



FLIGHT CONTROL SYSTEM DESIGN FOR AN OVER ACTUATED UAV AGAINST  
ACTUATOR FAILURES

A THESIS SUBMITTED TO  
THE GRADUATE SCHOOL OF NATURAL AND APPLIED SCIENCES  
OF  
MIDDLE EAST TECHNICAL UNIVERSITY

BY

SİNEM IŞIK

IN PARTIAL FULFILLMENT OF THE REQUIREMENTS  
FOR  
THE DEGREE OF MASTER OF SCIENCE  
IN  
AEROSPACE ENGINEERING

FEBRUARY 2010

Approval of the thesis:

**FLIGHT CONTROL SYSTEM DESIGN FOR AN OVER ACTUATED UAV AGAINST  
ACTUATOR FAILURES**

submitted by **SİNEM İŞİK** in partial fulfillment of the requirements for the degree of  
**Master of Science in Aerospace Engineering Department, Middle East Technical Uni-  
versity** by,

Prof. Dr. Canan Özgen  
Dean, Graduate School of **Natural and Applied Sciences**

\_\_\_\_\_

Prof. Dr. Ozan Tekinalp  
Head of Department, **Aerospace Engineering**

\_\_\_\_\_

Prof. Dr. Ozan Tekinalp  
Supervisor, **Aerospace Engineering Dept., METU**

\_\_\_\_\_

**Examining Committee Members:**

Assoc. Prof. Dr. Demirkan Çöker  
Aerospace Engineering Dept., METU

\_\_\_\_\_

Prof. Dr. Ozan Tekinalp  
Aerospace Engineering Dept., METU

\_\_\_\_\_

Assoc. Prof. Dr. Ali Türker Kutay  
Aerospace Engineering Dept., METU

\_\_\_\_\_

Dr. Volkan Nalbantoğlu  
MGEO, ASELSAN

\_\_\_\_\_

Dr. Tayfun Çimen  
Sr. Systems & Control Engineer, ROKETSAN

\_\_\_\_\_

**Date:**

\_\_\_\_\_

**I hereby declare that all information in this document has been obtained and presented in accordance with academic rules and ethical conduct. I also declare that, as required by these rules and conduct, I have fully cited and referenced all material and results that are not original to this work.**

Name, Last Name: SİNEM IŞIK

Signature :

# ABSTRACT

## FLIGHT CONTROL SYSTEM DESIGN FOR AN OVER ACTUATED UAV AGAINST ACTUATOR FAILURES

Işık, Sinem

M.S, Department of Aerospace Engineering

Supervisor : Prof. Dr. Ozan Tekinalp

February 2010, 124 pages

This thesis describes the automatic flight control systems designed for a conventional and an over actuated unmanned air vehicle (UAV). A nonlinear simulation model including the flight mechanics equations together with the interpolated nonlinear aerodynamics, environmental effects, mass-inertia properties, thrust calculations and actuator dynamics is created; trim and linearization codes are developed. Automatic flight control system of the conventional UAV is designed by using both classical and robust control methods. Performances of the designs for full autonomous flight are tested through nonlinear simulations for different maneuvers in the presence of uncertainties and disturbances in the aircraft model. The fault tolerant control of an over actuated UAV is the main concern of the thesis. The flight control system is designed using classical control techniques. Two static control allocation methods are examined: Moore-Penrose pseudo inverse and blended inverse. For this purpose, an aircraft with three sets of ailerons is employed. It is shown that with redundant control surfaces, fault tolerant control is possible. Although both of the static control allocation methods are found to be quite successful to realize the maneuvers, the new blended inverse algorithm is shown to be more effective in controlling the aircraft when some of the control surfaces are lost. It is also demonstrated that, with redundant control surfaces it is possible to recover the aircraft

during a maneuver even some of the control surfaces are damaged or got stuck at a particular deflection.

Keywords: UAV, Flight Mechanics, Automatic Flight Control System, Robust Controller, Control Allocation

# ÖZ

## ARTIK EYLEYİCİLİ BİR İHA İÇİN EYLEYİCİ ARIZALARINA KARŞI UÇUŞ KONTROL SİSTEMİ TASARIMI

Işık, Sinem

Yüksek Lisans, Havacılık ve Uzay Mühendisliği Bölümü

Tez Yöneticisi : Prof. Dr. Ozan Tekinalp

Şubat 2010, 124 sayfa

Bu tez konvensiyonel ve artık eyleyicili bir İnsansız Hava Aracı (İHA) için tasarlanan otomatik uçuş kontrol sistemlerini anlatmaktadır. Uçuş mekaniği denklemleriyle beraber aerodinamik etkiler, çevresel etkiler, kütle-eylemsizlik özellikleri, itki hesaplamaları ve eyleyici dinamiklerini içeren doğrusal olmayan benzetim modeli yaratılmış; trim ve doğrusallaştırma kodları geliştirilmiştir. Konvensiyonel İHA'nın otomatik uçuş kontrol sistemi, klasik ve gürbüz kontrol methodlarının her ikisi birden kullanılarak tasarlanmıştır. Tasarımların tam otonom uçuşdaki performansları, hem belirsizlik hem de bozucu etkilerin bulunduğu doğrusal olmayan benzetimler aracılığıyla farklı manevralar için test edilmiştir. Artık eyleyicili bir İHA'nın hata toleranslı kontrolü tezin temel çalışma konusudur. Uçuş kontrol sistemi, klasik kontrol yöntemleri kullanılarak tasarlanmıştır. İki statik kontrol dağıtım methodu incelenmiştir: Moore-Penrose pseudo inverse ve blended inverse. Bu amaçla, üç kanatçık seti bulunan bir uçak kullanılmıştır. Artık kontrol yüzeleriyle hata toleranslı kontrolün mümkün olduğu gösterilmiştir. Her iki statik kontrol dağıtım methodu da manevranın gerçekleştirilmesinde oldukça başarılı olsa da, yeni blended inverse algoritmasının kontrol yüzelerinden bazıları kaybedildiği zaman uçağın kontrolünde daha etkili olduğu gösterilmiştir. Ayrıca, manevra esnasında kontrol yüzelerinden bazıları hasar görse veya belirli bir açıda takılı kalsalar dahi

artık kontrol yüzeyleriyle uçağın kurtarılmasının mümkün olduğu gösterilmiştir.

Anahtar Kelimeler: IHA, Uçuş Mekaniği, Otomatik Uçuş Kontrol Sistemi, Gürbüz Kontrolcü,  
Kontrol Dağıtımı

*to my mother*

## ACKNOWLEDGMENTS

I would like to express my sincere gratitude to my supervisor Prof. Dr. Ozan Tekinalp for his guidance, aid and support. He provided the necessary resources during the research and shared his invaluable knowledge and experience with me through the thesis.

I would like to thank Dr. İlkey Yavrucuk for his assistance. His energy, enthusiasm and advises helped me to complete this thesis. Special thanks to Dr. Volkan Nalbantoğlu and Dr. Ali Turker Kutay for their suggestions. They shared their time, energy and knowledge whenever I needed.

I wish to state my special thanks to Onur Tarımcı. He always supported me and never turned me down when I requested help. I appreciate his patience and very precious aid during the last two years. I would also like to thank my dear friend Zeynep Çakır for her useful discussions with me during the thesis. Also thanks to my other friends in the Simulation, Control and Avionics Laboratory, Batu Demir, Tuba Elmas, Yunus Emre Arslantaş, Mehmet Katırcıoğlu and Eser Kubalı for their precious moral aid. I should not forget my dear friends Tuğba Ünlü, Hilal Erçin, Arzu Kayır and Miray Demir, who have always supported me. Special thanks to Tuğba Ünlü for helping me about Latex. Also, thanks to Gökhan Ahmet, Sinan Körpe and Mehmet Can Kılıç for their positive energy.

Finally, I would like to express my deepest thanks to my family for their endless trust, patience and encouragements, especially to my mother for always believing in and supporting me. It would not be possible for me to finish this thesis if it weren't for her.

This study is supported by the Scientific and Technological Research Council of Turkey (TUBITAK), Project No: 107M346.

# TABLE OF CONTENTS

ABSTRACT . . . . .	iv
ÖZ . . . . .	vi
ACKNOWLEDGMENTS . . . . .	ix
TABLE OF CONTENTS . . . . .	x
LIST OF TABLES . . . . .	xv
LIST OF FIGURES . . . . .	xvii
LIST OF ABBREVIATIONS . . . . .	xxi
CHAPTERS	
1 INTRODUCTION . . . . .	1
1.1 Overview . . . . .	1
1.2 Aim of the Thesis . . . . .	1
1.3 Literature Survey . . . . .	2
1.3.1 Recent Work on UAV Modeling . . . . .	2
1.3.2 Recent Work on Robust Control . . . . .	3
1.3.3 Recent Work on Control Allocation . . . . .	5
1.4 Contents of the Thesis . . . . .	6
1.5 Original Contributions of the Thesis . . . . .	7
2 NONLINEAR 6-DOF MATHEMATICAL MODEL . . . . .	8
2.1 Platform . . . . .	8
2.2 Reference Frames and Sign Conventions . . . . .	10
2.3 Simulation Structure . . . . .	12
2.4 Aerodynamic Model . . . . .	14
2.5 Propulsion Model . . . . .	15

2.6	Mass - Inertia Model . . . . .	15
2.7	Atmosphere Model . . . . .	16
2.8	Wind Gust Model . . . . .	17
2.9	Equations of Motion Model . . . . .	17
2.9.1	Forces and Moments . . . . .	17
2.9.2	6-DOF Equations of Motion . . . . .	18
2.10	Actuator Models . . . . .	20
3	TRIM AND LINEARIZATION ANALYSES . . . . .	21
3.1	Trim Analyses . . . . .	21
3.1.1	Steady State Flight Conditions . . . . .	22
3.1.2	Trim Method . . . . .	23
3.2	Linearization . . . . .	24
3.2.1	Linearization Method . . . . .	24
3.2.2	Uncoupled Dynamics . . . . .	26
3.3	Validation of Simulation, Trim and Linearization Tools . . . . .	26
3.3.1	Trim Results . . . . .	26
3.3.2	Linearization Results . . . . .	28
3.4	Trim and Linearization Results of the UAV . . . . .	28
3.4.1	Trim Results . . . . .	28
3.4.2	Linearization Results . . . . .	31
3.5	Validation of the Linear Model . . . . .	32
4	CONTROLLER DESIGNS FOR THE CONVENTIONAL UAV . . . . .	36
4.1	PID Classical Controller Design . . . . .	36
4.1.1	PID Classical Control Method . . . . .	36
4.1.2	Controller Gains and Tuning . . . . .	37
4.1.3	Command Filters . . . . .	39
4.1.4	Longitudinal Autopilot . . . . .	39
4.1.5	Lateral Autopilot . . . . .	41
4.1.6	Robustness Analysis of the Classical Controllers . . . . .	42
4.2	Robust Controller Design . . . . .	44

4.2.1	Problem Statement . . . . .	44
4.2.2	Norms of Systems . . . . .	45
4.2.3	Linear Fractional Transformations (LFTs) . . . . .	47
4.2.4	Closed Loop Transfer Functions . . . . .	48
4.2.5	Model Uncertainty . . . . .	49
	4.2.5.1 Parametric Uncertainty . . . . .	50
	4.2.5.2 Unmodeled Dynamics Uncertainty . . . . .	50
4.2.6	Stability and Performance Requirements for SISO Systems	52
	4.2.6.1 Nominal Stability (NS) . . . . .	53
	4.2.6.2 Nominal Performance (NP) . . . . .	53
	4.2.6.3 Robust Stability (RS) . . . . .	53
	4.2.6.4 Robust Performance (RP) . . . . .	54
4.2.7	Stability and Performance Requirements for MIMO Systems	55
	4.2.7.1 Nominal Stability (NS) . . . . .	55
	4.2.7.2 Nominal Performance (NP) . . . . .	55
	4.2.7.3 Robust Stability (RS) . . . . .	56
	4.2.7.4 Robust Performance (RP) . . . . .	56
4.2.8	Solution of the $H_\infty$ Problem . . . . .	56
4.2.9	$\mu$ Analysis . . . . .	58
	4.2.9.1 Structured Singular Value ( $\mu$ ) . . . . .	58
	4.2.9.2 Robust Stability (RS) . . . . .	61
	4.2.9.3 Robust Performance (RP) . . . . .	61
4.2.10	Implementation on MATLAB . . . . .	62
	4.2.10.1 Controller Configuration . . . . .	62
	4.2.10.2 Obtaining Controllers . . . . .	63
	4.2.10.3 $\mu$ Analysis . . . . .	64
4.2.11	Longitudinal Autopilot . . . . .	65
	4.2.11.1 Controller Configuration . . . . .	65
	4.2.11.2 Choice of Weighting Functions . . . . .	67
	4.2.11.3 Robust Performance Analysis . . . . .	71

4.2.12	Lateral Autopilot . . . . .	71
4.2.12.1	Controller Configuration . . . . .	71
4.2.12.2	Choice of Weighting Functions . . . . .	72
4.2.12.3	Robust Performance Analysis . . . . .	76
5	COMPARISON OF CLASSICAL AND ROBUST CONTROLLERS . . . . .	77
5.1	Performance Comparison of Controllers for Unit Step Inputs . . . . .	77
5.1.1	Pitch Attitude Response . . . . .	78
5.1.2	Longitudinal Velocity Response . . . . .	80
5.1.3	Roll Attitude Response . . . . .	82
5.1.4	Yaw Rate Response . . . . .	84
5.2	Performance Comparison of Controllers for Full Autonomous Flight . . . . .	86
5.2.1	Longitudinal Maneuvers . . . . .	87
5.2.2	Lateral Maneuvers . . . . .	90
6	FAULT TOLERANT CONTROLLER DESIGN FOR AN OVER ACTUATED UAV . . . . .	93
6.1	Allocation Methodology . . . . .	93
6.1.1	Moore-Penrose Pseudo (MP) Inverse . . . . .	95
6.1.2	Blended Inverse (BI) . . . . .	95
6.2	Control Allocation for the UAV . . . . .	96
6.2.1	Over Actuated Mechanism of Controls . . . . .	96
6.2.2	Controller Configuration . . . . .	97
6.2.3	Determination of the Controller Gains . . . . .	98
6.2.4	Determination of the Weightings in Allocation . . . . .	99
6.3	Results and Discussion . . . . .	100
6.3.1	Scenario-1 . . . . .	100
6.3.2	Scenario-2 . . . . .	103
6.3.3	Scenario-3 . . . . .	107
6.3.4	Scenario-4 . . . . .	110
7	CONCLUSION . . . . .	113
	REFERENCES . . . . .	115

## APPENDICES

A	UAV GEOMETRY . . . . .	119
A.1	Aircraft Geometric Parameters . . . . .	119
A.1.1	Wing Geometry . . . . .	119
A.1.2	Horizontal Tail Geometry . . . . .	120
A.1.3	Vertical Tail Geometry . . . . .	120
B	SIMULATION SUBSYSTEMS . . . . .	121
C	LINEARIZED SYSTEM MATRICES . . . . .	123
C.1	Conventional UAV . . . . .	123
C.2	Over Actuated UAV . . . . .	124

## LIST OF TABLES

### TABLES

Table 2.1	Specifications of SIG Rascal 110 . . . . .	9
Table 2.2	Component Weights . . . . .	10
Table 2.3	Average Thrust, Current and RPM Values for Different Throttle Settings . . . . .	15
Table 2.4	Mass and Inertias of the UAV . . . . .	15
Table 2.5	Actuator Limits . . . . .	20
Table 3.1	Comparison of Eigenvalues for Cessna 172 Airplane Flying at 1524 m with 66 m/s . . . . .	28
Table 3.2	Eigenvalues of Rascal for 20 m/s Wings-level Flight at 1000m . . . . .	31
Table 3.3	Longitudinal Mode Characteristics of Rascal . . . . .	31
Table 3.4	Dutch Roll Mode Characteristics of Rascal . . . . .	31
Table 3.5	Roll and Spiral Mode Characteristics of Rascal . . . . .	32
Table 4.1	Longitudinal Controller Gains . . . . .	40
Table 4.2	Lateral Controller Gains . . . . .	41
Table 4.3	PID Controller Gains for the Longitudinal Autopilot . . . . .	66
Table 5.1	Performance Comparison of Controllers for Pitch Attitude . . . . .	78
Table 5.2	Performance Comparison of Controllers for Longitudinal Velocity . . . . .	80
Table 5.3	Performance Comparison of Controllers for Roll Attitude . . . . .	82
Table 5.4	Performance Comparison of Controllers for Yaw Rate . . . . .	84
Table 5.5	Gaussian Noise Characteristics . . . . .	86
Table 6.1	Controller Gains . . . . .	99

Table A.1 Geometric Parameters of Wing . . . . .	119
Table A.2 Geometric Parameters of Horizontal Tail . . . . .	120
Table A.3 Geometric Parameters of Vertical Tail . . . . .	120

## LIST OF FIGURES

### FIGURES

Figure 2.1 SIG Rascal 110 General View . . . . .	9
Figure 2.2 Relation between Body-fixed and Earth-fixed Frames . . . . .	11
Figure 2.3 Relation between Stability - Wind - Body-fixed Frames . . . . .	11
Figure 2.4 Positive Deflections of the Control Surfaces . . . . .	12
Figure 2.5 Simulink <sup>®</sup> Nonlinear Simulation Diagram of the Air Vehicle . . . . .	13
Figure 2.6 Subsystems of the Nonlinear Simulation Model . . . . .	13
Figure 3.1 Simulation Results of Cessna 172 for Steady Wings-level Flight . . . . .	27
Figure 3.2 Nonlinear Simulation Results for Coordinated Turn Flight of Rascal at Trimmed Flight . . . . .	29
Figure 3.3 Simulation Results of Rascal after 5 degrees of Elevator Doublet . . . . .	30
Figure 3.4 Variation of Elevator Deflection with Time . . . . .	33
Figure 3.5 Linear and Nonlinear Simulation Results for 5 degrees of Elevator Doublet Input . . . . .	33
Figure 3.6 Variation of Percent Throttle with Time . . . . .	34
Figure 3.7 Linear and Nonlinear Simulation Results for 10 % of Throttle Step Input . . . . .	34
Figure 3.8 Variation of Aileron Deflection with Time . . . . .	35
Figure 3.9 Linear and Nonlinear Simulation Results for 5 degrees of Aileron Doublet Input . . . . .	35
Figure 4.1 Block Diagram of the Longitudinal Controller . . . . .	40
Figure 4.2 Block Diagram of the Lateral Controller . . . . .	41
Figure 4.3 Bode Diagram of Altitude Channel . . . . .	42

Figure 4.4	Bode Diagram of Roll Attitude Channel . . . . .	43
Figure 4.5	Bode Diagram of Yaw Rate Channel . . . . .	43
Figure 4.6	General Design Framework . . . . .	45
Figure 4.7	Block Diagram of an LTI System . . . . .	45
Figure 4.8	Lower Linear Fractional Transformation . . . . .	47
Figure 4.9	Upper Linear Fractional Transformation . . . . .	48
Figure 4.10	Feedback Configuration . . . . .	48
Figure 4.11	Multiplicative Uncertainty . . . . .	51
Figure 4.12	Additive Uncertainty . . . . .	52
Figure 4.13	System Structure for Stability and Performance Criteria . . . . .	52
Figure 4.14	$M\Delta$ Structure for Small Gain Theorem . . . . .	54
Figure 4.15	General Control Configuration using LFTs . . . . .	55
Figure 4.16	$M\Delta$ Structure . . . . .	58
Figure 4.17	Modified $M\Delta$ Structure . . . . .	59
Figure 4.18	Set of Perturbed Plants . . . . .	61
Figure 4.19	Block Diagram of the Closed-loop System . . . . .	62
Figure 4.20	Block Diagram of the $M\Delta$ Structure . . . . .	64
Figure 4.21	Block Diagram of the Longitudinal Autopilot . . . . .	65
Figure 4.22	Bode Plots of $W_{p1}$ and $W_{p2}$ . . . . .	68
Figure 4.23	Relative Errors for Elevator Inputs . . . . .	69
Figure 4.24	Relative Errors for Throttle Inputs . . . . .	70
Figure 4.25	$\mu$ Curve for Robust Performance of the Longitudinal Controller . . . . .	71
Figure 4.26	Block Diagram of the Lateral Autopilot . . . . .	72
Figure 4.27	Bode Plots of $W_{p1}$ and $W_{p2}$ . . . . .	73
Figure 4.28	Relative Errors for Aileron Inputs . . . . .	74
Figure 4.29	Relative Errors for Rudder Inputs . . . . .	75
Figure 4.30	$\mu$ Curve for Robust Performance of the Lateral Controller . . . . .	76
Figure 5.1	Variation of Pitch Attitude with Time . . . . .	78

Figure 5.2	Variation of Elevator Deflection with Time . . . . .	79
Figure 5.3	Variation of Elevator Deflection Rate with Time . . . . .	79
Figure 5.4	Variation of Longitudinal Velocity with Time . . . . .	80
Figure 5.5	Variation of Percent Throttle with Time . . . . .	81
Figure 5.6	Variation of Percent Throttle Rate with Time . . . . .	81
Figure 5.7	Variation of Roll Attitude with Time . . . . .	82
Figure 5.8	Variation of Aileron Deflection with Time . . . . .	83
Figure 5.9	Variation of Aileron Deflection Rate with Time . . . . .	83
Figure 5.10	Variation of Yaw Rate with Time . . . . .	84
Figure 5.11	Variation of Rudder Deflection with Time . . . . .	85
Figure 5.12	Variation of Rudder Deflection Rate with Time . . . . .	85
Figure 5.13	Simulation Results for Decreasing Velocity by 5 m/s at Constant Altitude .	88
Figure 5.14	Simulation Results for Increasing Altitude by 50 m while Increasing Ve- locity by 5 m/s . . . . .	89
Figure 5.15	Simulation Results for a Coordinated Turn with 3 deg/s Turn Rate . . . . .	91
Figure 5.16	Simulation Results for a Fixed Roll Maneuver . . . . .	92
Figure 6.1	Block Diagram of the Control System . . . . .	98
Figure 6.2	Block Diagram of the Combined System . . . . .	98
Figure 6.3	Simulation Results for Comparison of MP-Inverse and Blended Inverse Methods . . . . .	101
Figure 6.4	Variations of the Controls for Comparison of MP-Inverse and Blended In- verse Methods . . . . .	102
Figure 6.5	Variations of the Controls for a Roll Maneuver with Conventional UAV . . .	103
Figure 6.6	Simulation Results for a Roll Maneuver with Conventional UAV . . . . .	104
Figure 6.7	Variations of the Controls for a Roll Maneuver with Redundant Ailerons .	105
Figure 6.8	Simulation Results for a Roll Maneuver with Redundant Ailerons . . . . .	106
Figure 6.9	Variations of the Controls for a Coordinated Turn Maneuver with Redun- dant Ailerons . . . . .	108
Figure 6.10	Simulation Results for a Coordinated Turn Maneuver with Redundant Ailerons	109

Figure 6.11 Simulation Results for Comparison of System Responses with and without Blended Inverse Method . . . . .	111
Figure 6.12 Variations of the Controls for Comparison of System Responses with and without Blended Inverse Method . . . . .	112
Figure B.1 Atmosphere Subsystem Model . . . . .	121
Figure B.2 Aerodynamics Subsystem Model . . . . .	122
Figure B.3 Equations of Motion Subsystem Model . . . . .	122

## LIST OF ABBREVIATIONS

<p>A, B, C, D Linearized system matrices</p> <p>b Wing reference span</p> <p>c Wing reference chord</p> <p>d Disturbance</p> <p>e Error signal</p> <p>F, M Forces, Moments</p> <p>G Nominal Plant</p> <p>g Gravity</p> <p>h Altitude</p> <p><math>I_{xx}</math> Inertia in body x-axis</p> <p><math>I_{yy}</math> Inertia in body y-axis</p> <p><math>I_{zz}</math> Inertia in body z-axis</p> <p><math>I_{xz}</math> Inertia in body x-z plane</p> <p><math>I_{xy}</math> Inertia in body x-y plane</p> <p><math>I_{yz}</math> Inertia in body y-z plane</p> <p><math>I_n</math> n-dimensional unit matrix</p> <p>K Controller</p> <p><math>K_p</math> Proportional gain</p> <p><math>K_i</math> Integral gain</p> <p><math>K_d</math> Derivative gain</p> <p>m mass</p> <p><math>N_x, N_y, N_z</math> Normal accelerations in 3 axes</p> <p>n Noise</p> <p>P Generalized Plant</p> <p>p, q, r Body angular velocities</p> <p>q Dynamic pressure, blending coefficient</p> <p>Q, R Weighting matrices for state-errors and controls</p> <p>R, M, N Body-fixed roll, pitch, yaw moments</p> <p>r Reference signal</p> <p>S Sensitivity function</p>	<p>T Complementary sensitivity function</p> <p>u, v, w Body translational velocities</p> <p>u, x, <math>\dot{x}</math> System inputs, states, state derivatives</p> <p>u Control signal</p> <p>V Total velocity</p> <p>w External input</p> <p>X, Y, Z Body-fixed drag, sideforce, lift force</p> <p><math>X_E</math> East position</p> <p><math>X_N</math> North position</p> <p>z Error signal related to uncertainties</p> <p style="text-align: center;"><b>Greek Symbols</b></p> <p><math>\alpha</math> Angle of attack</p> <p><math>\dot{\alpha}</math> Rate of angle of attack</p> <p><math>\beta</math> Sideslip angle</p> <p><math>\gamma</math> Flight path angle</p> <p><math>\delta_{ail}</math> Aileron input</p> <p><math>\delta_{elev}</math> Elevator input</p> <p><math>\delta_{rud}</math> Rudder input</p> <p><math>\delta_{th}</math> Throttle input</p> <p><math>\Delta</math> Variation, perturbation</p> <p><math>\zeta</math> Damping ratio</p> <p><math>\mu</math> Structured singular value</p> <p><math>\rho</math> Air density</p> <p><math>\omega_n</math> Natural frequency</p> <p><math>\phi, \theta, \psi</math> Roll, pitch, yaw attitudes</p> <p style="text-align: center;"><b>Subscripts</b></p> <p>A Aerodynamics</p> <p>ac Aerodynamic center</p>
---	---

<i>act</i>	Actuator	<i>NED</i>	North-East-Down
<i>aero</i>	Aerodynamic coefficients	<i>NP</i>	Nominal Performance
<i>body</i>	in body-fixed frame	<i>NS</i>	Nominal Stability
<i>cg</i>	Due to center of gravity	<i>PIC</i>	Peripheral Interface Controller
<i>des</i>	Desired	<i>PID</i>	Proportional-Integral-Derivative
<i>dyn</i>	Dynamic coefficients	<i>RC</i>	Robust Controller
<i>e</i>	Error	<i>RHP</i>	Right Hand Plane
<i>eq</i>	Equilibrium	<i>RMS</i>	Root Mean Square
<i>G</i>	Gravity	<i>RP</i>	Robust Performance
<i>late</i>	Lateral-directional	<i>RPM</i>	Revolution Per Minute
<i>long</i>	Longitudinal	<i>RS</i>	Robust Stability
<i>p</i>	Perturbed	<i>SAS</i>	Stability Augmentation System
<i>ref</i>	Reference input	<i>SISO</i>	Single Input single Output
<i>SL</i>	Sea level	<i>SSV</i>	Structured Singular Value
<i>T</i>	Thrust	<i>UAV</i>	Unmanned Aerial Vehicle
<i>WBHV</i>	Wing-body-horizontal-vertical tail configuration	<i>USAF</i>	United States Air Force
<i>wind</i>	in wind frame		

### Acronyms

6 – <i>DOF</i>	Six Degree Of Freedom
<i>BI</i>	Blended Inverse
<i>CC</i>	Classical Controller
<i>CG</i>	Center of Gravity
<i>DATCOM</i>	Data Compendium
<i>DC</i>	Direct Current
<i>DCM</i>	Direct Cosine Matrix
<i>ESC</i>	Electronic Speed Controller
<i>GPS</i>	Global Positioning System
<i>IMU</i>	Inertial Measurement Unit
<i>ISA</i>	International Standard Atmosphere
<i>LHP</i>	Left Hand Plane
<i>LTI</i>	Linear Time Invariant
<i>MIMO</i>	Multi Input Multi Output
<i>MP</i>	Moure-Penrose Pseudo
<i>NACA</i>	National Advisory Committee of Aeronautics

# CHAPTER 1

## INTRODUCTION

### 1.1 Overview

Unmanned air vehicles (UAVs) have been a growing research area in recent years. Being unmanned, UAVs are smaller and lighter than the piloted aircrafts, and provide the opportunity for autonomous flight applications with lower cost. In addition to their multi mission capability, UAVs also remove the danger to human life in dirty and dangerous missions that cannot be accomplished by manned aircraft [42]. As UAVs are capable of performing the missions that cannot be achieved by manned aircraft, they are preferred in both military and civilian applications for a wide range of missions [25]. Their possible uses in military operations include, surveillance, reconnaissance, maritime operations as well as autonomous combat operations, observation and convoy protection. UAVs of all size are also being used in civilian operations like search and rescue, disaster and emergency management, meteorological data acquisition, etc.

### 1.2 Aim of the Thesis

Although UAVs are expected to carry out complex missions, their reliability and fault tolerance is usually not addressed. There are basically two approaches to improve reliability. The first approach is to use reliable hardware and software. The second choice is to make the system redundant. The purpose of this thesis is to design an automatic flight control system for an over actuated UAV. A conventional UAV with three pairs of ailerons is considered and control allocation methods are addressed.

## 1.3 Literature Survey

### 1.3.1 Recent Work on UAV Modeling

UAVs are not only able to perform risky missions, but also they do this autonomously. A key requirement for autonomy is designing accurate flight control systems that stabilize the aircraft while also satisfying the performance requirements. For this purpose, first the vehicle dynamics should be modeled properly. Mathematical models, that describe the flight characteristics as well as the dynamic response of the vehicle to disturbances and control inputs, are used for aircraft design, trim and linearization analyses, development of flight control algorithms, testing/validating these algorithms, etc.

Development of accurate dynamic models requires detailed information about the system characteristics. Thus, components/subsystems of the aircraft such as aerodynamics, environmental effects, mass-inertia properties, propulsion system, equations of motion, actuator dynamics and various other features should be considered.

In the literature, many studies related to modeling of different types of UAVs are present. In Ref [47], a tilt-duct vertical takeoff and landing (VTOL) UAV is modeled in Matlab<sup>®</sup> - Simulink<sup>®</sup> environment. Aerodynamic database is generated by using USAF Digital Datcom software and all related work together with the geometry and design characteristics of the UAV are explained in detail. In Ref [25] on the other hand, a fixed-wing UAV, namely a SIG Rascal 110 aircraft, is modeled. Stability and dynamic derivatives are obtained from semi-empirical methods, namely USAF DATCOM, and the techniques presented in Ref [39] and [17]. Calculation of the inertia is performed through experiments. The aircraft is hanged from a single point in the ceiling and swung with constant oscillations. Then, counting and timing the prescribed oscillations, inertias are found and used in the 6-DOF simulation model constructed in Matlab<sup>®</sup> - Simulink<sup>®</sup>. The work presented in Ref [27] concerns the modeling of Middle East Technical University (METU) Tactical Unmanned Aerial Vehicle (TUAV). In this study, the dynamic model is generated by using FORTRAN programming language.

### 1.3.2 Recent Work on Robust Control

Automatic flight control systems are used to provide stability if the system is inherently unstable and change the system response to meet the performance specifications. Different techniques for linear and nonlinear methods are present in the literature and can be used for designing the controllers. Linear feedback control theory provides a basis for development of the flight control algorithms. Linearizing the system dynamics around an equilibrium point, the linear time invariant (LTI) system can be obtained and then used for designing the autopilots.

Linear methods based on classical PID techniques are widely used for flight control system designs. Classical sequential loop closing methods provide a powerful design tool especially for single-input-single-output (SISO) systems. Closing the feedback loops on one another and adjusting the gains appropriately, the desired system response can be achieved and the performance requirements can be satisfied. More information about classical control methods can be found in Ref [17, 34, 37]. In addition, examples of different approaches related to classical controller designs are presented in Ref [26, 47].

Classical control methods based on PID techniques and gain scheduling are relatively simple when compared to robust and nonlinear control methods. Controllers designed with classical techniques are capable of satisfying the nominal stability and nominal performance specifications. However, when the mathematical model contains some uncertainty resulting from variations in the plant parameters and unmodeled/neglected dynamics, classical controllers may not be fully successful. Since they are rather sensitive to disturbances as well as uncertainties, the desired system response might not be obtained, actuator limits might not be satisfied, etc. Therefore, a need for robust controllers that guarantee the stability of the aircraft and satisfy the performance requirements when the system deviates from its nominal design condition and/or subjected to significant disturbances has risen.

The first important works related to  $H_\infty$  optimization of control systems were made by Zames and Doyle. Zames [54] introduced the idea of a controller which makes the closed loop system stable and minimizes the peak value ( $H_\infty$  norm) of the sensitivity function of a SISO linear feedback system in 1979 and formulated the  $H_\infty$  optimal control theory in 1981 [55] for the first time. Doyle [15] proposed the stability robustness criterion that demonstrates the impor-

tance of  $H_\infty$  norm for robustness in 1979 and gave the first state-space solution to the  $H_\infty$  problem in 1984 [12]. In 1987, Francis and Doyle [18] introduced a solution to the MIMO optimal problem. However, computational difficulties resulting from the Algebraic Riccati Equations (AREs) caused some problems. Then, the solution was found by Doyle, Glover, Khargonekar and Francis [14] in 1989 by proposing the state-space methods for MIMO systems.

Robust control techniques such as  $H_\infty$  control and  $\mu$ -synthesis are used to develop control laws that are efficient in satisfying the stability and performance specifications while also handling uncertainties and attenuating disturbances. Detailed information about the theory and its applications to SISO and MIMO systems can be found in Ref [32, 43, 57]. In addition, there are various studies in the literature regarding robust controller designs with different approaches. Ref [28] concerns design of MIMO robust controllers for different types of aircrafts. The design process is discussed for each aircraft and performances of the controllers designed by using  $H_\infty$  transformation methods are also analyzed. In Ref [41], a robust nonlinear controller design is performed by combining  $H_\infty$  control and dynamic inversion methods. The controller is designed for a complete UAV mission in the Matlab<sup>®</sup> - Simulink<sup>®</sup> environment. In addition to uncertainties in weight, center of gravity location and stability derivatives; atmospheric disturbances and measurement noises are also taken into account. Ref [44] and [51] discuss robust controller design for F-16 longitudinal and lateral dynamics, respectively. In these studies, linear parameter varying feedback control and sliding mode control methods are applied to MIMO systems. Lastly, in Ref [30], a robust controller is designed for a turn coordination system by using the  $H_\infty$  optimal control method. Variations in the stability and control derivatives are considered as the source of uncertainties in the model parameters and a parameter identification study is performed in order to find the difference between the aerodynamic coefficients.

### 1.3.3 Recent Work on Control Allocation

Conventional aircrafts use three main control surfaces in order to generate the required moments for controlling of the aircraft. An elevator is used for pitch control, whereas ailerons and rudder are necessary for roll and yaw controls. However, with this configuration, if one or more of the control surfaces are not operating, airplane loss may be unavoidable. With introducing redundancy to the system, performance and maneuverability of the aircraft can be improved and control loss can be minimized. In addition, a more reliable system can be obtained which works under a wide range of failure conditions.

System reliability may be realized by using reliable components introducing redundancy to the systems. This can be achieved by using unconventional controls such as flaps, canards, ruddervators, elevons etc. Unmanned air vehicles using commercial off the shelf elements may also be made more reliable and fault tolerant by introducing redundancy in subsystems. Redundancies in flight control systems among other things may be realized using redundant set of aerodynamic control surfaces that may counteract possible failures in any of those control surfaces, thus improving the survivability. In addition, these control surfaces may be used to improve the flight quality of the air vehicle. One such study [1] uses multiple ailerons and reports on the improvement in flight performance.

The main issue in flying with an over actuated system is the method used in allocating controls. The static control allocation methods are extensively used in steering redundant robot manipulators [3, 36] as well as spacecraft actuators mainly the control moment gyroscopes [52, 53]. In these systems, static allocation techniques are used to prevent possible singularities at certain gimbal angles ( $-90^\circ$   $180^\circ$   $90^\circ$   $0^\circ$ ) and to increase the motion capability by performance optimization.

Moore-Penrose pseudo (MP) inverse, weighted MP inverse, singularity robust (SR) inverse and blended inverse (BI) are some methods used for static control allocation. Among these, BI developed by Tekinalp and Yavuzoğlu [49] is the most efficient method to allocate the controls for the over actuated mechanism. In their paper, BI algorithm is successfully applied to the steering of control moment gyroscopes. Additionally, in the work of Tekinalp, Ünlü and Yavrucuk [48], effectiveness of the BI method during transition phase flight control of a tilt-duct UAV is demonstrated.

Dynamic control allocation, which uses various forms of optimal control methods, is also proposed in the literature (see Ref [7, 23]). However, static control allocation has a significant advantage over dynamic control allocation. The advantage of static solutions in over actuated systems is that the controller may be designed separately without paying too much attention to how these controls are generated. Then using a static control allocation algorithm, the desired controls may be obtained from the solution of algebraic equations.

## **1.4 Contents of the Thesis**

In the thesis, geometric properties of the UAV and details of the 6-DOF nonlinear simulation model are described in Chapter 2. This simulation model is used in the calculations of the trim flight conditions, numerical linearization of flight mechanics equations and testing the flight control algorithms. In Chapter 3, trim and linearization methodologies are explained. Nonlinear simulation model, trim and linearization algorithms developed in Matlab<sup>®</sup> - Simulink<sup>®</sup> environment are validated by using Cessna 172 airplane's data for a certain flight condition. In addition, trim and linearization results as well as the stability analyses of the UAV are also presented in this chapter. Chapter 4 addresses the different controller design methods used in the thesis. Classical and robust control techniques are explained, longitudinal and lateral autopilots of the conventional UAV designed by classical and robust techniques are described, and results for  $\mu$  analyses are given. In Chapter 5, simulation results of the classical and robust controllers are presented. Autopilots of the conventional UAV designed by using the linear UAV model are compared through nonlinear simulations. First part of this chapter includes the performance comparison of the controllers for unit step input commands in presence of uncertainties. In the second part of this chapter, performances of the controllers are compared for different maneuvers in presence of disturbances as well as uncertainties. Chapter 6 addresses the fault tolerant control of an over actuated UAV. Allocation methods used in the thesis and the flight control system design are explained. Different control allocation techniques are compared and nonlinear simulation results for different scenarios are presented. Finally, in Chapter 7, conclusions are made and recommendations for the future work are summarized.

## 1.5 Original Contributions of the Thesis

The original contributions of the thesis may be summarized as follows:

- Development of the 6-DOF nonlinear simulation model, trim and linearization algorithms for an over actuated UAV
- Development of longitudinal and lateral MIMO robust controllers for a conventional UAV for full autonomous flight
- Application of inverse kinematic algorithms to the redundant control mechanism of the over actuated UAV
- Demonstration of the fault tolerance of the automatic flight control system designed for the over actuated UAV

## CHAPTER 2

### NONLINEAR 6-DOF MATHEMATICAL MODEL

The purpose of this chapter is to provide background information on the Rascal 110 UAV and to describe the 6-DOF nonlinear simulation model. First, specifications of the aircraft and its equipments are explained. Second, definitions of reference frames and sign conventions for control surface deflections are described. Next, the dynamic simulation model is presented in detail. This model is created in Matlab<sup>®</sup> - Simulink<sup>®</sup> environment and includes aerodynamic, propulsion, mass - inertia, atmosphere, wind gust and 6-DOF equations of motion models. Finally, the chapter ends with a discussion on the actuator models.

#### 2.1 Platform

Simulation, Control and Avionics Laboratory (SCALAB) of the Aerospace Engineering Department is involved in testing and development of flight control algorithms for conventional and over actuated aerospace vehicles, mainly airplanes and satellites under a research project supported by TUBITAK. As a part of this research project, a UAV test bed with associated flight control algorithms is being developed. The test bed is based on a model airplane (Figure 2.1). SIG Rascal 110 ARF is selected for its ease of use, large payload capacity and relatively stable performance characteristics.

It has a high wing configuration with 2.79 m wingspan and includes four primary controls, elevator, aileron, rudder and throttle. In Ref [25], performance data of the aircraft and airfoils can be found. Table 2.1 lists the primary specifications of the aircraft. Geometry and design characteristics are given in detail in Appendix A.



Figure 2.1: SIG Rascal 110 General View

Table 2.1: Specifications of SIG Rascal 110

Length (m)	1.66
Wing Span (m)	2.79
Wing Area (m <sup>2</sup> )	0.98
Cruise Velocity (m/s)	20
Operation Altitude (m)	1000

The airplane is to carry a PC/104 form factor single board computer, with an INS-magnetometer suite, a GPS sensor, as well as pressure sensors to measure static and dynamic pressures. The airplane is propelled by a brushless DC motor. It has been flown manually using a regular RC radio controller and will be flown autonomously through the onboard computer by using a switch. The data link communication between a portable computer and the airplane is realized using a pair of wireless modems. Components of the testbed together with their corresponding weights are shown in Table 2.2.

An important task in this study is the design and implementation of flight control algorithms on the PC/104 based flight control computer. The flight control computer uses the XPC-target real time operating system, and the algorithms developed in Matlab<sup>®</sup> - Simulink<sup>®</sup> environment will be downloaded from the host PC.

Table 2.2: Component Weights

Component	Weight (g)
PC/104	150
DC/DC converter	71
IMU	74
Modem	281
Switch, pressure sensors, RS PIC	200
GPS receiver	181
Power supply	400
UAV, engine, batteries, ESC, servos	6500
Total weight	~ 7900

## 2.2 Reference Frames and Sign Conventions

The inertial frame is a fixed (non-rotating and non-accelerating) frame. In the thesis, since earth is assumed to be flat and stationary in inertial space, the earth-fixed frame is considered as the inertial frame. It is attached to the center of the earth as shown in Figure 2.2.

The navigation (NED) frame is located on the surface of the earth such that x-axis points north, y-axis points east and z-axis points to the local gravity vector (down). Neglecting the curvature of the earth, NED frame coincides with the earth-fixed frame (Figure 2.2).

The body-fixed frame is an orthogonal axis system attached to the center of gravity (CG) of the aircraft and rotates with it. The x-axis points out of the nose, y-axis points to the right wing and z-axis points down.

The transformation from earth-fixed frame to body-fixed frame is defined by the Direction Cosine Matrix (DCM) obtained by three consecutive rotations. The angular rotations are called as the Euler angles. The first rotation is done around z-axis of the earth-fixed frame by  $\psi$ , the second rotation is done around the y-axis of the intermediate frame by  $\theta$  and the third rotation is done around the x-axis of the new intermediate frame by  $\phi$ . Then, taking transpose of the DCM, transformation from body-fixed frame to earth-fixed frame can be expressed as in equation 2.1.

$$L_{EB} = \begin{Bmatrix} \cos \theta \cos \psi & \sin \phi \sin \theta \cos \psi - \cos \phi \sin \psi & \cos \phi \sin \theta \cos \psi + \sin \phi \sin \psi \\ \cos \theta \sin \psi & \sin \phi \sin \theta \sin \psi + \cos \phi \cos \psi & \cos \phi \sin \theta \sin \psi - \sin \phi \cos \psi \\ -\sin \theta & \sin \phi \cos \theta & \cos \phi \cos \theta \end{Bmatrix} \quad (2.1)$$

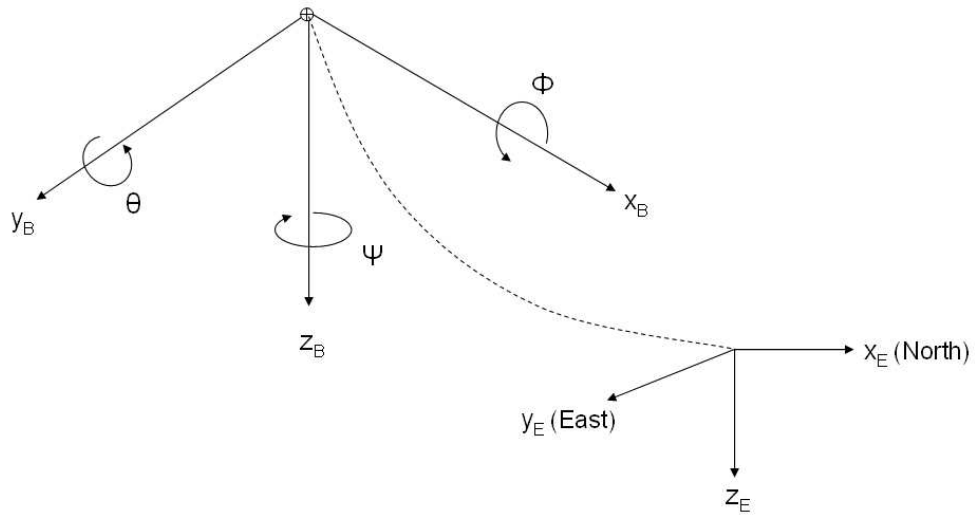


Figure 2.2: Relation between Body-fixed and Earth-fixed Frames

The stability frame is fixed to the aircraft. The x-axis is chosen parallel to the projection of  $V$  on the body-fixed frame. The difference between x-axes of the stability and body-fixed frames is equal to  $\alpha$ . The wind frame is oriented with respect to the flight path of the aircraft. Therefore, x-axis of the wind frame is parallel to the freestream velocity and the difference between x-axes of the wind and stability frames is equal to  $\beta$  (Figure 2.3).

The transformation from wind frame to body-fixed frame is defined as in equation 2.2.

$$L_{BW} = \begin{bmatrix} \cos\alpha\cos\beta & -\cos\alpha\sin\beta & -\sin\alpha \\ \sin\beta & \cos\beta & 0 \\ \sin\alpha\cos\beta & -\sin\alpha\sin\beta & \cos\alpha \end{bmatrix} \quad (2.2)$$

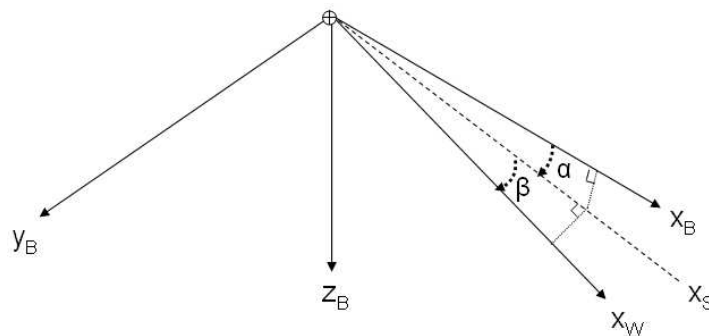


Figure 2.3: Relation between Stability - Wind - Body-fixed Frames

In the thesis, the positive elevator deflection is measured downwards (creating a pitch-down movement), the positive aileron deflection is measured downwards (creating a positive roll moment) and the positive rudder deflection is measured leftwards (creating a negative yaw moment). Figure 2.4 shows the positive deflections of the control surfaces.

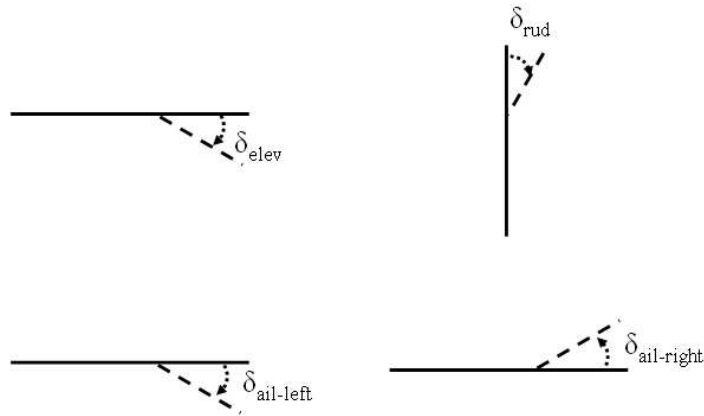


Figure 2.4: Positive Deflections of the Control Surfaces

### 2.3 Simulation Structure

The flight simulation code incorporates the flight mechanics equations together with an aerodynamic database. The aerodynamic database of the airplane is generated by using semi-empirical and empirical methods. The 6-DOF equations of motion, interpolated nonlinear aerodynamics, propulsion, mass-inertia and atmospheric models are formed in separate blocks and integrated in the Simulink<sup>®</sup> environment. This nonlinear simulation model is used in the calculations of the trim flight conditions, numerical linearization of flight mechanics equations, as well as testing the flight control algorithms. A window from the nonlinear simulation model is presented in Figure 2.5 and subsystems of this dynamic model are shown in Figure 2.6. In Appendix B, internal structures of subsystem models are given in detail.

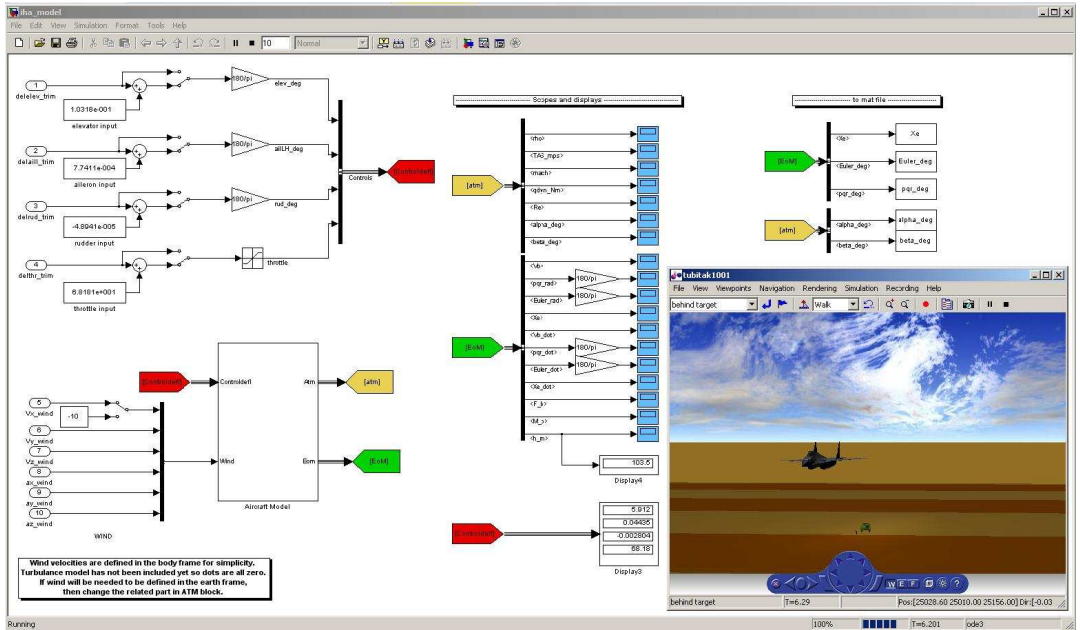


Figure 2.5: Simulink<sup>®</sup> Nonlinear Simulation Diagram of the Air Vehicle

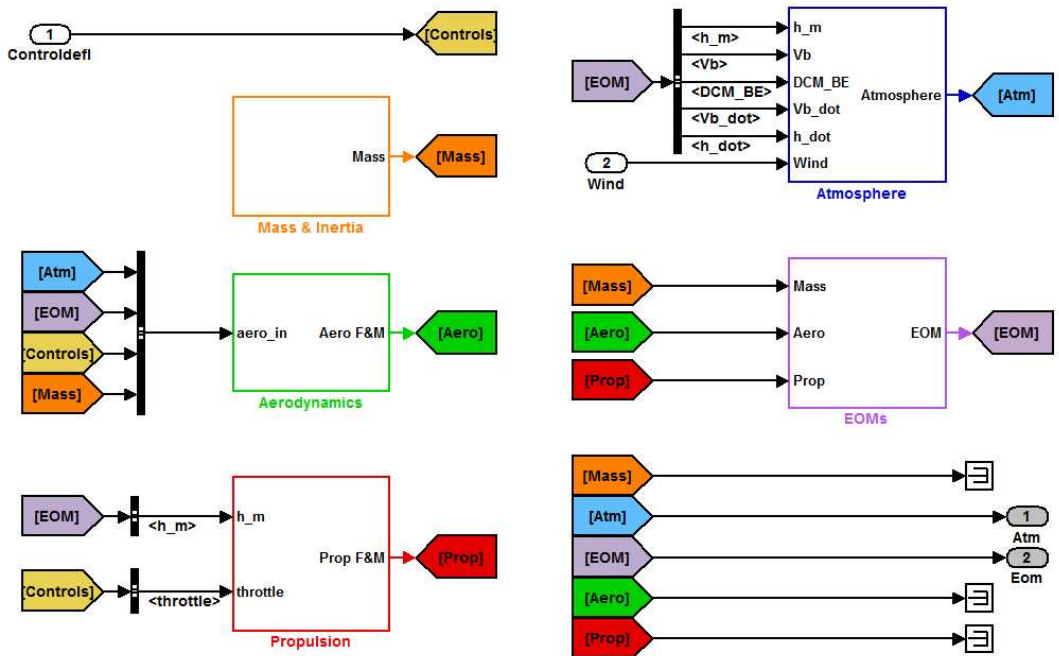


Figure 2.6: Subsystems of the Nonlinear Simulation Model

## 2.4 Aerodynamic Model

In this subsystem, the aerodynamic force and moment coefficients are calculated. The aerodynamic database of the airplane is generated mainly by using semi-empirical methods, USAF DATCOM [33]. Methods used in this software are shown to be also applicable to small UAVs [24]. Aerodynamic coefficients of each aircraft component are calculated individually. In addition, because DATCOM does not have a rudder model, empiric formulas in Ref [39] are used to compute rudder coefficients.

DATCOM outputs stability and dynamic derivatives separately. As a result, total coefficients are found by adding these derivatives together (Equation 2.3). For each longitudinal and lateral force and moment coefficient, this equation is given in details between equations 2.4 - 2.15. Since these coefficients are defined in stability axes, first a transformation to body axes is performed. Then, the aerodynamic forces and moments of each component are carried to the center of gravity (CG) as shown in equations 2.16 - 2.24.

$$C_{tot} = (C_{WBHV} + C_{\delta elev} + C_{\delta ail} + C_{\delta rud}) + C_{dyn} \quad (2.3)$$

$$C_L = C_{L_{WBHV}}(\alpha) + C_{L_{\delta elev}}(\delta_{elev}) + C_{L_{dyn}} \quad (2.4)$$

$$C_{L_{dyn}} = (C_{L_q}q + C_{L_{\dot{\alpha}}}\dot{\alpha})\frac{c}{V} \quad (2.5)$$

$$C_D = C_{D_{WBHV}}(\alpha) + C_{D_{\delta elev}}(\alpha, \delta_{elev}) + C_{D_{dyn}} \quad (2.6)$$

$$C_{D_{dyn}} = 0 \quad (2.7)$$

$$C_M = C_{M_{WBHV}}(\alpha) + C_{M_{\delta elev}}(\delta_{elev}) + C_{M_{dyn}} \quad (2.8)$$

$$C_{M_{dyn}} = (C_{M_q}q + C_{M_{\dot{\alpha}}}\dot{\alpha})\frac{c}{V} \quad (2.9)$$

$$C_Y = C_{Y_{WBHV,\beta}}\beta + C_{Y_{\delta rud}}(\delta_{rud}) + C_{Y_{dyn}} \quad (2.10)$$

$$C_{Y_{dyn}} = (C_{Y_p}(\alpha)p + C_{Y_r}r)\frac{b}{2V} \quad (2.11)$$

$$C_R = C_{R_{WBHV,\beta}}\beta + C_{R_{\delta ail}}(\delta_{ail}) + C_{R_{\delta rud}}(\alpha, \delta_{rud}) + C_{R_{dyn}} \quad (2.12)$$

$$C_{R_{dyn}} = (C_{R_p}(\alpha)p + C_{R_r}(\alpha)r)\frac{b}{2V} \quad (2.13)$$

$$C_N = C_{N_{WBHV,\beta}}\beta + C_{N_{\delta ail}}(\alpha, \delta_{ail}) + C_{N_{\delta rud}}(\alpha, \delta_{rud}) + C_{N_{dyn}} \quad (2.14)$$

$$C_{N_{dyn}} = (C_{N_p}(\alpha)p + C_{N_r}(\alpha)r)\frac{b}{2V} \quad (2.15)$$

$$C_{X_{cg}} = C_{X_{body}} \quad (2.16)$$

$$C_{Y_{cg}} = C_{Y_{body}} \quad (2.17)$$

$$C_{Z_{cg}} = C_{Z_{body}} \quad (2.18)$$

$$C_{R_{cg}} = C_{R_{body}} - (C_{Y_{body}} \Delta z_{cg} + C_{Z_{body}} \Delta y_{cg})/b \quad (2.19)$$

$$C_{M_{cg}} = C_{M_{body}} + (C_{X_{body}} \Delta z_{cg} - C_{Z_{body}} \Delta x_{cg})/c \quad (2.20)$$

$$C_{N_{cg}} = C_{N_{body}} + (C_{Y_{body}} \Delta x_{cg} + C_{X_{body}} \Delta y_{cg})/b \quad (2.21)$$

$$\Delta x_{cg} = x_{ac} - x_{cg} \quad (2.22)$$

$$\Delta y_{cg} = y_{ac} - y_{cg} \quad (2.23)$$

$$\Delta z_{cg} = z_{ac} - z_{cg} \quad (2.24)$$

## 2.5 Propulsion Model

Propulsion submodel is created by measuring thrust for different throttle stick positions. Average thrust values obtained from 4 different experiments are implemented into the simulation model as a function of throttle stick deflection by using a look up table (Table 2.3). Motor torque resulting from the propeller motion is neglected.

Table 2.3: Average Thrust, Current and RPM Values for Different Throttle Settings

Throttle Stick (%)	Average Thrust (N)	Average Current (A)	Average RPM
25	22.4	10.1	2925
50	61.3	39.4	4800
75	63.6	41.9	4850
100	63.1	41.3	4825

## 2.6 Mass - Inertia Model

As mentioned previously in Section 2.1, the aircraft uses a brushless DC motor. Since there is no fuel consumption, CG position does not change during the flight. Therefore, inertias are taken constant throughout the simulations. Weight and corresponding inertia values [25] are shown in Table 2.4.

Table 2.4: Mass and Inertias of the UAV

Weight (kg)	Ixx (kgm <sup>3</sup> )	Iyy (kgm <sup>3</sup> )	Izz (kgm <sup>3</sup> )	Ixz (kgm <sup>3</sup> )
7.9	2.64	2.10	2.60	0

## 2.7 Atmosphere Model

Air density is a key factor that affects aircraft performance. It is needed for the solution of equations of motion; hence, necessary for force and moment calculations. At low speeds, effect of air pressure and temperature are small. However, if the aircraft flies at higher speeds, force and moments may also depend on Mach number due to the compressibility effect. Temperature, pressure, air density and speed of sound can be expressed in terms of the altitude by an International Standard Atmosphere (ISA) model by using the relations given in equations 2.25 - 2.28 [40, 46].

The air temperature decreases linearly with increasing altitude:

$$T = T_{SL} - hL \quad (2.25)$$

where

T : Air temperature (in [K])

$T_{SL}$  : Air temperature at sea level ( $T_{SL} = 288.15\text{K}$ )

h : Altitude above sea level (in [m])

L : Lapse rate ( $L = 0.0065 \text{ K/m}$ )

The static air pressure may be found by equation 2.26 :

$$\frac{P}{P_{SL}} = \left( \frac{T}{T_{SL}} \right)^{\frac{\gamma}{\gamma-1}} \quad (2.26)$$

Air density ( $\rho$ ) and speed of sound (a) are calculated by using the ideal gas relation (Equations 2.27 and 2.28).

$$\rho = \frac{P}{RT} \quad (2.27)$$

$$a = \sqrt{\gamma RT} \quad (2.28)$$

where R : Specific gas constant ( $R=287.0529 \text{ J/Kkg}$ )

## 2.8 Wind Gust Model

Wind gusts are included as external inputs which affect the body velocities of the aircraft for short durations. No separate subsystem is generated for these effects; however, they are directly implemented to the model as can be seen on the left lower part of Figure 2.5. In the simulation model, by using a switch, wind inputs can be defined in body or wind axes. The point is, if external inputs are given in wind axes, then a transformation from wind to body axes is required. Wind effects are defined in equation 2.29. Optionally, MATLAB<sup>®</sup> gust and turbulence models or wind - turbulence model presented in [27] can be used.

$$V_{wind} = \begin{bmatrix} u_{wind} \\ v_{wind} \\ w_{wind} \end{bmatrix} \quad (2.29)$$

## 2.9 Equations of Motion Model

Equations of motion express the motion of the aircraft in terms of external forces and moments. While deriving the 6-DOF general equations of motion following assumptions are made:

- The aircraft is assumed to be a rigid body.
- The airplane's mass is assumed to be constant.
- The curvature of the earth is neglected.
- The earth is assumed to be fixed in space.

### 2.9.1 Forces and Moments

In order to solve the nonlinear equations of motion implemented in the 6-DOF simulation model, first total force and moments are calculated. There are three main contributions to the external forces and moments considered in this block: aerodynamic forces and moments, contributions to the force due to thrust and force contributions from gravity. The non-dimensional

force and moment coefficients (equations 2.16 - 2.21) can be made dimensional by using equations 2.30 - 2.35.

$$X_A = C_{X_{cg}} qS \quad (2.30) \quad R_A = C_{R_{cg}} qSb \quad (2.33)$$

$$Y_A = C_{Y_{cg}} qS \quad (2.31) \quad M_A = C_{M_{cg}} qSc \quad (2.34)$$

$$Z_A = C_{Z_{cg}} qS \quad (2.32) \quad N_A = C_{N_{cg}} qSb \quad (2.35)$$

Thrust contribution is explained in Section 2.5 previously.

The contribution of the aircraft's weight to the forces are originally defined in earth-fixed frame. They are transformed to the body-fixed frame by a multiplication with direction cosine matrix (DCM). Force contributions from gravity along the body-axes of the aircraft are calculated as the Euler angles are already known. The contributions of the weight to the forces along the body-axes are given in equations 2.36 - 2.38.

$$X_G = -mg \sin \theta \quad (2.36)$$

$$Y_G = mg \cos \theta \sin \phi \quad (2.37)$$

$$Z_G = mg \cos \theta \cos \phi \quad (2.38)$$

## 2.9.2 6-DOF Equations of Motion

It is possible to express the aircraft dynamics as a set of nonlinear ordinary differential equations (ODEs). These 12 ODEs can be categorized in 4 groups as the following:

Force Equations :

$$\dot{u} = rv - qw - g \sin \theta + \frac{X_A + X_T}{m} \quad (2.39)$$

$$\dot{v} = -ru + pw + g \cos \theta \sin \phi + \frac{Y_A + Y_T}{m} \quad (2.40)$$

$$\dot{w} = qu - pv + g \cos \theta \cos \phi + \frac{Z_A + Z_T}{m} \quad (2.41)$$

Kinematic Equations:

$$\dot{\phi} = p + q \sin \phi \tan \theta + r \cos \phi \tan \theta \quad (2.42)$$

$$\dot{\theta} = q \cos \phi - r \sin \phi \quad (2.43)$$

$$\dot{\psi} = q \sin \phi \sec \theta + r \cos \phi \sec \theta \quad (2.44)$$

Moments Equations:

$$\dot{p} = \frac{I_{xz}}{I_{xx}I_{zz}-I_{xz}^2} \left[ (R_A + R_T) + I_{xz}pq - (I_{zz} - I_{yy})qr \right] \quad (2.45)$$

$$+ \frac{I_{xz}}{I_{xx}I_{zz}-I_{xz}^2} \left[ (N_A + N_T) - I_{xz}qr - (I_{yy} - I_{xx})pq \right]$$

$$\dot{q} = \frac{1}{I_{yy}} \left[ (M_A + M_T) - (I_{xx} - I_{zz})pr - I_{xz}(p^2 - r^2) \right] \quad (2.46)$$

$$\dot{r} = \frac{I_{xz}}{I_{xx}I_{zz}-I_{xz}^2} \left[ (R_A + R_T) + I_{xz}pq - (I_{zz} - I_{yy})qr \right] \quad (2.47)$$

$$+ \frac{I_{xz}}{I_{xx}I_{zz}-I_{xz}^2} \left[ (N_A + N_T) - I_{xz}qr - (I_{yy} - I_{xx})pq \right]$$

Navigation Equations:

$$\begin{aligned} \dot{X}_N &= u \cos \theta \cos \psi + v(-\cos \phi \sin \psi + \sin \phi \sin \theta \cos \psi) \\ &\quad + w(\sin \phi \sin \psi + \cos \phi \sin \theta \cos \psi) \end{aligned} \quad (2.48)$$

$$\begin{aligned} \dot{X}_E &= u \cos \theta \sin \psi + v(\cos \phi \cos \psi + \sin \phi \sin \theta \sin \psi) \\ &\quad + w(-\sin \phi \cos \psi + \cos \phi \sin \theta \sin \psi) \end{aligned} \quad (2.49)$$

$$\dot{h} = u \sin \theta - v \sin \phi \cos \theta - w \cos \phi \cos \theta \quad (2.50)$$

## 2.10 Actuator Models

Actuators of an aircraft take the commanded control surface deflections and throttle setting generated by the pilot or the automatic flight control system as inputs. However, while returning the actual controls as outputs, they may affect the closed loop performance due to their own dynamics. Therefore, they play an important role in control studies and should be modeled correctly.

In the thesis, actuator dynamics are first assumed to be fast enough when compared to the aircraft itself and modeled as first order systems (Equation 2.51). Corner frequency ( $a$ ) of each actuator is selected by examining the open loop dynamics of the UAV. Considering the longitudinal and lateral modes of the UAV (Section 3.4.2),  $a$  is selected as 40 rad/s for elevator, 35 rad/s for engine and 15 rad/s for aileron and rudder actuators.

$$K_{act}(s) = \frac{a}{a + T} \quad (2.51)$$

Next, actuator limits for each control are obtained by examining the real UAV. In Table 2.5, angle and rate limits for the elevator, aileron and rudder actuators are listed. In addition to the values given in this table, maximum percent throttle and its rate are limited to 0-100 % and 200 %/s, respectively.

Table 2.5: Actuator Limits

	Elevator	Aileron	Rudder
Angle Limits (deg)	$\pm 20$	$\pm 20$	$\pm 15$
Rate Limits (deg/s)	$\pm 100$	$\pm 100$	$\pm 100$

After modeling the actuators, functional tests are performed to check the correctness of these models. Using the simulation model, the UAV is commanded to fly steady wings level. During the simulation, first a horizontal, then a vertical and finally a lateral wind gust are applied for short durations. Control inputs generated by the flight control system are used in the functional tests and it is seen that, the real controls of the UAV are able to follow the commands.

## CHAPTER 3

### TRIM AND LINEARIZATION ANALYSES

This chapter describes the trim and linearization tools developed and presents the results obtained for two different aircrafts, Cessna 172 and Rascal 110. Chapter begins with a discussion on the trim algorithm, which drives the forces and moments of the aircraft equal to zero at a specified flight condition, and continues with the linearization method used to obtain the linear aircraft model. Validation of simulation, trim and linearization algorithms is accomplished by using an existing airplane's data found in the literature, namely Cessna 172, and the results are presented. Chapter ends with the trim and linearization results of the UAV and a discussion on open loop system characteristics.

#### 3.1 Trim Analyses

Linearization of the 6-DOF nonlinear aircraft model plays an important role in controller design and stability analyses. Since linearization requires the reference flight conditions, first a trim algorithm is developed. The trim algorithm is based on the minimization of a cost function which makes the forces and moments of the aircraft equal to zero at a given flight condition, posed as equality constraints to the optimization routine. Two flight regimes, the steady wings-level and steady coordinated / uncoordinated turning flights are considered in the trim algorithm.

### 3.1.1 Steady State Flight Conditions

The 6-DOF nonlinear equations of motion were discussed in Section 2.9.2 previously. These equations may be written as in the form of equation 3.1.

$$\dot{x} = f(x(t), u(t), t) \quad (3.1)$$

In order to obtain the trim points, also known as the equilibrium points, a more general form should be considered. A trim point of an autonomous, time-invariant system may be defined as in equation 3.2 [45]. When all of the time derivatives are zero, the system is said to be 'at rest'.

$$f(\dot{x}, x(t), u(t)) = 0 \quad \dot{x} = 0 \quad \text{and} \quad u = 0 \quad \text{or} \quad \text{constant} \quad (3.2)$$

Since a trim point is a steady state point of a dynamic system [47], first the steady state flight conditions should be defined. In steady state flight, all accelerations are zero and all of the motion variables are constant or zero. This general condition for steady state flight is given in equation 3.3. Additional constraints are given in equations 3.4 - 3.7.

General condition:

$$\dot{u} = \dot{v} = \dot{w} = \dot{p} = \dot{q} = \dot{r} = 0 \quad (3.3)$$

Steady, straight wings-level flight:

$$\phi = \dot{\phi} = \dot{\theta} = \dot{\psi} = 0 \quad (3.4)$$

Steady turning flight:

$$\dot{\phi} = \dot{\theta} = 0 \quad \dot{\psi} = \text{turn rate} \quad (3.5)$$

Steady pull-up:

$$\phi = \dot{\phi} = \dot{\psi} = 0 \quad \dot{\theta} = \text{pull-up rate} \quad (3.6)$$

Steady roll:

$$\dot{\psi} = \dot{\theta} = 0 \quad \dot{\phi} = \text{roll rate} \quad (3.7)$$

Finding the steady state flight conditions requires the solution of nonlinear state equations. This problem is handled by a numerical optimization algorithm based on iterative solutions of the independent state and control variables which are adjusted during the trim process. Details of this trim routine are presented in the next section.

### 3.1.2 Trim Method

The trim routine is an optimization based algorithm that determines the steady state flight conditions for two different flight regimes, the steady wings-level and steady coordinated / uncoordinated turning flights. The trim routine solves the nonlinear state equations for the state ( $x$ ) and control ( $u$ ) vectors.

$$x = \begin{bmatrix} u & v & w & p & q & r & \phi & \theta & \psi & X_N & X_E & h \end{bmatrix}^T \quad u = \begin{bmatrix} \delta_{elev} & \delta_{ail} & \delta_{rud} & \delta_{th} \end{bmatrix}^T \quad (3.8)$$

To obtain the trim conditions, first the flight conditions are needed to be specified. According to these flight conditions, parameters are divided into two categories: trim constants and trim variables. Trim constants include the parameters that will be kept constant during the trim process. These are  $u$ ,  $h$ ,  $\gamma$  and other states and state derivatives that change according to the steady state flight trim conditions given in equations 3.4 - 3.7. Trim variables are the independent states,  $v$  and  $w$ , and the control inputs,  $\delta_{elev}$ ,  $\delta_{ail}$ ,  $\delta_{rud}$  and  $\delta_{th}$ . Idea of the trim is to find the trim variables that drive the forces and moments of the aircraft equal to zero. For this purpose, a Matlab<sup>®</sup> minimization routine is used. This minimization routine tries to find  $x$  and  $u$  which minimize the scalar cost function given in equation 3.9. This cost function is formed according to the general steady state flight conditions given in equation 3.3; hence, can be used for different flight regimes.

$$J = c_1 \dot{u}^2 + c_2 \dot{v}^2 + c_3 \dot{w}^2 + c_4 \dot{p}^2 + c_5 \dot{q}^2 + c_6 \dot{r}^2 \quad (3.9)$$

where  $c_1 \dots c_6$  are weighting parameters.

For steady state turning flight, the turn is specified by the yaw rate,  $\dot{\psi}$ . If it is a coordinated turn, required roll angle is computed by the coordinated turn constraint given in equations 3.10 - 3.13 [45].  $p$ ,  $q$  and  $r$  are determined by the kinematic relations derived in Section 2.9.2.

$$\tan \phi = G \frac{\cos \beta (a - b^2) + b \tan \alpha \sqrt{c(1 - b^2) + G^2 \sin^2 \beta}}{\cos \alpha (a^2 - b^2(1 + c \tan^2 \alpha))} \quad (3.10)$$

where

$$a = 1 - G \tan \alpha \sin \beta, \quad b = \frac{\sin \gamma}{\cos \beta}, \quad c = 1 + G^2 \cos^2 \beta \quad (3.11)$$

when the flight path angle,  $\gamma$ , is zero, equation 3.10 reduces to:

$$\tan \phi = G \frac{\cos \beta}{\cos \alpha - G \sin \alpha \sin \beta} \quad (3.12)$$

and when  $\beta$  is small, equation 3.12 reduces to:

$$\tan \phi = \frac{G}{\cos \alpha} \quad (3.13)$$

For both steady state wings-level and turning flights, trim algorithm begins with evaluation of the cost function around an initial point. The simulation model is run in compile mode by using Matlab<sup>®</sup> 'feval' function and the cost function is calculated by using current values of the state derivatives.  $\phi$  is evaluated by using equation 3.13 and  $p, q, r$  are calculated from the kinematic relations. Current  $x$  and  $u$  vectors are found and used to run the simulation model once more to compute the cost function and obtain new  $x$  and  $u$ . Iterations are continued until the error tolerance for the cost function is satisfied and required trim conditions are obtained.

## 3.2 Linearization

### 3.2.1 Linearization Method

As mentioned in Section 3.1, linearization of the 6-DOF nonlinear aircraft model is a crucial step for creating the linear state space model to be used in the development of the flight control algorithms. Once the linear model is obtained, system analysis can be performed more easily when compared to the complex nonlinear system analysis. Linear systems can be used to examine the stability characteristics of the dynamic system, i.e. eigenvalues of the system, system responses to step inputs, and to design the control algorithms.

Linearization is performed around an operating point for which all the state derivatives must be chosen [22]. The best results can be obtained by selecting this operating point as the trim point defined by state ( $x$ ) and input ( $u$ ) vectors given in equation 3.8.

In the thesis, linear system model is obtained by using 'linmod' command of Matlab<sup>®</sup>. In addition, a separate code is also generated. This linearization routine uses the nonlinear simulation code and carries out numerical differentiation based on small disturbances to derive the state ( $A$ ) and input ( $B$ ) matrices. However, results showed that the state space model obtained

by 'linmod' command is more accurate for certain parameters of  $A$  and  $B$ . Hence, 'linmod' is used for the linearization analyses.

A Taylor Series expansion can be used to compute the linear state space model [31]. This linearization process is based on an assumption. State and input variables are perturbed around the equilibrium point to find the rate of change of  $x$  and  $u$  (Jacobians), so only first-order terms are kept, squares and products are assumed to be negligible. First order Taylor Series expansion for  $n$  independent variables about an equilibrium point is given in equation 3.14.

$$f(x_1, x_2, \dots, x_n) \approx f(x_1, x_2, \dots, x_n)_{ref} + \left. \frac{\partial f}{\partial x_1} \right|_{ref} \Delta x_1 + \left. \frac{\partial f}{\partial x_2} \right|_{ref} \Delta x_2 + \dots + \left. \frac{\partial f}{\partial x_n} \right|_{ref} \Delta x_n + \underbrace{H.O.T}_0 \quad (3.14)$$

In equations 3.15-3.16, linear state-space form is given. Here, the Jacobian matrices  $A$ ,  $B$ ,  $C$ , and  $D$  are the state, input, output and direct transmission matrices, respectively [31].

$$\Delta \dot{x} \triangleq A \Delta x + B \Delta u \quad (3.15)$$

$$\Delta y \triangleq C \Delta x + D \Delta u \quad (3.16)$$

where  $\Delta x = x - x_{eq}$  or  $\Delta x = x - x_{trim}$

$$A = \begin{bmatrix} \left. \frac{\partial f_1}{\partial x_1} \right|_{x_{eq}, u_{eq}} & \left. \frac{\partial f_1}{\partial x_2} \right|_{x_{eq}, u_{eq}} & \dots & \left. \frac{\partial f_1}{\partial x_n} \right|_{x_{eq}, u_{eq}} \\ \left. \frac{\partial f_2}{\partial x_1} \right|_{x_{eq}, u_{eq}} & \left. \frac{\partial f_2}{\partial x_2} \right|_{x_{eq}, u_{eq}} & \dots & \left. \frac{\partial f_2}{\partial x_n} \right|_{x_{eq}, u_{eq}} \\ \vdots & \vdots & \vdots & \vdots \\ \left. \frac{\partial f_n}{\partial x_1} \right|_{x_{eq}, u_{eq}} & \left. \frac{\partial f_n}{\partial x_2} \right|_{x_{eq}, u_{eq}} & \dots & \left. \frac{\partial f_n}{\partial x_n} \right|_{x_{eq}, u_{eq}} \end{bmatrix} \quad (3.17)$$

$$\bar{B} = \begin{bmatrix} \left. \frac{\partial f_1}{\partial u_1} \right|_{x_{eq}, u_{eq}} & \dots & \left. \frac{\partial f_1}{\partial u_n} \right|_{x_{eq}, u_{eq}} \\ \left. \frac{\partial f_2}{\partial u_1} \right|_{x_{eq}, u_{eq}} & \dots & \left. \frac{\partial f_2}{\partial u_n} \right|_{x_{eq}, u_{eq}} \\ \vdots & \vdots & \vdots \\ \left. \frac{\partial f_n}{\partial u_1} \right|_{x_{eq}, u_{eq}} & \dots & \left. \frac{\partial f_n}{\partial u_n} \right|_{x_{eq}, u_{eq}} \end{bmatrix} \quad (3.18)$$

### 3.2.2 Uncoupled Dynamics

If the coupling effects between the longitudinal and lateral airplane dynamics are negligible, separate longitudinal and lateral models would be sufficient to describe the airplane motion. Full system linearization results of both Cessna 172 and Rascal 110 airplanes showed that longitudinal responses to lateral controls and lateral responses to longitudinal controls are almost zero. Hence, longitudinal states and controls are manually decoupled from the lateral states and controls. State, input and output matrices for the uncoupled system is given in equations 3.19-3.24.

$$x_{long} = \begin{bmatrix} u \text{ (m/s)} \\ w \text{ (m/s)} \\ q \text{ (deg/s)} \\ \theta \text{ (deg)} \end{bmatrix} \quad (3.19) \quad u_{long} = \begin{bmatrix} \delta_{elev} \text{ (deg)} \\ \delta_{th} \text{ (\%max)} \end{bmatrix} \quad (3.20) \quad y_{long} = \begin{bmatrix} u \text{ (m/s)} \\ w \text{ (m/s)} \\ q \text{ (deg/s)} \\ \theta \text{ (deg)} \end{bmatrix} \quad (3.21)$$

$$x_{late} = \begin{bmatrix} v \text{ (m/s)} \\ p \text{ (deg/s)} \\ r \text{ (deg/s)} \\ \phi \text{ (deg)} \\ \psi \text{ (deg)} \end{bmatrix} \quad (3.22) \quad u_{late} = \begin{bmatrix} \delta_{ail} \text{ (deg)} \\ \delta_{rud} \text{ (deg)} \end{bmatrix} \quad (3.23) \quad y_{late} = \begin{bmatrix} v \text{ (m/s)} \\ p \text{ (deg/s)} \\ r \text{ (deg/s)} \\ \phi \text{ (deg)} \\ \psi \text{ (deg)} \end{bmatrix} \quad (3.24)$$

## 3.3 Validation of Simulation, Trim and Linearization Tools

### 3.3.1 Trim Results

To validate the simulation model and the trim algorithm, a Cessna 172 airplane data found in the literature is used. This airplane is trimmed at an altitude of 1524 m and a velocity of 66 m/s [39]. Figure 3.1 shows the simulation results for steady wings-level flight during 10 seconds. These results show that the aircraft when started at the trim flight conditions, maintains its altitude, attitude, and trim flight velocity without any deviations in the lateral channel.

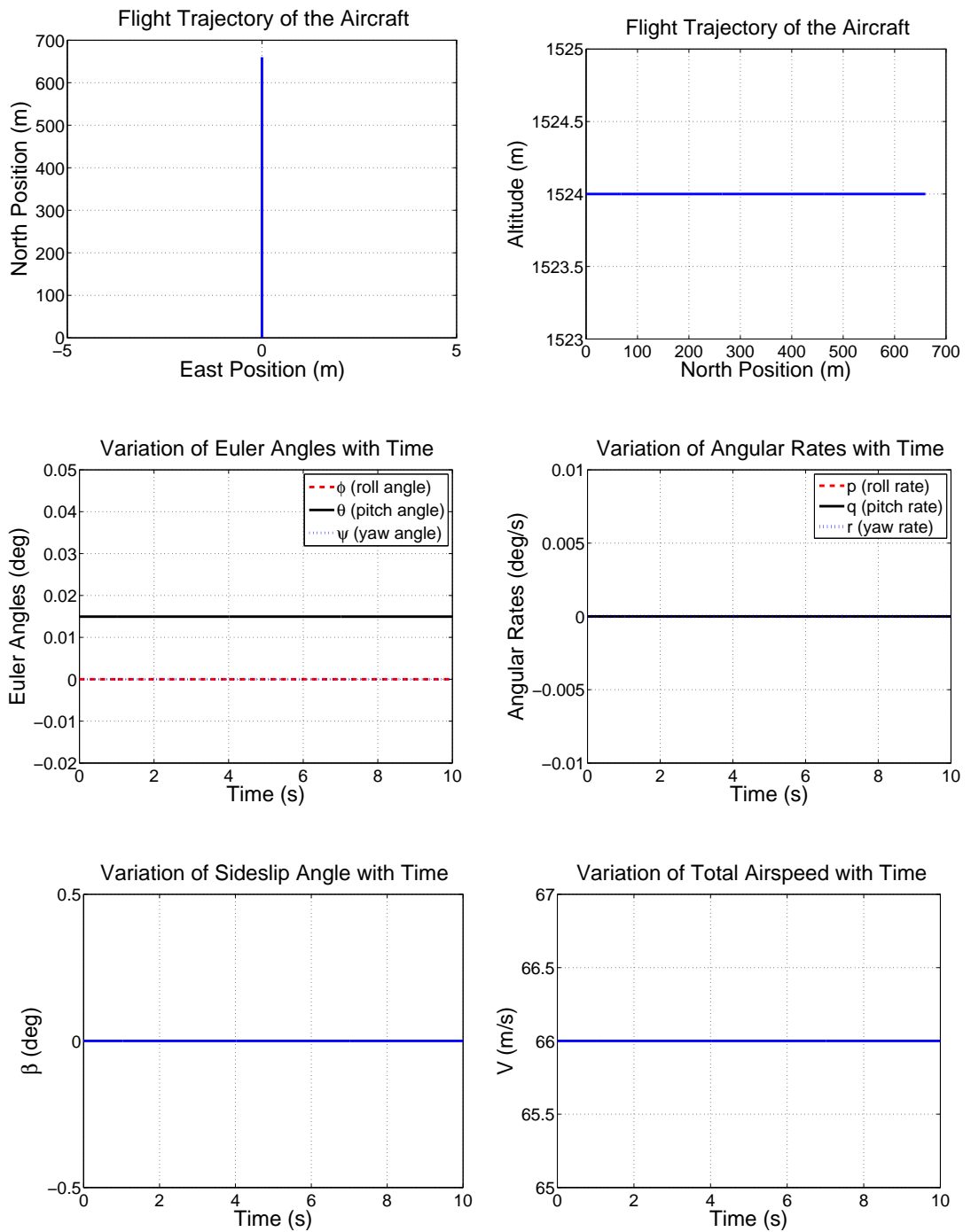


Figure 3.1: Simulation Results of Cessna 172 for Steady Wings-level Flight

### 3.3.2 Linearization Results

Linear model is obtained by using the trimmed flight conditions as the reference inputs. Eigenvalues of the longitudinal and lateral modes are presented in Table 3.1 together with those given in Ref [39]. As it may be observed from this table, the linearization results are quite close to those presented in the literature, validating the correctness of the simulation, trim and linearization algorithms.

Table 3.1: Comparison of Eigenvalues for Cessna 172 Airplane Flying at 1524 m with 66 m/s

Eigenvalues obtained from the nonlinear simulation	Eigenvalues given in Ref [39]
Longitudinal	Longitudinal
$-4.1256 \pm 4.4264i$	$-4.130 \pm 4.390i$
$-0.0165 \pm 0.1537i$	$-0.0209 \pm 0.1797i$
Lateral	Lateral
-12.433	-12.43
$-0.6933 \pm 3.3040i$	$-0.6858 \pm 3.306i$
-0.0105	-0.0109

## 3.4 Trim and Linearization Results of the UAV

### 3.4.1 Trim Results

After validation of the simulation, trim and linearization algorithms, the Rascal simulation model is trimmed for two flight regimes, namely, steady wings-level and coordinated turn flights, at an altitude of 1000 m and a velocity of 20 m/s. To demonstrate the effectiveness of the trim, the nonlinear simulation code is run with trim flight inputs as initial conditions. Both the wings-level and steady turning flights are observed to hold the trim conditions. An example is given for a coordinated turn in Figure 3.2. The aircraft completes the loop while maintaining its altitude, and the desired turn rate is acquired without and sideslip. On the other hand, Figure 3.3 shows the system response to 5 degrees of elevator doublet. Note that the states are constant until the elevator input. As can be seen, only pitch rate, pitch angle, angle of attack, velocity and altitude change with respect to the elevator inputs. There is no deviation to the East, indicating a straight flight path in a northerly heading. All the results are as expected for the input command, verifying that the system is stable and the correct trim conditions are obtained.

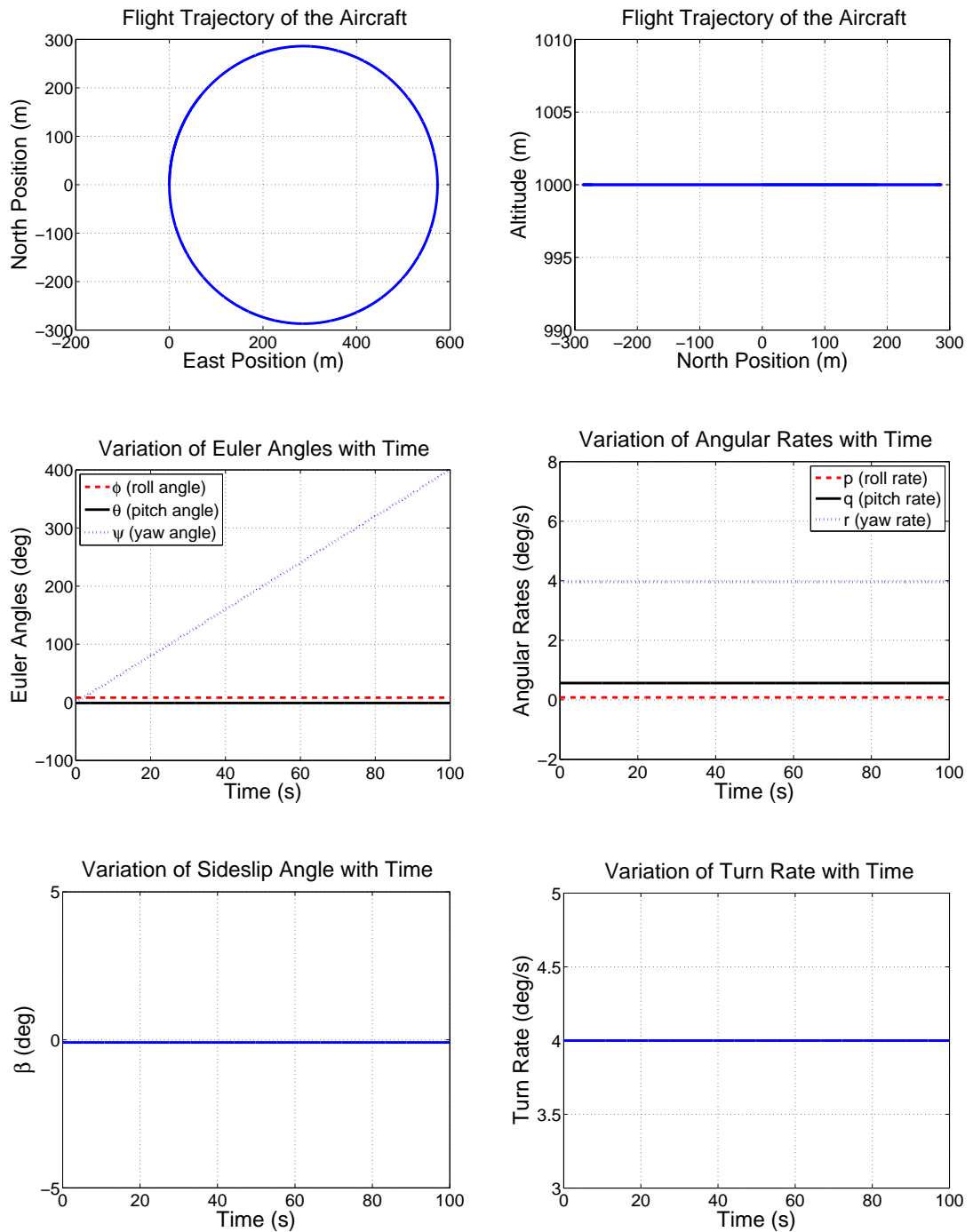


Figure 3.2: Nonlinear Simulation Results for Coordinated Turn Flight of Rascal at Trimmed Flight

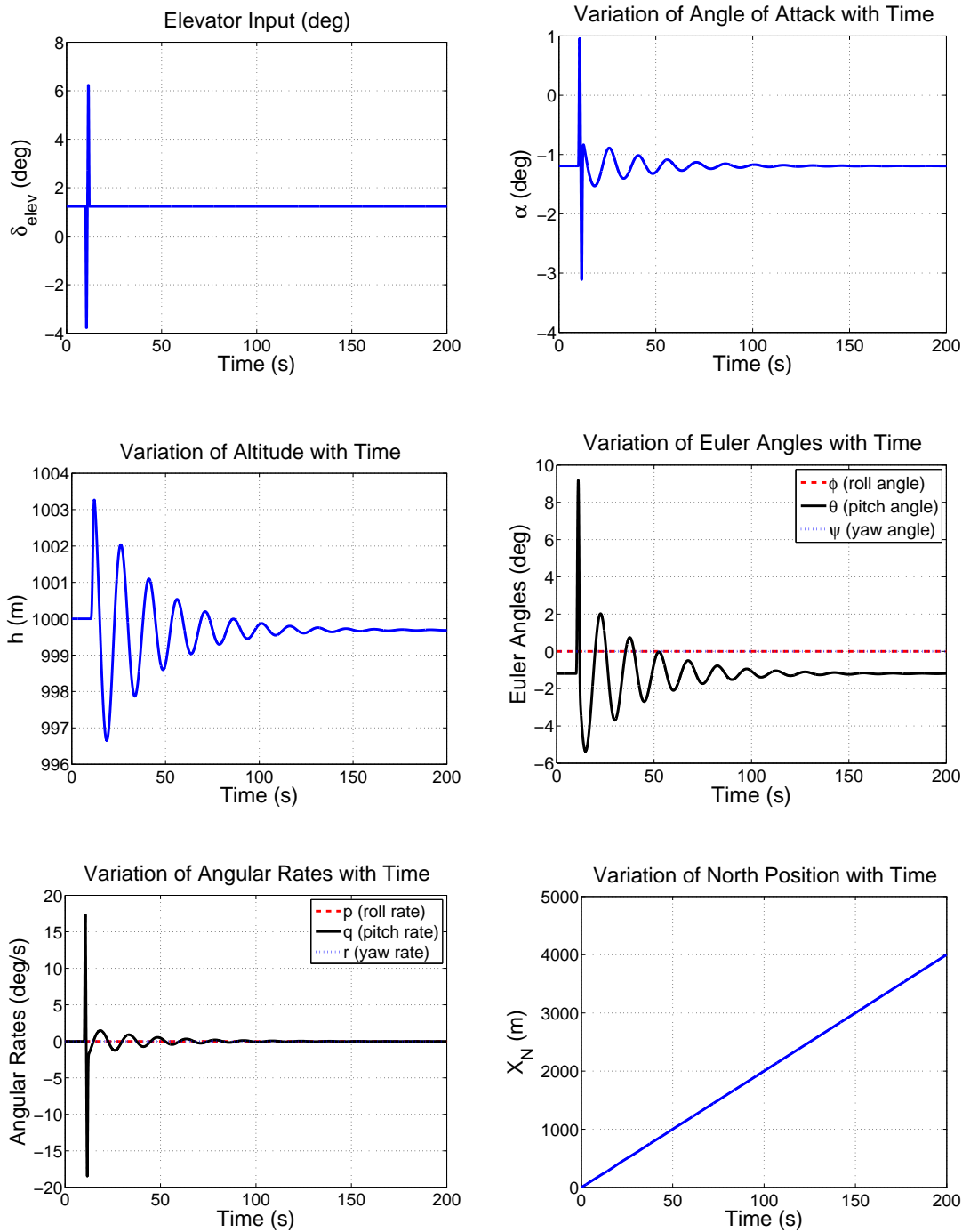


Figure 3.3: Simulation Results of Rascal after 5 degrees of Elevator Doublet

### 3.4.2 Linearization Results

After the trim conditions are obtained, linearization is performed. The linearized matrices can be found in Appendix C. Eigenvalues of the longitudinal and lateral modes of Rascal flying at 1000 m with 20 m/s wings level are computed and given in Table 3.2. As can be seen from this table, the UAV is stable since the real parts of the eigenvalues are all negative.

Table 3.2: Eigenvalues of Rascal for 20 m/s Wings-level Flight at 1000m

Longitudinal Eigenvalues	Lateral Eigenvalues
$-7.7276 + 2.3562i$	$-8.5525$
$-7.7276 - 2.3562i$	$-0.3437 + 2.7040i$
$-0.0414 + 0.3114i$	$-0.3437 - 2.7040i$
$-0.0414 - 0.3114i$	$-0.0896$

Longitudinal modes are the short period and phugoid modes. These modes are both oscillatory and observable through perturbations in longitudinal (u) and vertical (w) speeds, pitch rate (q), and pitch angle ( $\theta$ ). The short period mode is heavily damped whereas the phugoid mode has a smaller damping ratio. These modes are controllable through elevator deflection and throttle input. Longitudinal mode characteristics are given in Table 3.3.

Table 3.3: Longitudinal Mode Characteristics of Rascal

Mode	Roots	Natural Frequency $\omega_n$ [rad/s]	Damping Ratio $\zeta$
Short Period	$-7.7276 \pm 2.3562i$	8.08	0.957
Phugoid	$-0.0414 \pm 0.3114i$	0.314	0.132

The lateral modes are the roll, dutch roll and spiral modes. Only the dutch roll mode is oscillatory. These modes are observable through perturbations in lateral speed (v), roll (p) and yaw (r) rates, and roll angle ( $\phi$ ). These modes are controllable through aileron and rudder deflections. Lateral mode characteristics are given in Table 3.4 and 3.5.

Table 3.4: Dutch Roll Mode Characteristics of Rascal

Mode	Roots	Natural Frequency $\omega_n$ [rad/s]	Damping Ratio $\zeta$
Dutch Roll	$-0.3437 \pm 2.7040i$	2.73	0.126

Table 3.5: Roll and Spiral Mode Characteristics of Rascal

Mode	Roots	Time Constant [s]	Time to Half Amplitude [s]
Roll	-8.5525	0.1169	0.081
Spiral	-0.0896	11.1607	7.7344

### 3.5 Validation of the Linear Model

Linear model of the UAV used for development of the flight control systems is validated by comparing the system response with the nonlinear model response for separate step and doublet inputs (Figures 3.4, 3.6 and 3.8). For this aim, the linearized system matrices given in Appendix C are used and the correctness of the linear model is tested by disturbing the airplane from its trim flight condition (steady wings-level flight at an altitude of 1000 m and a velocity of 20 m/s). As can be seen from the results illustrated in Figures 3.5, 3.7 and 3.9, responses of linear and nonlinear models to different control inputs are similar as expected.

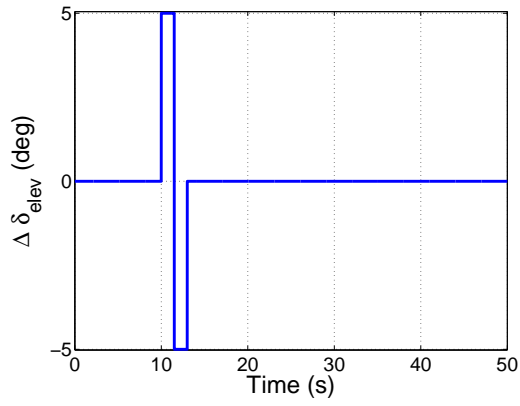


Figure 3.4: Variation of Elevator Deflection with Time

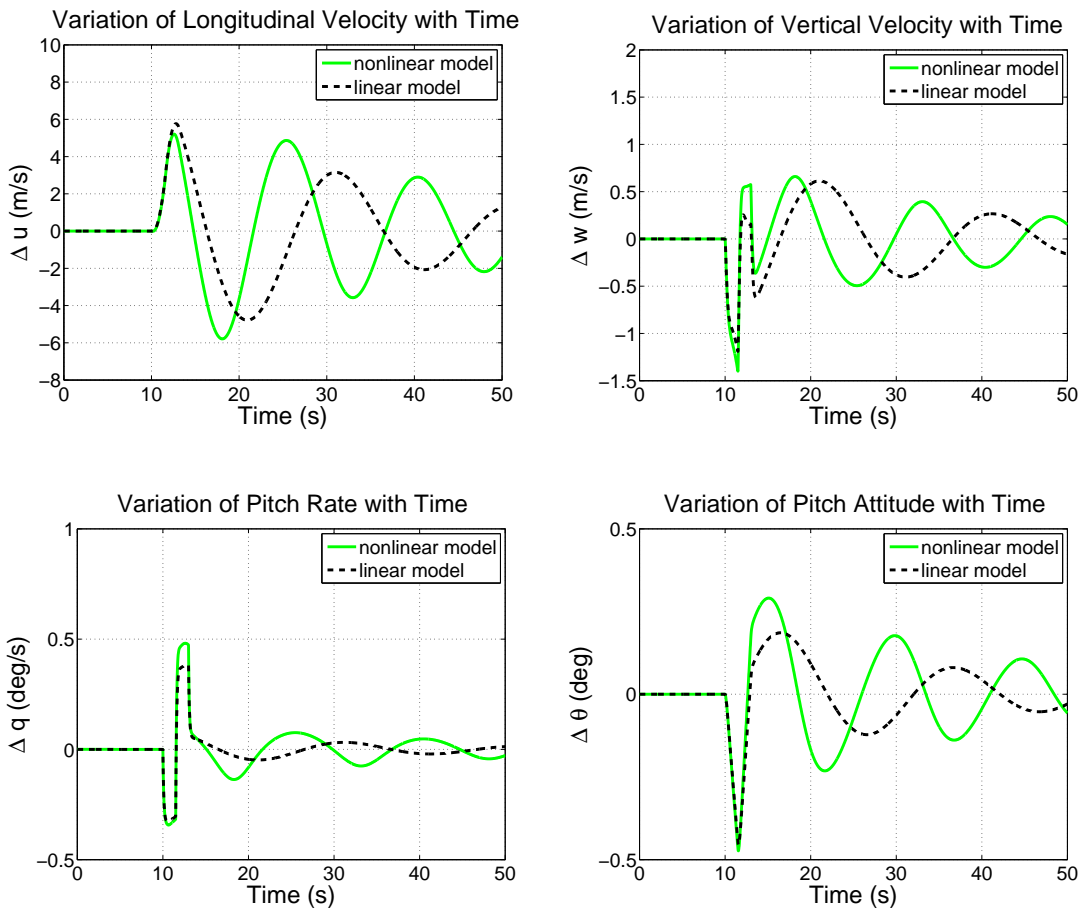


Figure 3.5: Linear and Nonlinear Simulation Results for 5 degrees of Elevator Doublet Input

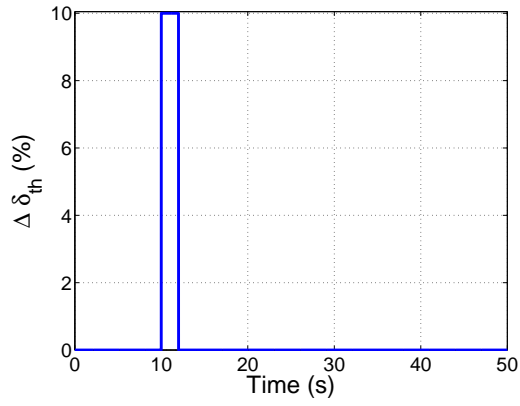


Figure 3.6: Variation of Percent Throttle with Time

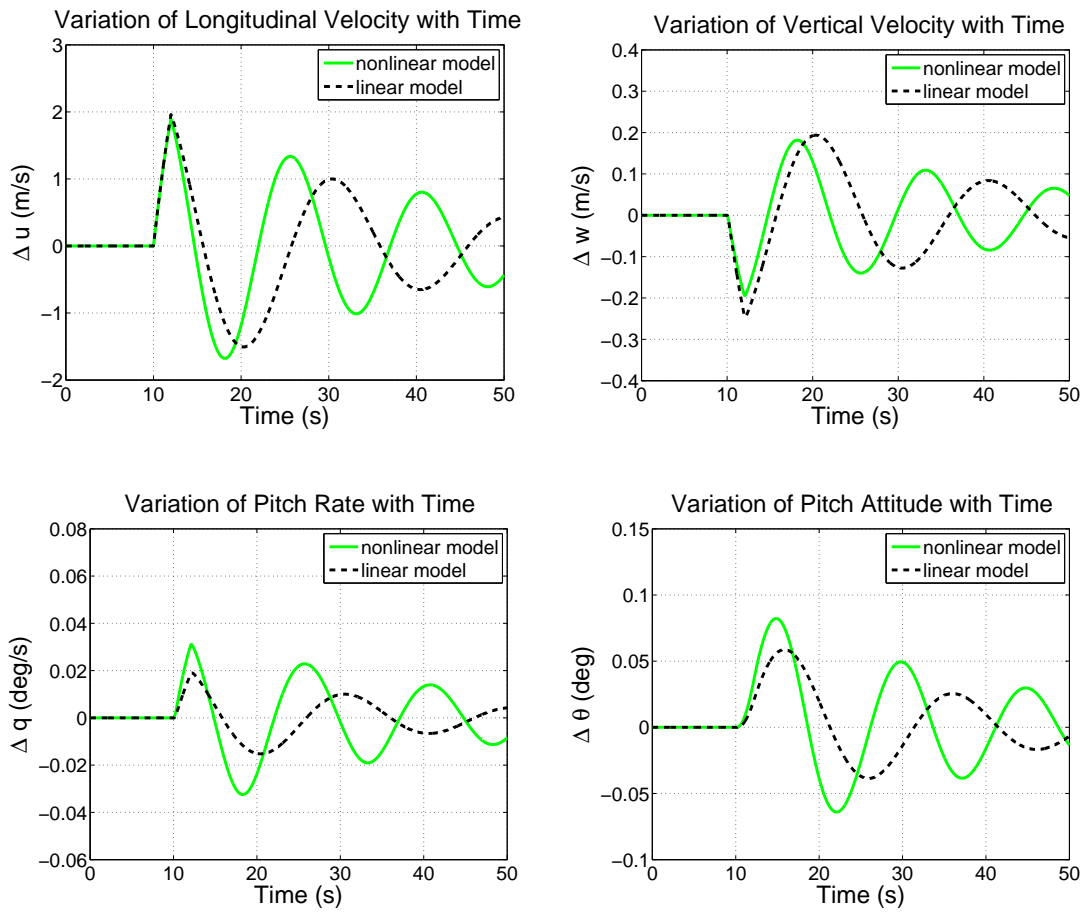


Figure 3.7: Linear and Nonlinear Simulation Results for 10 % of Throttle Step Input

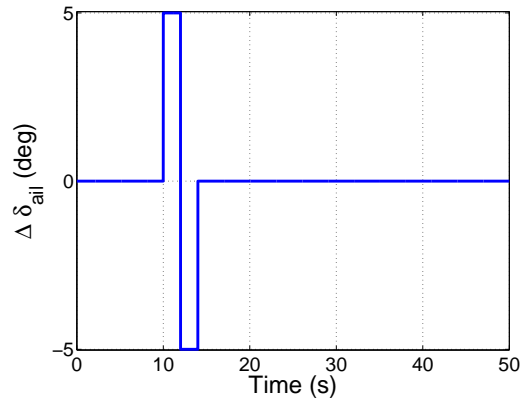


Figure 3.8: Variation of Aileron Deflection with Time

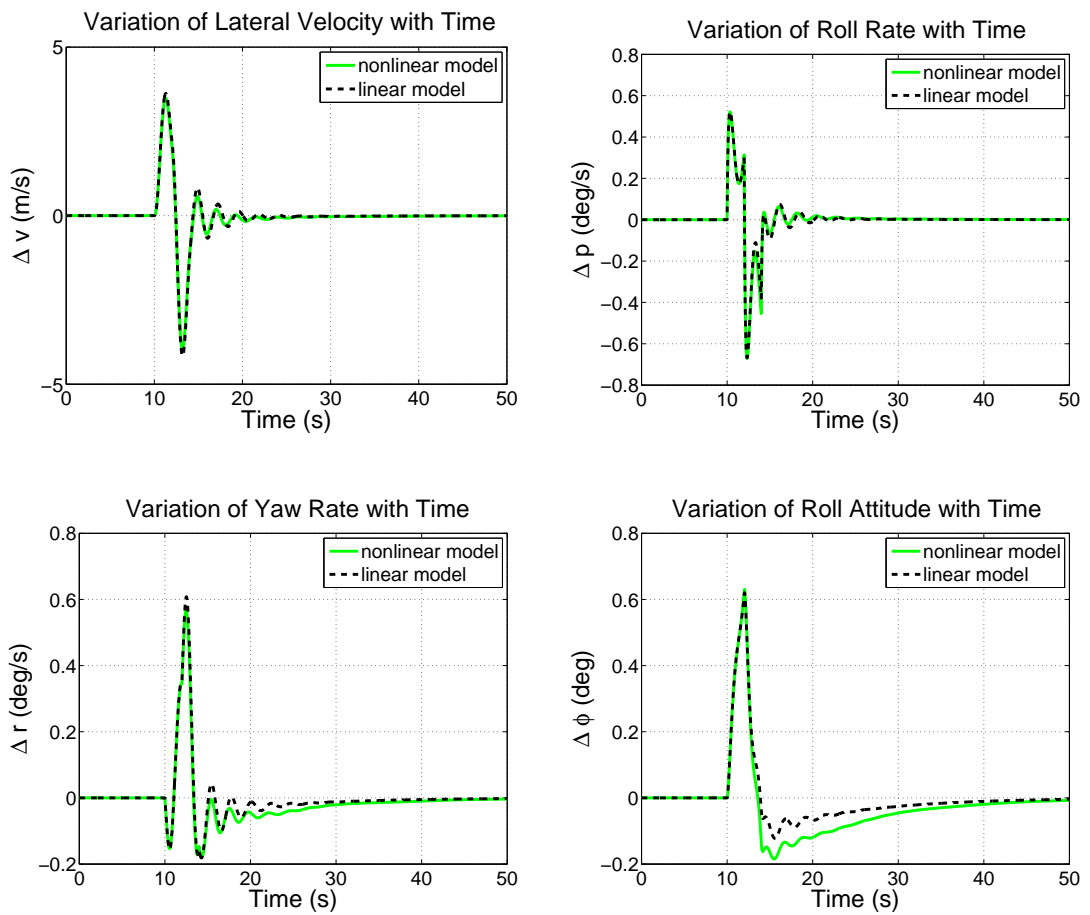


Figure 3.9: Linear and Nonlinear Simulation Results for 5 degrees of Aileron Doublet Input

## CHAPTER 4

### CONTROLLER DESIGNS FOR THE CONVENTIONAL UAV

This chapter explains the different linear controller design methods used for autopilots of the conventional UAV. First, PID classical controller design method and tuning rules are discussed. Then the configurations of both longitudinal and lateral autopilots are described. Next, robust controller design method is explained and robust autopilots are discussed in detail. Configurations of the controllers, weighting functions used in the designs, step responses of the controllers and results of  $\mu$ -analyses are presented for both longitudinal and lateral robust controllers.

#### 4.1 PID Classical Controller Design

Using classical PID controllers for flight control system designs is an extensive application for control studies. Mostly, a linear time invariant (LTI) system, which is an approximation to the nonlinear time varying system, is used to design the controllers and also for their analyses [17]. Control methods are based on frequency domain analyses of the system and single-input-single-output (SISO) techniques provide simpler stability analyses for the controller designs.

##### 4.1.1 PID Classical Control Method

In the thesis, classical PID control approach is used to minimize the tracking errors. Negative linear feedback is used for both longitudinal and lateral autopilots, and effects of signal uncertainties (unknown disturbances) as well as modeling uncertainties are tried to be minimized.

Transfer function of a PID controller is given in equation 4.1.

$$K_{PID}(s) = K_p + \frac{K_i}{s} + K_d s \quad (4.1)$$

The proportional term (P) is used to reduce the rise time; however, it increases the effect of sensor noises at high frequencies. In addition, it reduces the steady-state error; however, cannot eliminate it completely. Therefore, an integral term (I) is needed for complete elimination of the error. When an integral term is used, it adds a pole at the origin. This yields an infinite gain at zero frequency [21] which prevents the accumulation of errors. The disadvantage of using an integral controller is, it slows the response of the system while forcing the error to be zero. If desired, system response can be accelerated through using a derivative term (D). Although this term has no effect on the steady-state errors, it speeds up the response, reduces the settling time as opposed to the integral action, and also reduces the overshoot [50].

In the thesis, all P, PI and PID type controllers are used. Mostly, simulations with PI controllers are found to give satisfactory results; however, in some channels a derivative term is also added to decrease the settling time and overshoot of the response, and to obtain better transient performance. When required, state derivative is calculated from the nonlinear simulation model whereas desired state derivative is obtained from the command filters. Then, the difference between these signals, which is the derivative of the error, is fed to the D controller. Consequently, PID controllers are used instead of PI controllers when it is desired to improve both steady-state response and transient characteristics of the system [37].

#### 4.1.2 Controller Gains and Tuning

Classical PID controller gains can be determined if the dynamics can be modeled as first or second order transfer functions. Otherwise, the parameters can be tuned manually [8]. However, before manual tuning, one of the techniques presented in the literature can be used. Zieger-Nichols rules are widely used for tuning the gains of PID controllers. In addition, other techniques, such as automatic tuning methods, analytical and graphical approaches, and optimization algorithms which find the set of parameters that satisfy the best possible performance, are present in the literature.

Transfer function of a PID controller is shown in equation 4.2.  $K_p$ ,  $T_i$  and  $T_d$  represent the proportional gain, integral time and derivative time, respectively. These values can be

determined from the tuning rules of Ziegler-Nichols explained in Ref [4, 5, 9]. Additionally, in Ref [37], Ziegler-Nichols tuning methods are also discussed. First method is based on step response of the plant, whereas the second method is based on the critical gain and critical period. Critical gain ( $K_{cr}$ ) is the maximum proportional controller gain and critical period ( $P_{cr}$ ) is the corresponding period of oscillations, both determined experimentally.

$$K_{PID}(s) = K_p(1 + \frac{1}{T_i s} + T_d s) \quad (4.2)$$

Ziegler-Nichols tuning rules are very useful even if the plant dynamics are not known. Moreover, these methods can also be used for complicated systems, such as aircrafts, and controller gains can be found by applying one of the methods described in Ref [37]. The point is, step response of a PID controller tuned by Ziegler-Nichols rules generally has 10% ~ 60% maximum overshoot. However, by fine tuning it is possible to obtain the desired closed loop response. Thus, Ziegler- Nichols tuning rules are very effective to find the initial points for fine tuning of a PID controller.

In the thesis, in order to find the PID controller gains, first the Ziegler-Nichols rules are applied to the SISO models. If the responses of the plants with the PID controllers tuned by Ziegler-Nichols rules were obtained as desired, the gains might not be changed. However, results showed that for both longitudinal and lateral PID controllers, the stability margins of the closed-loop systems were small; the responses were oscillatory and had high overshoots. Hence, desired response characteristics like rise time, settling time, overshoot behaviors [29] are obtained by adjusting the parameters of the PID controllers manually. Furthermore, fine tuning of the controllers are accomplished by also using Matlab<sup>®</sup> - Simulink<sup>®</sup> 'Optimization Technique: Signal Constraint' when necessary.

Both longitudinal and lateral autopilots are designed for the linear UAV model and then tested through nonlinear simulations. Due to changes in the flight conditions and response characteristics of the aircraft, gain scheduling may have been needed. In order to check the necessity of such an approach, first the PID controllers are designed about an initial trim point of 1000 m and 20 m/s. Then, these PID controllers are tested for different flight conditions which led to satisfactory results. Since altitude and velocity changes are small, they have little effect on the aerodynamic database. Hence, the derivatives remain nearly the same and aircraft modes are not affected extensively. This yields almost generic autopilots for the whole flight envelope of the UAV. Therefore, gain scheduling is not used.

### 4.1.3 Command Filters

Command filters are low pass filters which basically represent the desired response of the aircraft. They are used to shape the command signals to match the dynamics of the aircraft. Since they smoothen the command inputs, the tracking performance of the aircraft is improved [35] and it would be able to follow the inputs. In addition, as low pass filters, they limit the actuator deflection rates; remove high frequency components from the command signals and, as a result, lower the overshoot of the response in the respective channels. The transfer function of a first order command filter is shown in equation 4.3.

$$K_{filter}(s) = \frac{b}{s + b} \quad (4.3)$$

In the thesis, for both longitudinal and lateral autopilots first order command filters are utilized. For the longitudinal controller, command filters are present in inner and outer loops, whereas, for the lateral controller they are used for the outer loops. It is worth to mention that, they do not have a destabilizing effect on the controllers [16]. They are adjusted according to the dynamic characteristics of the aircraft. First, it is checked whether the elevator, aileron, rudder and throttle rates are within the actuator limits or not. When limits are satisfied, then, the system response is tried to be improved without slowing it down or demanding more than the aircraft can achieve.

### 4.1.4 Longitudinal Autopilot

Longitudinal flight control system design is carried out by using classical PID controller techniques. For inner and outer loops, classical sequential loop closing methods are applied and the inputs are smoothened by the command filters. Inputs of the longitudinal autopilot are the required altitude and velocity, and outputs are the elevator deflection and throttle. Control signals generated by the controller are finally sent to the corresponding actuators. The block diagram of the longitudinal control system developed in Simulink<sup>®</sup> is depicted in Figure 4.1 and controller gains are given in Table 4.1.

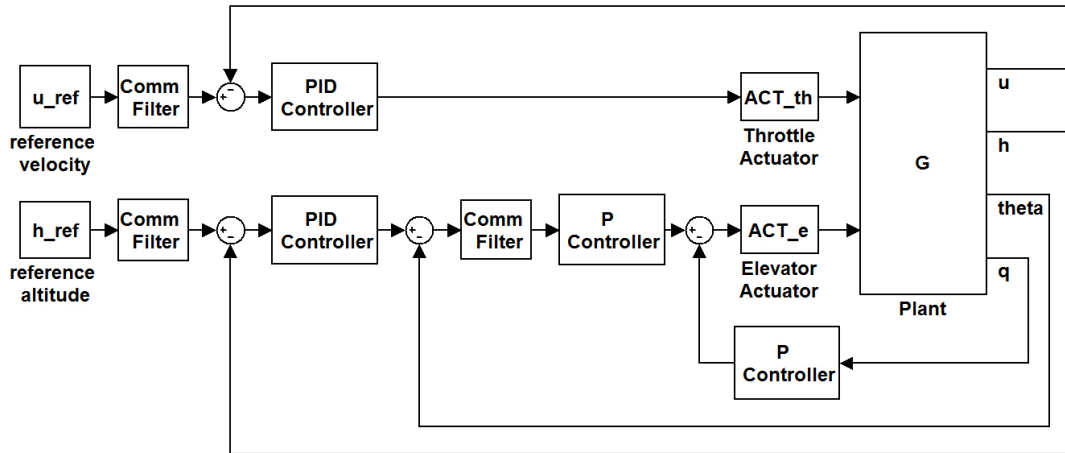


Figure 4.1: Block Diagram of the Longitudinal Controller

Table 4.1: Longitudinal Controller Gains

	$K_p$	$K_i$	$K_d$
u	300	200	25
h	0.1	0.025	0.15
$\theta$	1.5	0	0
q	2	0	0

A pitch rate stability augmentation system (SAS) is used in the most inner loop in order to enhance the control characteristics of the short period mode. Since the pitch rate SAS does not affect the phugoid mode characteristics, next a pitch attitude controller is designed to suppress the phugoid motion.

The outer loop receives the required altitude and velocity, and uses PID controllers to minimize the respective error signals. The integral term is used to eliminate the steady state errors whereas the derivative term is implemented to improve the transient performance characteristics. The system commands a pitch angle that is proportional to the height error. The reason is if there is an initial error in altitude, in order to fix it, the flight path must be deflected upward which means the angle of attack must be increased. Since short-term changes in pitch angle have a strong effect on angle of attack changes, pitch angle is used instead of angle of attack [17].

#### 4.1.5 Lateral Autopilot

The lateral autopilot generates the necessary aileron and rudder deflections from the roll angle and yaw rate errors, and sends these control signals to the actuators. First order command filters are implemented to the outer loops as shown in Figure 4.2. A roll rate damper is used to improve the steady state and transient performance characteristics of the aircraft. Roll angle and yaw rate errors are corrected via PI controllers as no derivative term is needed. Gains of the lateral controller are shown in Table 4.2.

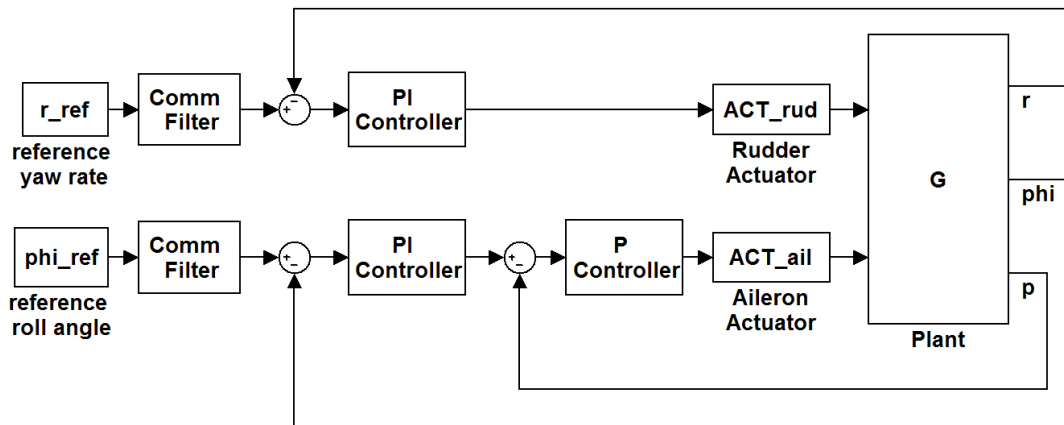


Figure 4.2: Block Diagram of the Lateral Controller

Table 4.2: Lateral Controller Gains

	$K_p$	$K_i$	$K_d$
r	-0.75	-0.05	0
$\phi$	0.95	0.5	0
p	10	0	0

#### 4.1.6 Robustness Analysis of the Classical Controllers

After determining the gains, robustness of the controllers are tested by analyzing the gain and phase margins of the loop gain of each channel. Sufficient information about the stability of the system can be obtained by considering both margins together and adequate performance can be maintained if the gain margin is greater than 6 dB and the phase margin is between 30-60° [37]. Bode plots for different loops are presented in Figures 4.3, 4.4 and 4.5. As may be observed from these results, both gain and phase margins are positive as desired which implies that the controllers in different channels are able to ensure the stability of the system.

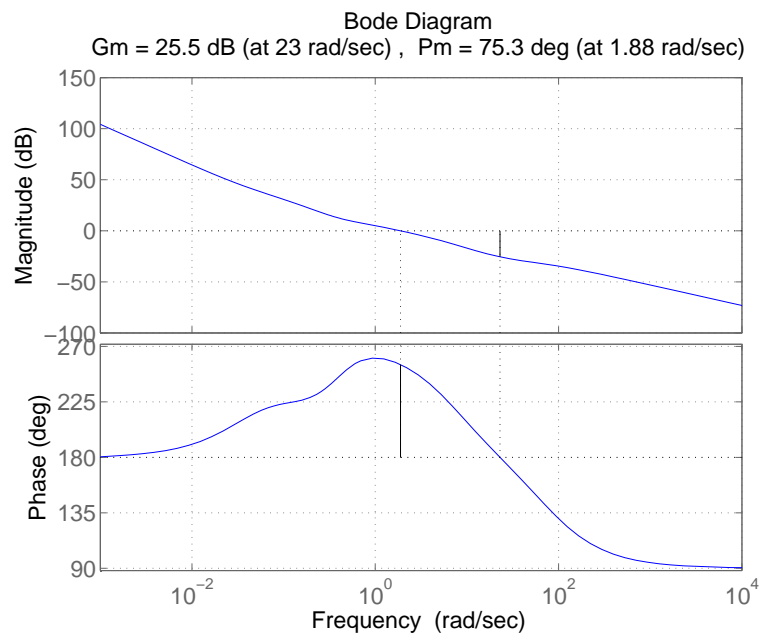


Figure 4.3: Bode Diagram of Altitude Channel

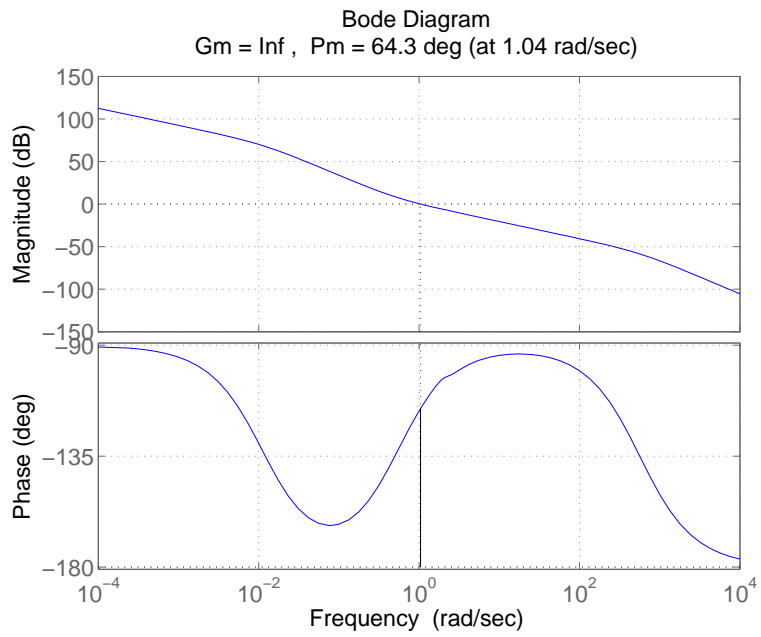


Figure 4.4: Bode Diagram of Roll Attitude Channel

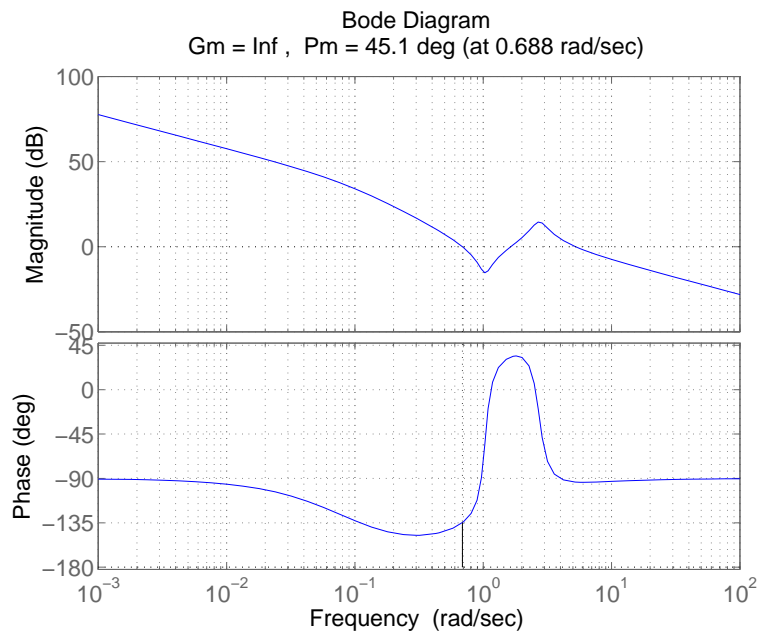


Figure 4.5: Bode Diagram of Yaw Rate Channel

## 4.2 Robust Controller Design

For flight control system designs, as mentioned previously in Section 4.1, generally classical sequential loop closing method based on SISO techniques is used. However, as more loops are added, the design procedure may become more difficult [45]. In addition, when the aircraft model contains some uncertainty, classical control methods may not work properly. Usually, a nominal model which represents the low-middle frequency range behavior of the plant is available, whereas the high frequency plant behavior is uncertain. These lead to a need for a robust controller that satisfies robust performance as well as the nominal performance by taking the uncertainties into consideration [10, 38].

Robust controllers can be designed by  $H_\infty$  optimization. The objective of  $H_\infty$  optimization is to design a controller that minimizes the  $H_\infty$  norm of the closed loop system. However, since the structure of the uncertainties is not taken into account, the controller may be unable to satisfy the performance measures. Therefore, in the thesis, the complex  $\mu$ -synthesis is also applied to take the structured uncertainties into consideration and obtain a controller which achieves robust performance as well as robust stability.

### 4.2.1 Problem Statement

The problem of controlling uncertain systems is also referred as the 'robust control problem'. In the thesis, the control problem is posed as a robust performance, model matching problem with multiplicative plant uncertainty at the plant input and minimization of weighted output transfer functions as the performance criterion. This control problem is shown in Figure 4.6 in the generalized plant form.

$P$  represents the generalized plant model to be controlled. It is a finite dimensional linear time invariant (FDLTI) system and derived from the nominal plant model. It includes design parameters and design weighting functions.  $K$  is the MIMO controller which simultaneously guarantees the stability of the aircraft when the system deviates from its nominal design condition or subjected to significant disturbances. In addition, it satisfies the performance specifications for all of the perturbed plants about the nominal model up to the worst case uncertainty by minimizing the norm of the transfer function from external inputs to the error signals [43].

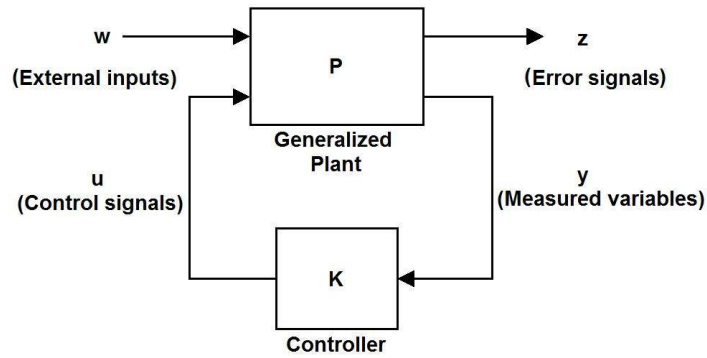


Figure 4.6: General Design Framework

### 4.2.2 Norms of Systems

There are many ways to determine the size of a signal or a system for stability and performance measures. Norms are one of the most common methods used to quantify the size of a signal or a system by describing certain geometric properties. A real-valued function  $\|x\|$  represents the norm of  $x$  and satisfies the following relations [43]:

Non-negativity :  $\|x\| \geq 0$

Positive definiteness :  $\|x\| = 0 \Leftrightarrow x = 0$

Homogeneity :  $\|\alpha \cdot x\| = |\alpha| \cdot \|x\|$  for any scalar  $\alpha$

Triangle inequality :  $\|x + y\| \leq \|x\| + \|y\| \forall x$  and  $y \in V$ ,  $V$  being a vector space.

The block diagram of an LTI system is illustrated in Figure 4.7 where  $u(t)$  and  $y(t)$  exist for  $t \geq 0$ .

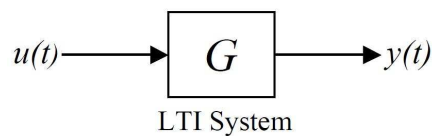


Figure 4.7: Block Diagram of an LTI System

Following norms can be defined for scalar signals:

$$L_1 \text{ norm: } \|u\|_{L_1} \triangleq \int_0^{\infty} |u(t)| dt \quad (4.4)$$

$$L_2 \text{ norm: } \|u\|_{L_2} \triangleq \left[ \int_0^{\infty} |u(t)|^2 dt \right]^{1/2} \quad (4.5)$$

$$L_p \text{ norm: } \|u\|_{L_p} \triangleq \left[ \int_0^{\infty} |u(t)|^p dt \right]^{1/p} \quad p \geq 1 \quad (4.6)$$

$$L_{\infty} \text{ norm: } \|u\|_{L_{\infty}} \triangleq \sup_{t \in [0, \infty)} |u(t)| \quad (4.7)$$

Root mean square (RMS) is another important measure for signals. It reflects the eventual average size of a signal (Equation 4.8). Persisting signals, such as unit step and sinusoidals, are not in  $L_p$  (function space based on  $L_p$  norm); however, they have finite RMS values.

$$\|u\|_{RMS} \triangleq \sqrt{\lim_{T \rightarrow \infty} \frac{1}{T} \int_0^{\infty} |u(t)|^2 dt} \quad (4.8)$$

Usually, norms of systems are determined in terms of the norms of input and output signals (induced norms). Considering the system shown in Figure 4.7, the RMS of the output can be defined as:

$$\|y\|_{RMS} = \sqrt{\frac{1}{2\pi} \int_{-\infty}^{\infty} |G(j\omega)|^2 S_u(\omega) d\omega} \quad (4.9)$$

where  $S_u(\omega)$  is the power spectral density of the input.

When the input is a white noise with unit sensitivity ( $S_u(\omega)=1$ ), the RMS of the output is defined as the  $H_2$  norm of the system  $G$  (Equation 4.10). Hence,  $H_2$  norm of a transfer function measures the RMS response of its output when it is driven by a white noise input.

$$\|G\|_2 \triangleq \sqrt{\frac{1}{2\pi} \int_{-\infty}^{\infty} |G(j\omega)|^2 d\omega} \quad (4.10)$$

In the thesis,  $H_{\infty}$  norm (RMS gain or energy gain) is used for robustness studies. For a stable SISO system, it can be expressed as its maximum magnitude on the  $j\omega$  axis (Equation 4.11).  $H_{\infty}$  norm is the peak value in Bode magnitude plot of the system and it provides a bound on the system gain.

$$\|G\|_{RMS-gain} = \sup_{\|u\|_2 \neq 0} \frac{\|G u\|_2}{\|u\|_2} = \sup_w |G(j\omega)| \quad (4.11)$$

For a stable MIMO system,  $H_\infty$  norm can be expressed as the peak value of the largest singular value ( $\bar{\sigma}$ ) of the frequency response matrix ( $G(j\omega)$ ) over the whole frequency range:

$$\|G\|_{RMS-gain} = \|G\|_\infty = \sup_{\omega} \bar{\sigma}(G(j\omega)) \quad (4.12)$$

### 4.2.3 Linear Fractional Transformations (LFTs)

LFTs were introduced by Doyle [12] into the control literature. They provide a powerful and flexible approach to represent uncertainty in matrices and systems [6].

The general design framework of the control problem is called the 'linear fractional transformation'. The plant  $P = \begin{bmatrix} A & B \\ C & D \end{bmatrix}$  can be partitioned in the form of equation 4.13.

$$P \triangleq \begin{bmatrix} P_{11} & P_{12} \\ P_{21} & P_{22} \end{bmatrix} \quad (4.13)$$

Then,

$$\begin{bmatrix} z \\ y \end{bmatrix} = \begin{bmatrix} P_{11} & P_{12} \\ P_{21} & P_{22} \end{bmatrix} \begin{bmatrix} w \\ u \end{bmatrix} \quad (4.14)$$

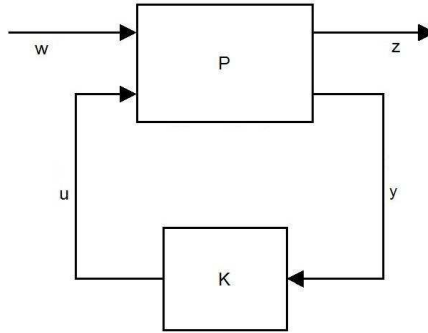


Figure 4.8: Lower Linear Fractional Transformation

The system is shown in Figure 4.8. In this figure,  $K$  represents the controller. Using  $u = Ky$ ,  $u$  and  $y$  can be eliminated, and the transfer function resulting from positive feedback of  $K$  around the lower part of  $P$  can be obtained. This is called the lower linear fractional transformation of  $P$  with  $K$  and can be represented as given in equation 4.15.

$$F_l(P, K) = P_{11} + P_{12}K(I - P_{22}K)^{-1}P_{21} \quad (4.15)$$

Similarly, upper linear fractional transformation of  $P$  with  $\Delta$  can be obtained by considering the  $P$ - $\Delta$  configuration shown in Figure 4.9. The transfer function (Equation 4.16) is obtained by the positive feedback of  $\Delta$  around the upper part of  $P$ .

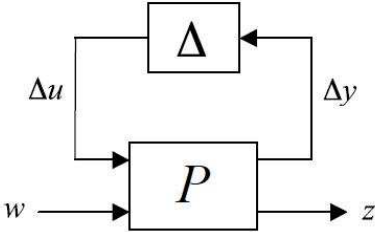


Figure 4.9: Upper Linear Fractional Transformation

$$F_u(P, \Delta) = P_{22} + P_{21}K(I - P_{11})^{-1}P_{12} \tag{4.16}$$

**4.2.4 Closed Loop Transfer Functions**

The closed loop system which includes the feedback structure of the plant  $P$  and controller  $K$  is depicted in Figure 4.10. In this diagram,  $r$  is the reference signal,  $u$  is the control signal,  $n$  is the measurement noise, and  $d$  is the disturbance.

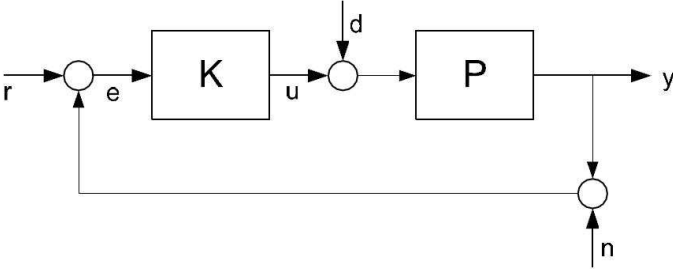


Figure 4.10: Feedback Configuration

Transfer function of such a system can be defined as in equation 4.17.

$$y = P[K(r - y - n) + d] \tag{4.17}$$

With some manipulations, the following equation can be found:

$$y = \underbrace{(I + PK)^{-1}PK}_{T} r + \underbrace{(I + PK)^{-1}P}_{S} d - \underbrace{(I + PK)^{-1}PK}_{T} n \quad \text{where } S + T = 1 \quad (4.18)$$

In equation 4.18,  $S$  and  $T$  are the sensitivity and complementary sensitivity functions, respectively. As the name implies,  $S$  is the transfer function that characterizes the sensitivity of the outputs to disturbances. In addition,  $T$  is the transfer function from the command inputs to the outputs.

For good tracking ( $y \approx r$ ),  $T$  has to be large, whereas for satisfactory sensor noise rejection  $T$  has to be small at the frequencies where large noises are present. On the other hand, to ensure small tracking errors (good disturbance rejection),  $S$  has to be small at the frequencies where the reference inputs and disturbances are large. However, since  $S+T=1$ , it is clear that  $S$  and  $T$  cannot be small at any one frequency. Despite these contradictions, it is possible to ensure good tracking, good disturbance rejection and noise attenuation at the same time by making  $T$  large at low frequencies, where references and disturbances dominate and noises have little effect. By this way,  $S$  becomes small and good disturbance rejection is obtained. In addition, noise attenuation is ensured by making  $T$  small at high frequencies where noises are large. These rules explain the reason why a large loop gain ( $L = PK$ ) is required at low frequencies for good tracking and small errors, and a small loop gain is required at high frequencies for noise attenuation and small control signals (to avoid actuator saturation) [57].

#### 4.2.5 Model Uncertainty

The robustness of a control system can be defined as not being sensitive to differences between the actual system and the plant model which was used to design the controller. The term ‘uncertainty’, which refers to the difference between the actual system and the model, has great importance in  $H_\infty$  optimization. To analyze the worst-case uncertainty, first the uncertainty set should be defined; next the robust stability and performance conditions should be checked.

To account for model uncertainty, it is assumed that the dynamic behavior of the plant is described by a set of possible LTI models instead of a single LTI model. For this purpose, following notations are used in the thesis:

$\Pi$ : set of possible perturbed plant models (the uncertainty set)

$G(s) \in \Pi$ : nominal plant model (no uncertainty)

$G_p(s) \in \Pi$ : particular perturbed plant

$\Delta$  : perturbations represented by any stable transfer function with  $H_\infty$  norm less than 1.

There are many sources of model uncertainty and these are well defined in Ref [43]. These sources may be divided into two groups as parametric uncertainty and unmodeled dynamics uncertainty. In the following sections, these norm-bounded uncertainties are explained.

#### **4.2.5.1 Parametric Uncertainty**

In this kind of uncertainty, the structure of the plant (including the order) is known, but some of the parameters are uncertain. The uncertainty structure can be obtained from the mathematical model since  $G_p(s)$  and  $G(s)$  have the same structures. However, this type of uncertainty is usually avoided due to its disadvantages. It requires a large effort to model parametric uncertainty for especially complicated plant models. The exact model structure is needed, which means that the unmodeled dynamics cannot be dealt with. In addition, real perturbations are required although these are mathematically and numerically more difficult to deal with.

#### **4.2.5.2 Unmodeled Dynamics Uncertainty**

Construction of a mathematical model which includes the real physical system is never possible. The plant model cannot respond exactly the same as the actual plant and if the differences between these two are not considered, an effective robust controller cannot be designed.

As mentioned earlier in this section, a low order nominal model which represents the low-middle frequency plant behavior is usually available; whereas the plant behavior is uncertain at high frequencies. In this case, using parametric uncertainty may not be enough and a richer description may be needed. Additive and multiplicative uncertainties are used for this purpose, to account both the uncertain parameters and the higher order dynamics that are missing in the model Ref [43]. By this way, a frequency-dependent percentage uncertainty in the actual plant behavior can be specified.

For multiplicative uncertainty, the set of possible perturbed plant models can be described as:

$$\Pi : \{G_p(s) = G(s)(1 + W_m(s)\Delta(s)); \quad |\Delta(j\omega)| \leq 1 \quad \forall \omega\} \quad (4.19)$$

In equation 4.19, the uncertainties between the nominal plant model and the actual plant is represented by  $W_m$  and  $\Delta$ .  $W_m$  is the multiplicative uncertainty weighting function which defines the magnitude of the uncertainty resulting from the uncertain parameters and neglected dynamics at each frequency. As  $W_m$ ,  $\Delta$  is also assumed to be stable; however, it is unknown and bounded by the norm condition  $\|\Delta\|_\infty \leq 1$ . The structure of the multiplicative uncertainty is given in Figure 4.11.

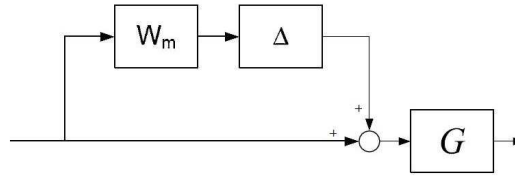


Figure 4.11: Multiplicative Uncertainty

From the definition, the multiplicative uncertainty can also be described as the following:

$$\max_{G_p \in \Pi} \left| \frac{G_p(j\omega) - G(j\omega)}{G(j\omega)} \right| \leq |W_m(j\omega)| \quad \forall \omega \quad (4.20)$$

As can be seen from equation 4.20,  $|W_m(j\omega)|$  is the maximum percentage difference between all of the possible perturbed plants and the nominal plant model at each frequency. On a Nyquist plot, a disk of radius  $|W_m(j\omega)G(j\omega)|$ , centered at  $G(j\omega)$  represents the set of possible values according to the uncertainty description.

The uncertainty can also be represented by the additive uncertainty in the form of equation 4.21.

$$\Pi : \{G_p(s) = G(s) + W_A(s)\Delta(s); \quad |\Delta(j\omega)| \leq 1 \quad \forall \omega\} \quad (4.21)$$

Block diagram for representing the uncertainty in additive form is given in Figure 4.12.

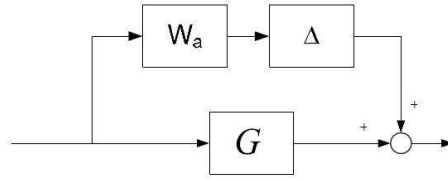


Figure 4.12: Additive Uncertainty

In the thesis, the multiplicative form is chosen for convenience. This is because it allows the spontaneous analysis of uncertainty magnitudes in terms of percent errors relative to the design model. Since the amount of deviation in the aerodynamic derivatives from their nominal values is known, this type of uncertainty is a good choice in order to model the uncertainties especially at high frequencies. Alternatively, additive uncertainty could have been used. In this type of uncertainty, the structured singular values are not complex numbers which would result in less conservative  $\mu$ -analysis. By this way, better robust performance as well as robust stability could have been achieved. However, as the largest singular values of the block diagonal matrices are around 1, using additive uncertainty form is not necessary and it is left as a future work. Choice of  $W_m$  for the longitudinal and lateral controllers will be explained in Section 4.2.11.2 and 4.2.12.2, respectively.

#### 4.2.6 Stability and Performance Requirements for SISO Systems

In this section, the stability and performance requirements of SISO systems are explained and the Small Gain Theorem is introduced. The structure of the system is shown in Figure 4.13. In this block diagram,  $W_p$  represents the stable transfer function of a pre-filter that is used to shape the reference signal  $r_p$  and  $W$  represents the uncertainty weighting function. More details about the system and the requirements can be found in Ref [13] and [43].

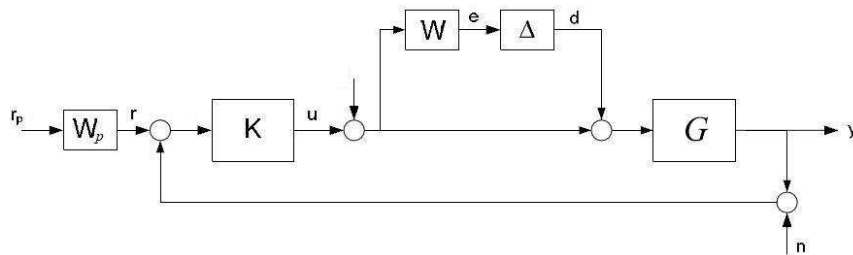


Figure 4.13: System Structure for Stability and Performance Criteria

#### 4.2.6.1 Nominal Stability (NS)

NS means that the system is stable with no model uncertainty. The closed loop transfer function ( $T$ ) should have internal stability which means that all of its poles are located in LHP and no unstable pole-zero cancellation exists. Loosing internal stability is an undesired situation due to the cancellation of those dangerous points with each other. To prevent this, there are some constraints on  $S$  and  $T$ , details of which are present in Ref [43] and [57].

#### 4.2.6.2 Nominal Performance (NP)

NP implies that the system has NS and satisfies the performance specifications with no model uncertainty. To achieve the desired performance, norm of the transfer function from disturbances to errors ( $S$ ) should be small. In terms of  $H_\infty$  norm, the condition can be written as:

$$\|W_p S\|_\infty \leq 1 \quad (4.22)$$

In equation 4.22,  $W_p$  represents the content of the disturbance and is used to shape the sensitivity function ( $S$ ) especially at low frequencies where the errors should be lessened.

#### 4.2.6.3 Robust Stability (RS)

RS refers to the stability of the closed loop system for all perturbed plants about the nominal model upto the worst-case uncertainty. If the  $H_\infty$  norm is used, the condition for RS can be stated as shown in equation 4.23.

$$\|WT\|_\infty \leq 1 \quad \forall \|\Delta\|_\infty \leq 1 \quad (4.23)$$

Nyquist stability criteria states that RS condition can be satisfied if and only if the loop transfer function does not encircle the -1 point. A related theorem is the 'Small Gain Theorem': if a feedback loop consists of stable systems and the loop gain product is less than unity, then the feedback loop is internally stable. This can be obtained by considering the  $M\Delta$  structure. By isolating the  $\Delta$  block and re-drawing the feedback connection, the following block diagram is obtained.

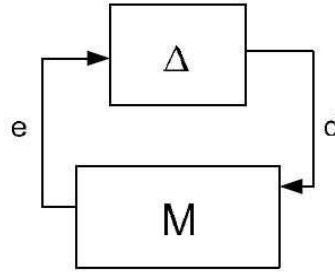


Figure 4.14:  $M\Delta$  Structure for Small Gain Theorem

In Figure 4.14,  $M$  represents the transfer function from the output of  $\Delta$  to the input of  $\Delta$ . It is called as the 'loop gain' and can be described as:

$$M = TF_{d \rightarrow e} = \frac{WKG}{1 + KG} = WT \quad (4.24)$$

Since  $M\Delta$  should not encircle the -1 point  $\forall \Delta$ :

$$|1 + M\Delta| > 0 \quad \forall \omega, \quad \forall |\Delta| \leq 1 \quad (4.25)$$

The worst case for the condition given in equation 4.25 is when  $\Delta = -1$ . Then, the RS condition can be written as:  $|M(j\omega)| < 1 \quad \forall \omega$ . More generally, plant  $M$  is said to be robustly stable to perturbations  $\Delta$  with  $\|\Delta\|_\infty \leq \gamma$  for some  $\gamma > 0$ , if and only if  $\|M\|_\infty = \|WT\|_\infty \leq 1/\gamma$ .

#### 4.2.6.4 Robust Performance (RP)

RP means that the NP condition is satisfied for all possible perturbed plants in the uncertainty set. All possible  $L_p(j\omega)$  should stay outside of a disk of radius  $|W_p(j\omega)|$  centered on -1 point.  $L_p(j\omega)$  at each frequency stays within a disk of radius  $|W(j\omega)L(j\omega)|$  centered on  $L(j\omega)$ . The condition for RP is that the two disks should not intersect:

$$|W_p| + |WL| < |1 + L| \quad \forall \omega \quad (4.26)$$

Then, the necessary and sufficient condition for RP can be obtained from equation 4.26 as the following:

$$\| |W_p S| + |WT| \|_\infty < 1 \quad (4.27)$$

Equation 4.27 implies that, for RP both NP and RS must be satisfied. For SISO systems, this may be achieved easily. However for MIMO systems, although NP and RS conditions are individually satisfied, the system may not have RP.

### 4.2.7 Stability and Performance Requirements for MIMO Systems

Stability and performance of MIMO systems can be analyzed by using a similar approach as for SISO systems. However, in this case, LFTs are needed due to the increased number of system inputs and outputs. As mentioned in Section 4.2.3, use of LFTs provides a powerful approach to represent the uncertainty in a system.

In general, both uncertainty and disturbances are present in the system. Considering this, the system can be constructed as shown in Figure 4.15 [43]. In this configuration,  $P$  represents the so called ‘generalized plant’ which includes the weights shown in Figure 4.13, and  $\Delta$  represents all possible uncertainties in the system.  $M$  is related to  $P$  and  $K$  by a lower LFT, such that  $M = F_l(P, K)$ . Then, the transfer function from disturbances ( $d$ ) to errors ( $e$ ) becomes  $e(s) = F_u(M, \Delta) d(s)$ , where  $F_u(M, \Delta)$  represents the upper LFT of  $M$  with  $\Delta$ .

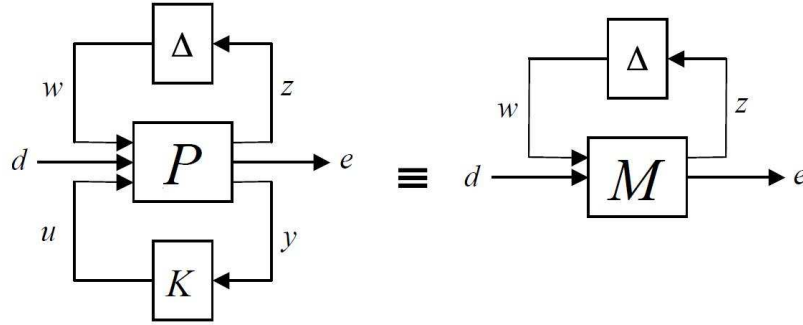


Figure 4.15: General Control Configuration using LFTs

#### 4.2.7.1 Nominal Stability (NS)

For NP, RS and RP, first NS must be satisfied. If a MIMO system has NS, it means that the whole system  $M$  is internally stable in the absence of uncertainties. In other words, transfer functions from all inputs to all outputs satisfy the NS condition for SISO case.

#### 4.2.7.2 Nominal Performance (NP)

NP is related to the transfer function from the disturbances to the errors. This condition can be satisfied by minimizing the  $H_\infty$  norm of this transfer function when the MIMO system has no model uncertainty, so that  $\|M_{22}\|_\infty < 1$ .

### 4.2.7.3 Robust Stability (RS)

Small Gain Theorem is used to derive the RS condition for a MIMO system. If  $\|\Delta\|_\infty \leq \gamma$ , then  $\|M_{11}\|_\infty \leq 1/\gamma$  is required for RS.

### 4.2.7.4 Robust Performance (RP)

RP requires the transfer function from disturbances to errors ( $TF_{d \rightarrow e}$ ) to be small even in the presence of  $\Delta$ . Hence, performance of a MIMO system can be checked by minimizing the  $H_\infty$  norm of the same transfer function. If  $\|F_u(F_l(P, K), \Delta)\|_\infty = \|F_u(M, \Delta)\|_\infty < 1$  for all  $\Delta$  with  $\|\Delta\|_\infty < 1$ , then the closed loop system has RP. By using the Small Gain Theorem, a sufficient condition can be obtained as  $\|M\|_\infty < 1$  [56]. More information about the RP of MIMO systems can be found in Section 4.2.9.

## 4.2.8 Solution of the $H_\infty$ Problem

The main objective of  $H_\infty$  optimization is to design a controller which lets the closed loop system to satisfy the stability and performance specifications in case of variations in the system parameters and errors in the plant model. As mentioned before, this can be achieved by minimizing the  $H_\infty$  norm of the transfer function from external inputs to the error signals. Considering Figure 4.6, this means that  $\|T_{wz}\|_\infty$  should be minimized over all finite-dimensional LTI stabilizing controllers  $K(s)$ , in order to get  $\|T_{wz}\|_\infty < 1$ . However, this is not as much easy as it seems. Since MIMO systems may experience much larger sensitivity to uncertainty than SISO systems, finding a unique optimal  $H_\infty$  controller may not be possible. Therefore, another definition of  $H_\infty$  control problem, named 'Sub-optimal Control Problem', is used: Given  $\gamma > 0$ , find all admissible controllers  $K$ , if exists, such that  $\|T_{wz}\|_\infty < \gamma$  [14]. The system of Figure 4.6 is described by equation 4.28 and a state space realization of the generalized plant  $P$  is given in equation 4.29.

$$\begin{bmatrix} z \\ y \end{bmatrix} = P(s) \begin{bmatrix} w \\ u \end{bmatrix} = \begin{bmatrix} P_{11}(s) & P_{12}(s) \\ P_{21}(s) & P_{22}(s) \end{bmatrix} \begin{bmatrix} w \\ u \end{bmatrix} \quad u = K(s) y \quad (4.28)$$

$$P = \left[ \begin{array}{c|cc} A & B_1 & B_2 \\ \hline C_1 & D_{11} & D_{12} \\ C_2 & D_{21} & D_{22} \end{array} \right] \quad (4.29)$$

D has a special off-diagonal structure.  $D_{11}$  is assumed to be 0 so that  $P_{11}(s)$  is strictly proper ( $P_{11}(j\omega) \rightarrow 0$  as  $\omega \rightarrow \infty$ ) and  $D_{22}$  is assumed to be 0 so that  $P_{22}(s)$  is also strictly proper ( $P_{22}(j\omega) \rightarrow 0$  as  $\omega \rightarrow \infty$ ). Then, the system equations can be written as the following:

$$\begin{aligned} \dot{x} &= Ax + B_1 w + B_2 u \\ z &= C_1 x + D_{12} u \\ y &= C_2 x + D_{21} w \end{aligned} \quad (4.30)$$

Theorem states that there exist a controller such that  $\|T_{zw}\|_\infty < \gamma$  if and only if the following three conditions hold [43]:

1. There exist a solution  $X_\infty > 0$  to

$$X_\infty A + A^* X_\infty + X_\infty \left( \frac{1}{\gamma^2} B_1 B_1^* - B_2 B_2^* \right) X_\infty + C_1^* C_1 = 0 \quad (4.31)$$

2. There exist a solution  $Y_\infty > 0$  to

$$A Y_\infty + Y_\infty A^* + Y_\infty \left( \frac{1}{\gamma^2} C_1^* C_1 - C_2^* C_2 \right) Y_\infty + B_1 B_1^* = 0 \quad (4.32)$$

3.  $\rho(X_\infty Y_\infty) < \gamma^2$

Equations 4.31 and 4.32 are the Algebraic Riccati Equations (AREs) that must be solved to find  $X_\infty$  and  $Y_\infty$ . The third condition represents the spectral radius. It implies that the largest eigenvalue of the multiplication  $X_\infty Y_\infty$  should be less than  $\gamma^2$ .

When these conditions are satisfied, the controller is given as:

$$K(s) = \left[ \begin{array}{cc} A_\infty & -Z_\infty L_\infty \\ F_\infty & 0 \end{array} \right] \quad (4.33)$$

where

$$A_\infty = A + \frac{1}{\gamma^2} B_1 B_1^* X_\infty + B_2 F_\infty + Z_\infty L_\infty C_2$$

$$F_\infty = -B_2^* X_\infty$$

$$L_\infty = -Y_\infty C_2^*$$

$$Z_\infty = \left( I - \frac{1}{\gamma^2} X_\infty Y_\infty \right)^{-1}$$

For the derivations of the results obtained from the theorem, the following assumptions should be made:

1.  $(A, B_2)$  is stabilizable and  $(A, C_2)$  is detectable (This assumption is necessary and sufficient for  $P$  to be internally stabilizable).

2.  $D_{12}^* [C_1 \ D_{12}] = [0 \ I]$

3.  $\begin{bmatrix} B_1 \\ D_{12} \end{bmatrix} D_{21}^* = \begin{bmatrix} 0 \\ I \end{bmatrix}$

#### 4.2.9 $\mu$ Analysis

##### 4.2.9.1 Structured Singular Value ( $\mu$ )

Robust stability and performance conditions for MIMO systems are discussed earlier in Section 4.2.7. These conditions are derived by using Small Gain Theorem and based on minimization of the  $H_\infty$  norm of the closed loop system. However, as mentioned at the beginning of Section 4.2, the structure of the uncertainties is not taken into account. Thus, a robust controller which satisfies the nominal performance and robust stability can be obtained; however, robust performance may still not be guaranteed. To solve this problem, the structured uncertainties are taken into consideration by using  $\mu$ -synthesis [11].

The uncertainty block  $\Delta$  in the  $M\Delta$  connection usually has a block-diagonal structure:

$\Delta = \text{diag}\{\Delta_i\}$ . This is illustrated in Figure 4.16.

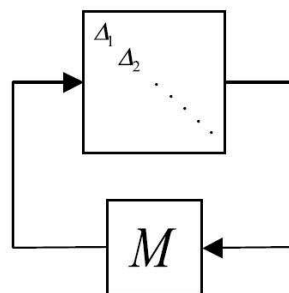


Figure 4.16:  $M\Delta$  Structure

The RS condition was previously defined as  $\bar{\sigma}(M(j\omega)) < 1$ . However, this is only the sufficient condition. By taking advantage of the fact that  $\Delta$  has a block-diagonal structure, a more effective definition can be obtained. By defining a scaling matrix  $D$  (Equation 4.34) and including it in the  $M\Delta$  structure, the modified  $M\Delta$  structure shown in Figure 4.17 can be constructed. In this figure,  $\Delta$  is a member of the set  $\Delta \in \mathbb{C}^{n \times n}$ .

$$D = \text{diag}\{d_i I_i\} \quad (4.34)$$

where  $d_i$  is a scalar and  $I_i$  is the identity matrix which has the same dimension as the  $i^{\text{th}}$  perturbation  $\Delta_i$ .

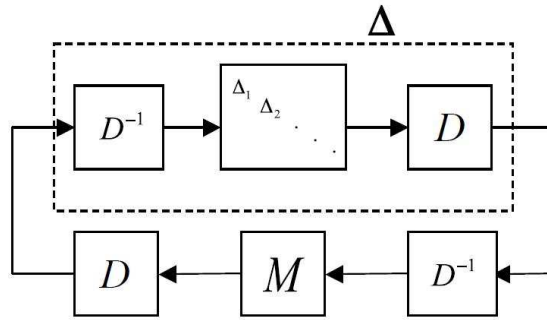


Figure 4.17: Modified  $M\Delta$  Structure

The overall system is the same since the scalings have no effect on stability. This means that the RS condition must also apply if  $M$  is replaced by  $DMD^{-1}$ :

$$\bar{\sigma}(DMD^{-1}) < 1, \quad \forall \omega \quad (4.35)$$

The least conservative RS condition can be obtained by minimizing the scaled singular value at each frequency. In equation 4.36,  $\mathbb{D}$  represents the set of block-diagonal matrices compatible with  $\Delta$  ( $\Delta D = D\Delta$ ). In addition, when  $\Delta$  is a full matrix,  $D = dI$ .

$$\min_{D(j\omega) \in \mathbb{D}} \bar{\sigma}(D(j\omega)M(j\omega)D(j\omega)^{-1}) < 1, \quad \forall \omega \quad (4.36)$$

As  $\bar{\sigma}(DMD^{-1}) = \bar{\sigma}(M)$ , when  $\Delta$  has a structure,  $\bar{\sigma}(DMD^{-1})$  may be smaller than  $\bar{\sigma}(M)$ . In fact, equation 4.35 is a scaled version of the Small Gain Theorem.

The structured singular value (SSV,  $\mu$ ) is an effective tool for deriving the necessary and sufficient conditions for RS and RP of a MIMO system with a given controller. It provides a generalization of the structured singular value  $\bar{\sigma}$  and can be described as the measure of the smallest structured  $\Delta$  that makes  $I - M\Delta$  singular. In mathematical form, it can be defined as given in equation 4.37. Note that  $\mu_\Delta(M)$  depends on both  $M$  and the structure of  $\Delta$ .

$$\mu_\Delta(M) \equiv \frac{1}{\min\{\bar{\sigma}(\Delta) : \det(I - M\Delta) = 0\}} \quad (4.37)$$

Since direct computation of  $\mu$  is not possible, the upper and lower bounds should be defined:

$$\rho(M) \leq \mu_\Delta(M) \leq \bar{\sigma}(M) \quad (4.38)$$

where  $\rho$  is the spectral radius and  $\bar{\sigma}$  is the maximum singular value.

The aim is to find the lowest  $\mu$  so that the best RS would be obtained. However, this may not be achieved because the gap between the bounds given in equation 4.38 may be arbitrarily large. The bounds can be tightened by using a scaling that will not affect  $\mu_\Delta(M)$  but will affect  $\rho$  and  $\bar{\sigma}$ . For this purpose, first the sub-sets of  $\mathbb{C}^{n \times n}$  should be defined:

$$\bar{Q} = \{Q \in \Delta : QQ^* = I_n\} \quad (4.39)$$

$$\bar{D} = \{diag[D_1, D_2, \dots, D_s, d_1 I_{m1}, d_2 I_{m2}, \dots, d_F I_{mF}] : D_i \in \mathbb{C}^{r_i \times r_i}, D_i = D_i^* > 0, d_j \in \mathbb{R}, d_j > 0\} \quad (4.40)$$

Then, the upper and lower bounds can be tightened to:

$$\max_{Q \in \bar{Q}} \rho(QM) \leq \mu_\Delta(M) \leq \inf_{D \in \bar{D}} \bar{\sigma}(DMD^{-1}) \quad \forall D \in \bar{D} \text{ and } Q \in \bar{Q} \quad (4.41)$$

### 4.2.9.2 Robust Stability (RS)

Assume that the nominal system  $M$  and the perturbation  $\Delta$  are stable. Then, the  $M - \Delta$  system is stable for all allowed perturbations if and only if equation 4.42 is satisfied.

$$\mu_{\Delta}(M(j\omega)) < 1 \quad (4.42)$$

### 4.2.9.3 Robust Performance (RP)

The general control configuration was previously discussed in Section 4.2.7. The interconnections between the uncertainty block  $\Delta$ , generalized plant  $P$  and the controller  $K$  are shown in Figure 4.15. Also in the same figure,  $M$  represents the plant when the  $H_{\infty}$  controller is connected.

From the definition of RP given in Section 4.2.7.4 ( $\|F_u(M, \Delta)\|_{\infty} < 1 \forall \|\Delta\|_{\infty} < 1$ ), RP condition can be turned into a RS condition by adding a fictitious performance block  $\Delta_p$ . The set of uncertain plants with and without  $\Delta_p$  block is shown in Figure 4.18.

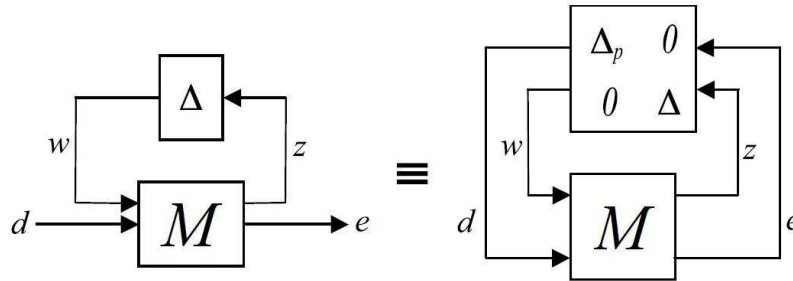


Figure 4.18: Set of Perturbed Plants

Then, this system has RP if and only if :

$$\mu_{\bar{\Delta}}(M(j\omega)) < 1 \quad \forall \omega \quad (4.43)$$

$$\text{where } \bar{\Delta} = \begin{bmatrix} \Delta_p & 0 \\ 0 & \Delta \end{bmatrix}$$

### 4.2.10 Implementation on MATLAB

Robust autopilots of the UAV are designed according to the Robust Control Theory discussed in the previous sections. During the design process, implementation of theory is achieved by using Robust Control Toolbox of Matlab<sup>®</sup>. Following sections explain the design process and tools used for this purpose.

#### 4.2.10.1 Controller Configuration

As mentioned in Section 4.2.1, the control problem is posed as a robust performance, model matching problem with multiplicative plant uncertainty at the plant input. The aim is to minimize the weighted output transfer functions of the closed-loop system and by this way to guarantee the design requirements in the presence of significant uncertainties and/or disturbances. A diagram for the closed loop MIMO system, which includes the feedback structure of the plant and controller, and elements associated with the uncertainty models and performance objectives, is shown in Figure 4.19.

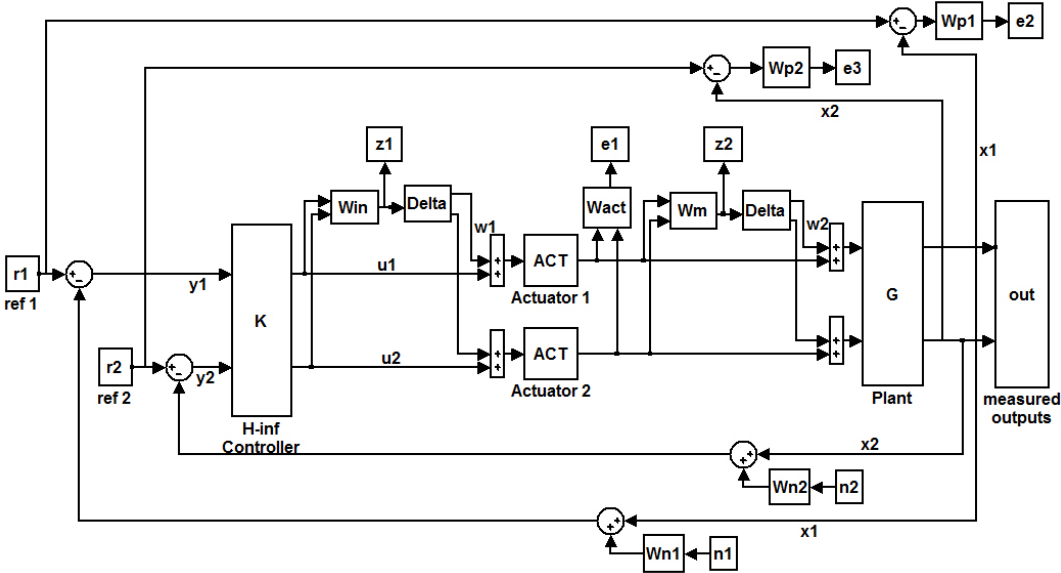


Figure 4.19: Block Diagram of the Closed-loop System

Figure 4.19 represents the control structure used for both longitudinal and lateral controller designs in the thesis. For the longitudinal autopilot, the reference inputs  $r_1$  and  $r_2$  are required velocity and pitch attitude; whereas for the lateral autopilot the reference inputs are roll angle

and yaw rate commands. In the diagram,  $u_1$  and  $u_2$  are the control inputs,  $x_1$  and  $x_2$  are the measured outputs,  $y_1$  and  $y_2$  are the deviations of the outputs from the required ones,  $n_1$  and  $n_2$  are the measurement noises in the respective channels.

In addition to multiplicative plant uncertainty at the plant input, uncertainty on the actuators is also taken into account. These uncertainties are bounded in size and described by the weighting functions  $W_m$  and  $W_{in}$ , respectively. In the diagram,  $z_1$  and  $z_2$  represent the errors related to these uncertainties. Moreover,  $e_1$ ,  $e_2$ , and  $e_3$  are the errors related to performance and used to create the fictitious  $\Delta_p$  block required for robust performance analyses.  $W_{act}$  is needed to shape the penalty on control signals in order to satisfy the control surface limits. On the other hand,  $W_{p1}$  and  $W_{p2}$  are utilized to achieve the performance objectives. In other words, to make the UAV respond effectively to the reference commands  $r_1$  and  $r_2$ . Finally, using  $W_{n1}$  and  $W_{n2}$ , effect of sensor noises are included in the model. Choice of these weighting functions are explained in Sections 4.2.11.2 and 4.2.12.2 in detail.

#### 4.2.10.2 Obtaining Controllers

The first step for designing a robust controller is to express the problem as in the form of Figure 4.15. After defining the uncertainty, performance and other weighting functions, the system is partitioned in terms of inputs, disturbances, errors and outputs, and transformed into LFT form. Implementation in the Matlab<sup>®</sup> environment is achieved by using ``sysic`` command. This command can be readily found in Matlab<sup>®</sup> Robust Control Toolbox and provides an easy solution for building the interconnection structure of certain and/or uncertain systems.

As explained in Section 4.2.8, synthesizing an  $H_\infty$  controller requires the solutions of AREs. Normally, these equations are solved by spectral decomposition of the Hamiltonian matrices and the sub-optimal controller  $K$  is found by applying a search procedure [20]. In Robust Control Toolbox, a useful command (``hinfsyn``) is present which can be used for this purpose. This command includes numerically reliable routines and can be used to obtain the optimal solution similar to that for the frequency domain approach.

In the thesis, after the generalized plant  $P$  is obtained by using ``sysic`` command, the optimal  $H_\infty$  controller for the LTI model is found by ``hinfsyn`` command. Then, state space form of the controller  $K$  is obtained by using ``ssdata`` command and all used in the simulations. Controllers are designed for the longitudinal and lateral linear dynamics separately, next combined together and validated through nonlinear simulations.

#### 4.2.10.3 $\mu$ Analysis

Robust performance tests are performed via  $\mu$  analysis. To obtain the set of perturbed plants as shown in Figure 4.18, first the controller  $K$  is embedded in the system and the closed loop  $M\Delta$  structure is formed by using ``sysic`` command. In addition, a fictitious  $\Delta_p$  block is added to take the structure of the uncertainties into account.

Considering the closed loop system given in Figure 4.19, the  $M\Delta$  structure (including  $\Delta_p$ ) is formed (Figure 4.20). Computation of the upper and lower bounds on the structured singular value ( $\mu_{\bar{\Delta}}$ ) is achieved by using ``mussv`` command. Robust performance of both the longitudinal and lateral controllers of the UAV are tested by using this command.

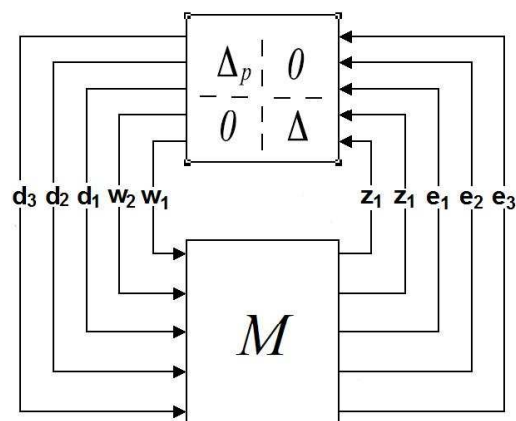


Figure 4.20: Block Diagram of the  $M\Delta$  Structure

### 4.2.11 Longitudinal Autopilot

#### 4.2.11.1 Controller Configuration

Longitudinal robust controller of the UAV is designed according to the structure shown in Figure 4.19. Considering this figure,  $r_1$  and  $r_2$  represent the reference velocity and pitch angle, and  $G$  represents the linearized longitudinal dynamics of the aircraft. The controller is used to find the elevator and throttle inputs to the aircraft and to control the velocity and pitch angle commands while attenuating disturbances and handling uncertainties in the dynamic model.

The overall longitudinal flight control system design is carried out by combining two design techniques. The inner loop consists of a robust controller where the inputs are the velocity and pitch attitude, and outputs are the elevator deflection and throttle. Control signals generated by the robust controller are finally sent to the elevator and throttle actuators. First this part is designed to establish some inherent inner loop stability and account for the disturbances as well as the model uncertainties. The outer loop controller is a classical PID controller which generates the necessary pitch attitude command that goes into the robust controller. The block diagram of the longitudinal autopilot developed in Simulink® is depicted in Figure 4.21 and the outer loop PID controller gains are given in Table 4.3.

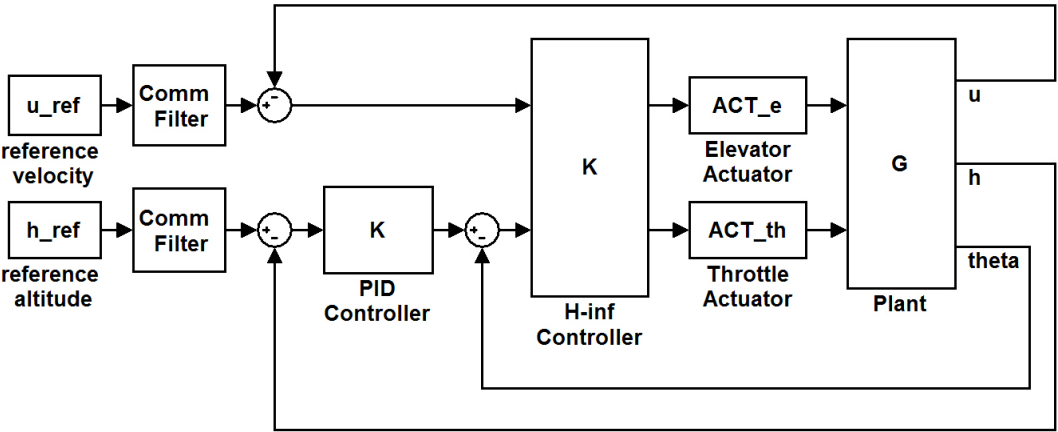


Figure 4.21: Block Diagram of the Longitudinal Autopilot

Table 4.3: PID Controller Gains for the Longitudinal Autopilot

	$K_p$	$K_i$	$K_d$
h	0.2	0.03	0.045

During the design phase, direct control of altitude and velocity is also tried. That is, pitch angle is not used in the inner loop and pure robust control techniques are applied. However, in this case it is seen that, commanded altitude cannot be maintained and the simulation blows up after a certain time. The reason for this can be explained by considering the following relation:

$$\Delta \dot{h} = -\Delta w + u_0 \sin(\Delta\theta) \approx -\Delta w + u_0 \Delta\theta \quad (4.44)$$

In equation 4.44, the climb rate ( $\dot{h}$ ) is represented in terms of the states. Note that in this equation, the pitch angle variation ( $\Delta\theta$ ) is assumed to be small. However, while trying to control the altitude directly, the pitch angle is free to take any value. Due to lack of control on the pitch attitude,  $\Delta\theta$  cannot be kept small and acquires large values spontaneously. For the linear model, as  $\Delta\theta$  gets higher values,  $\Delta \dot{h}$  increases, equation 4.44 fails, etc. On the other hand, for the nonlinear model, as  $\theta$  increases, angle of attack ( $\alpha$ ) also increases. This results in aircraft stall and control loss. Moreover, when nonlinearities are taken into consideration, realization of the desired altitude becomes even more difficult. This problem is solved by using a PID controller which generates the pitch attitude command from the altitude error and pitch attitude is controlled by the robust controller along with the velocity. As can be seen in Figure 4.21, first order command filters, which are low pass filters, are also used to match the performance of the aircraft to the commands.

#### 4.2.11.2 Choice of Weighting Functions

Determination of the weighting functions plays a crucial role in robust control system designs. In order to satisfy the design requirements in presence of significant uncertainties and disturbances, the weights discussed in Section 4.2.10.1, should be selected appropriately. Considering the closed loop structure of the control problem given in Figure 4.19,  $W_{act}$ ,  $W_n$ ,  $W_p$ ,  $W_{in}$  and  $W_m$  are related to the performance requirements, size of the uncertainties and external disturbances. Therefore, they should be considered as design constraints.

For the longitudinal robust controller,  $W_{act}$  is used to penalize the elevator and throttle inputs. Using this weight, the control activity is minimized by penalizing the large control deflections.  $W_{act}$  is selected as a 2x2 constant weighting function representing 1 % error on the actuator outputs (Equation 4.45).

$$W_{act} = \begin{bmatrix} 0.01 & 0 \\ 0 & 0.01 \end{bmatrix} \quad (4.45)$$

$W_{n1}$  and  $W_{n2}$  are used to model the magnitude of the sensor noises in velocity and pitch angle channels, respectively. Since uncertainty on sensor measurement increases at high frequencies, usually these weights are selected as high-pass filters. However simulations showed that, constant weights also lead to satisfactory results in terms of noise attenuation. Therefore, these weights are not selected as frequency varying functions. Instead, they are taken as constant for all frequencies representing the effects of 1 % measurement noises in the corresponding channels.

$W_{p1}$  and  $W_{p2}$  are directly related to the performance requirements of the system.  $W_{p1}$  weights the difference between the idealized velocity response and the actual aircraft response, whereas  $W_{p2}$  weights the difference between the idealized pitch attitude response and the actual aircraft response. Using these weighting functions, the tracking errors can be thought of as penalty functions.

Frequency characteristics of the performance weights are illustrated in Figure 4.22. As it may be observed from these plots, both  $W_{p1}$  and  $W_{p2}$  are selected as low-pass filters. They have higher gains when small errors are desired (low frequency range) and smaller gains when larger errors can be tolerated (high frequency range).

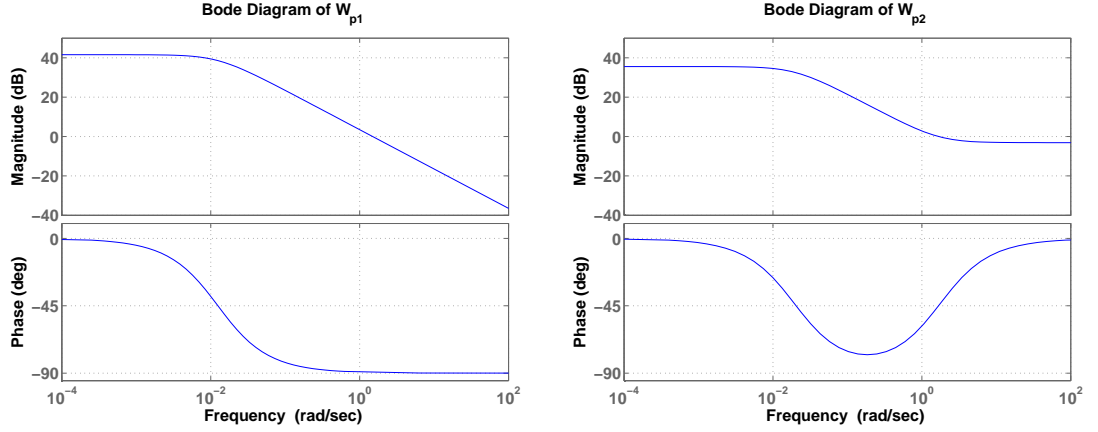


Figure 4.22: Bode Plots of  $W_{p1}$  and  $W_{p2}$

$W_{in}$  represents the uncertainty in the frequency responses of the actuators. Assuming that there is 5 % uncertainty on the actuators across all frequencies,  $W_{in}$  is taken as a 2x2 constant diagonal matrix (Equation 4.46).

$$W_{in} = \begin{bmatrix} 0.05 & 0 \\ 0 & 0.05 \end{bmatrix} \quad (4.46)$$

In general, flight control systems are reliable at low frequencies. However, as the frequency increases, due to uncertainties in system parameters and/or neglected dynamics, reliability may be lost.  $W_m$  is the multiplicative uncertainty weight used to model these errors in an unstructured form at the plant input [32]. Because multiplicative perturbations are small at low frequencies and they increase towards high frequencies, typically,  $W_m$  is an increasing weighting function with frequency.

In the thesis, it is assumed that the main source of the uncertainties is the variations in the aerodynamic database. For the longitudinal dynamics, the most important aerodynamic derivatives are longitudinal static stability derivative  $C_{m_\alpha}$ , pitch damping derivative  $C_{m_q}$  and elevator control effectiveness  $C_{m_{\delta_e}}$ . In order to find the weighting function  $W_m$ , 5 % uncertainty for the most important aerodynamic derivatives has been added to their nominal values and their effects on the components of the longitudinal state and input matrices are computed. Then, corresponding components of these matrices are changed while designing the controllers.

The uncertainty weight  $W_m$  is of the following form:

$$W_m = \begin{bmatrix} W_{m1} & 0 \\ 0 & W_{m2} \end{bmatrix} \quad (4.47)$$

where the weight  $W_{m1}$  is associated with the elevator input and  $W_{m2}$  with the thrust input.

The weighting function  $W_m$  can be obtained by finding the upper bounds on Bode plots of possible perturbations in the uncertainty set. For this purpose, first the transfer function of the particular plant  $G_p$  (Equation 4.19) and then, the difference between the particular and nominal plants are found (Equation 4.20). The perturbed and nominal plants from elevator and throttle to  $u$ ,  $w$ ,  $q$  and  $\theta$  are considered and the relative errors are plotted. The corresponding relative errors ( $|(G_p - G)/G|$ ) are shown as functions of frequency for all uncertainty cases. Results for elevator and throttle are shown in Figure 4.23 and 4.24, respectively. As can be seen,  $W_{m1}$  and  $W_{m2}$  lie above the error curves at each frequency.

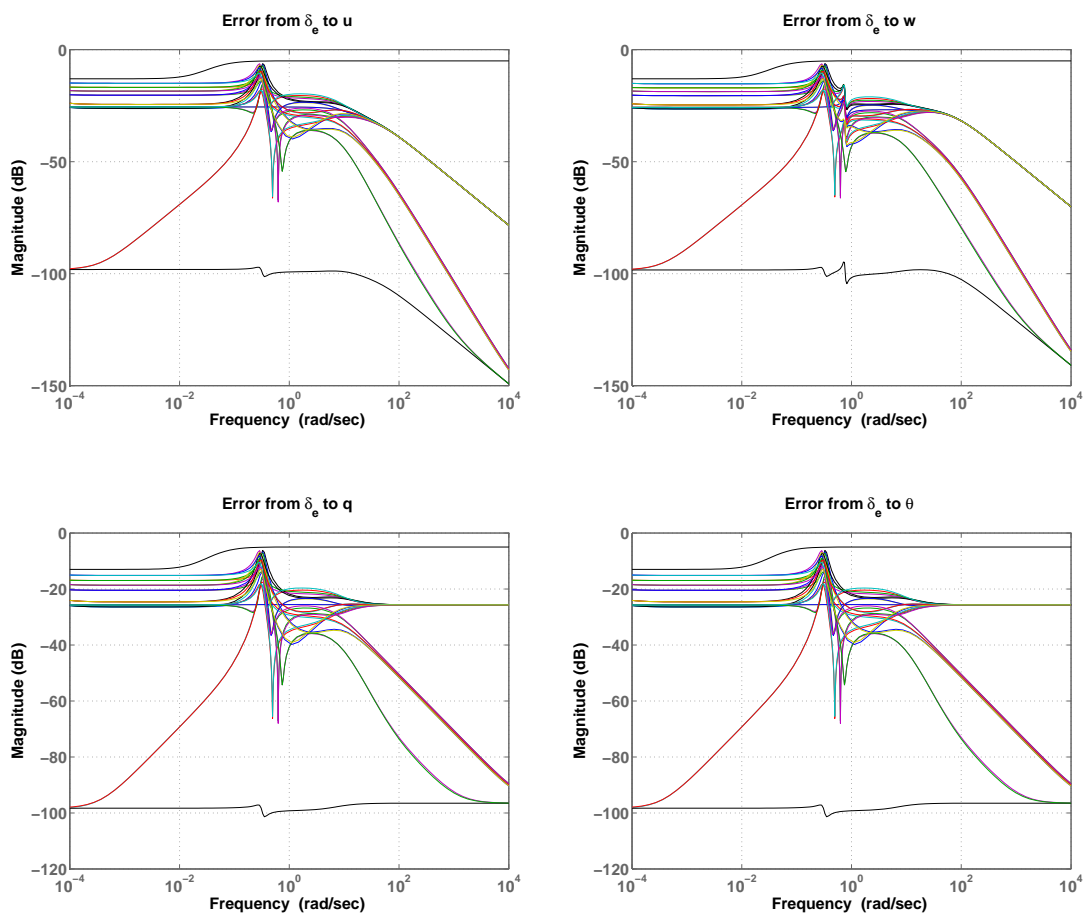


Figure 4.23: Relative Errors for Elevator Inputs

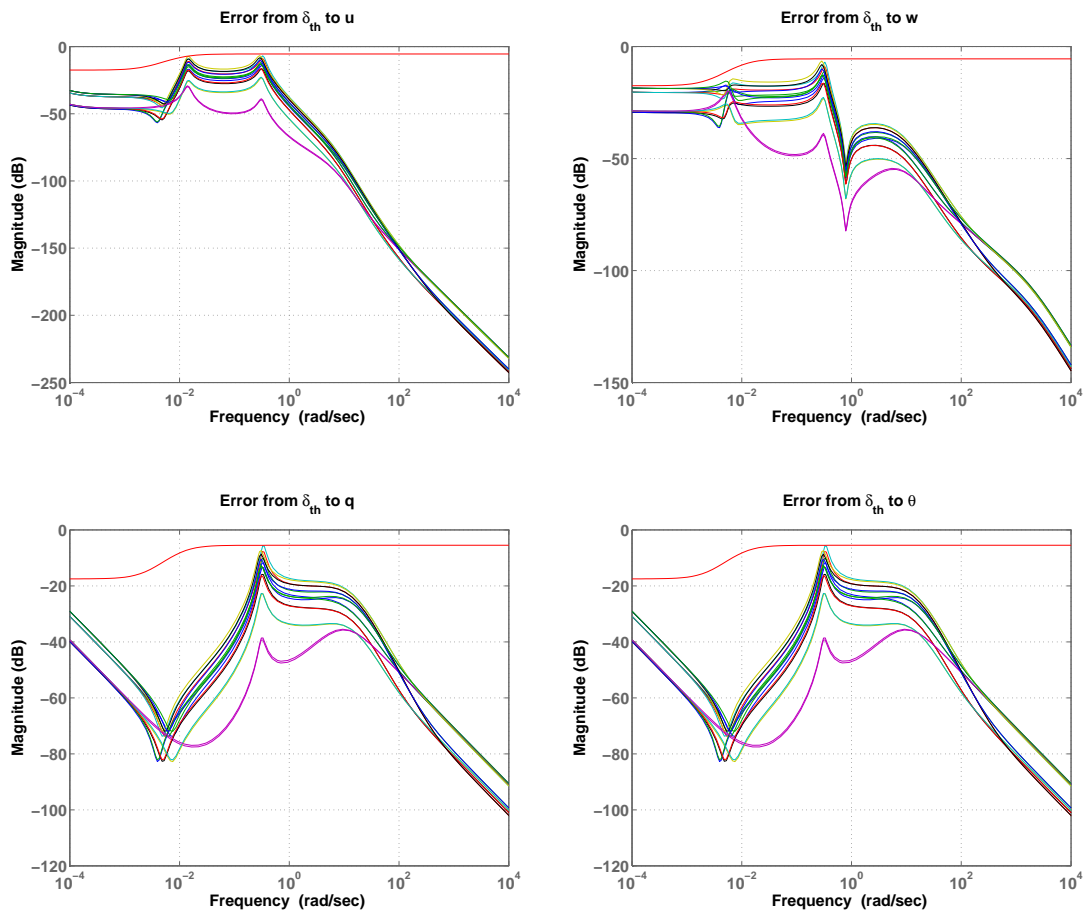


Figure 4.24: Relative Errors for Throttle Inputs

### 4.2.11.3 Robust Performance Analysis

Robust performance of the controller is checked by  $\mu$  analysis. The structured singular value,  $\mu_{\bar{\Delta}}(M(j\omega))$ , is computed at each frequency with

$$\bar{\Delta} = \begin{bmatrix} \Delta_p & 0 \\ 0 & \Delta \end{bmatrix}, \quad \Delta_p \in \mathbb{C}^{4 \times 4}, \Delta = \text{diag}\{\Delta_1, \Delta_2\}, \Delta_1 \in \mathbb{C}^{2 \times 2}, \Delta_2 \in \mathbb{C}^{2 \times 2} \quad (4.48)$$

The  $\mu$  curve for the controller is shown in Figure 4.25. The peak value is the largest singular value of the block diagonal matrix for the worst case. Since it is 0.89, it is proved that the robust performance condition ( $\mu_{\bar{\Delta}}(M(j\omega)) < 1$ ) is satisfied.

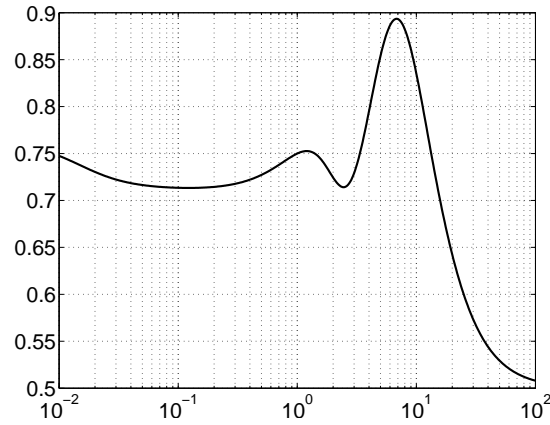


Figure 4.25:  $\mu$  Curve for Robust Performance of the Longitudinal Controller

## 4.2.12 Lateral Autopilot

### 4.2.12.1 Controller Configuration

Lateral robust controller of the UAV is designed by considering the structure shown in Figure 4.19. The controller takes the roll angle and yaw rate errors, and outputs the control signals to the aileron and rudder actuators. It tries to stabilize the aircraft and satisfy the performance specifications for all of the perturbed plants about the nominal model up to the worst case uncertainty. The block diagram of the lateral autopilot developed in Simulink<sup>®</sup> is shown in Figure 4.26.

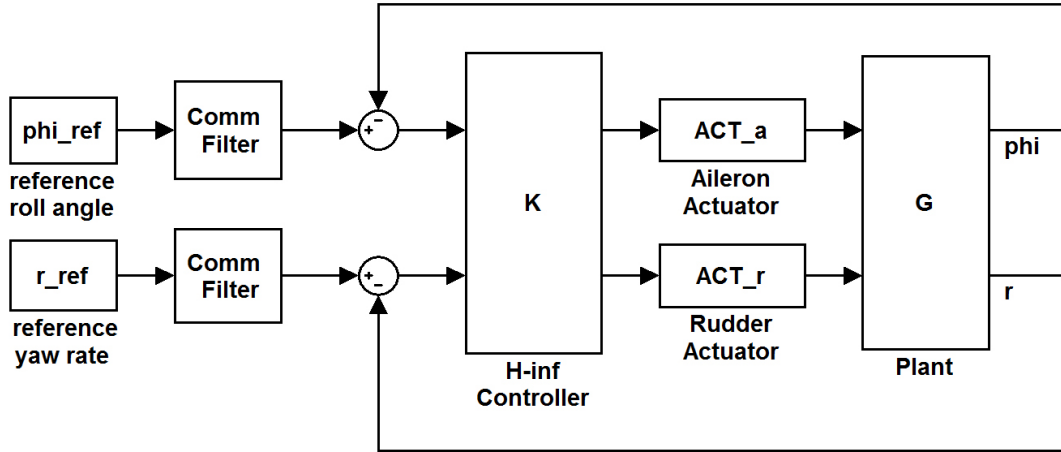


Figure 4.26: Block Diagram of the Lateral Autopilot

#### 4.2.12.2 Choice of Weighting Functions

Weighting functions for the lateral controller are determined by a similar approach as done for the longitudinal controller.

$W_{act}$  is used to shape the penalty on the aileron and rudder inputs, and to satisfy the actuator limits. It is selected as a  $2 \times 2$  constant weighting function representing 1 % error on the actuator outputs (Equation 4.49).

$$W_{act} = \begin{bmatrix} 0.01 & 0 \\ 0 & 0.01 \end{bmatrix} \quad (4.49)$$

Assuming 1 % sensor noise across all frequencies,  $W_{n1}$  and  $W_{n2}$  are taken as constants.

As mentioned before,  $W_{p1}$  and  $W_{p2}$  are the performance weights.  $W_{p1}$  weights the difference between the idealized roll attitude response and the actual aircraft response, whereas  $W_{p2}$  weights the difference between the idealized yaw rate response and the actual aircraft response. They are used to obtain a good performance tradeoff in the design and are both selected as low-pass filters since more performance is desired at low frequencies. Bode plots of the performance weights are given in Figure 4.27.

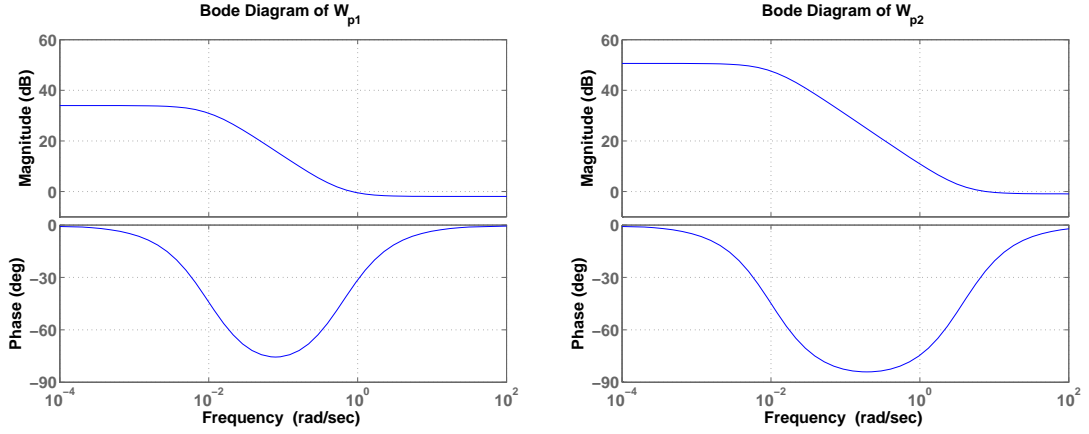


Figure 4.27: Bode Plots of  $W_{p1}$  and  $W_{p2}$

$W_{in}$  is taken as the same with the one used for the longitudinal controller. It is selected as a 2x2 constant diagonal matrix and represents the effect of 5 % on the actuators across all frequencies.

Multiplicative uncertainty weight  $W_m$  is determined by adding 5 % uncertainty to the most important aerodynamic derivatives. For the lateral dynamics, these are effective dihedral  $C_{l\beta}$ , roll damping derivative  $C_{lp}$  and aileron control effectiveness  $C_{l\delta_a}$ . To account for the 5 % uncertainties in these parameters, their effects on the components of the lateral state and input matrices are computed and the corresponding components of these matrices are changed while designing the controllers.

The uncertainty weight  $W_m$  is of the following form:

$$W_m = \begin{bmatrix} W_{m1} & 0 \\ 0 & W_{m2} \end{bmatrix} \quad (4.50)$$

where the weight  $W_{m1}$  is associated with the aileron input and  $W_{m2}$  with the rudder input.

In order to find  $W_m$ , the perturbed and nominal plants from aileron and rudder to  $v$ ,  $p$ ,  $r$  and  $\phi$  are considered. Relative error curves for aileron and rudder are shown in Figure 4.28 and 4.29, respectively. Since Bode plots of the weights cover all error curves,  $W_{m1}$  and  $W_{m2}$  are found to ensure the stability for the possible perturbations in the uncertainty set.

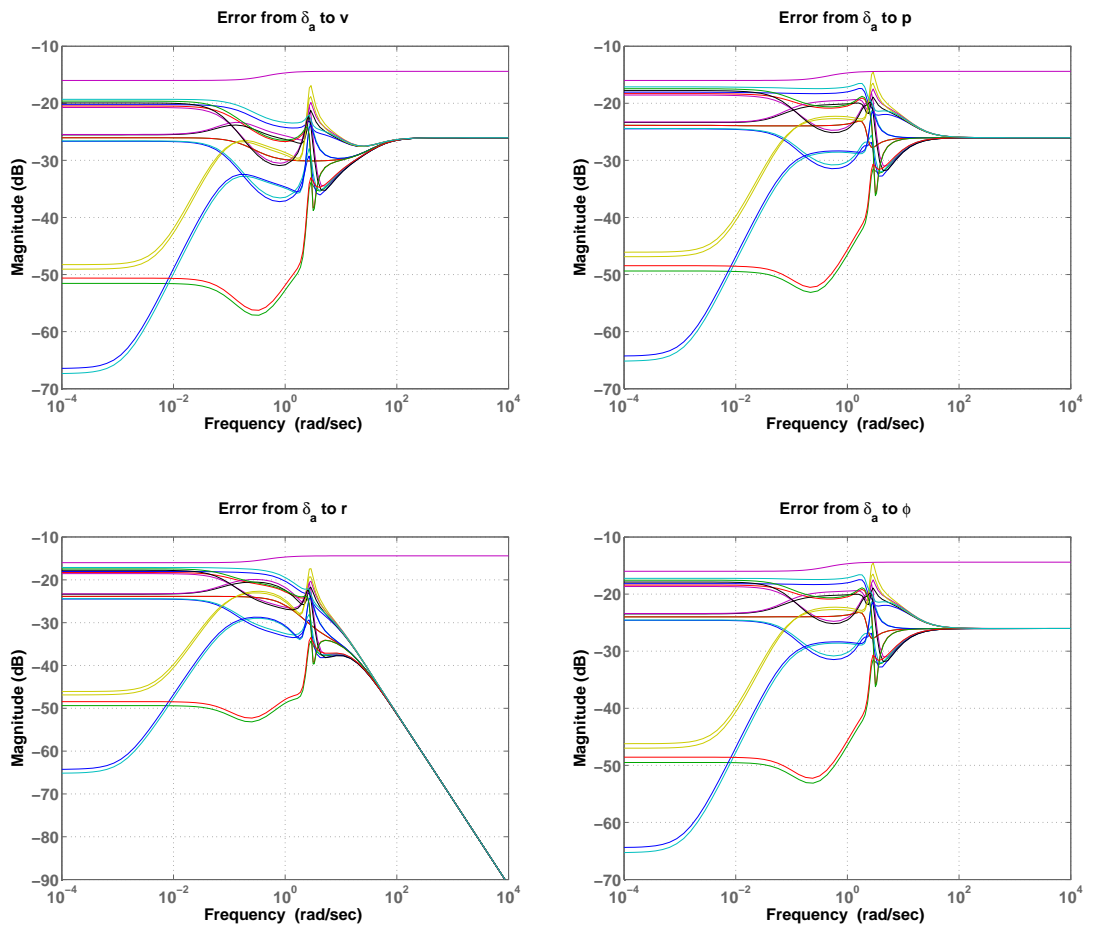


Figure 4.28: Relative Errors for Aileron Inputs

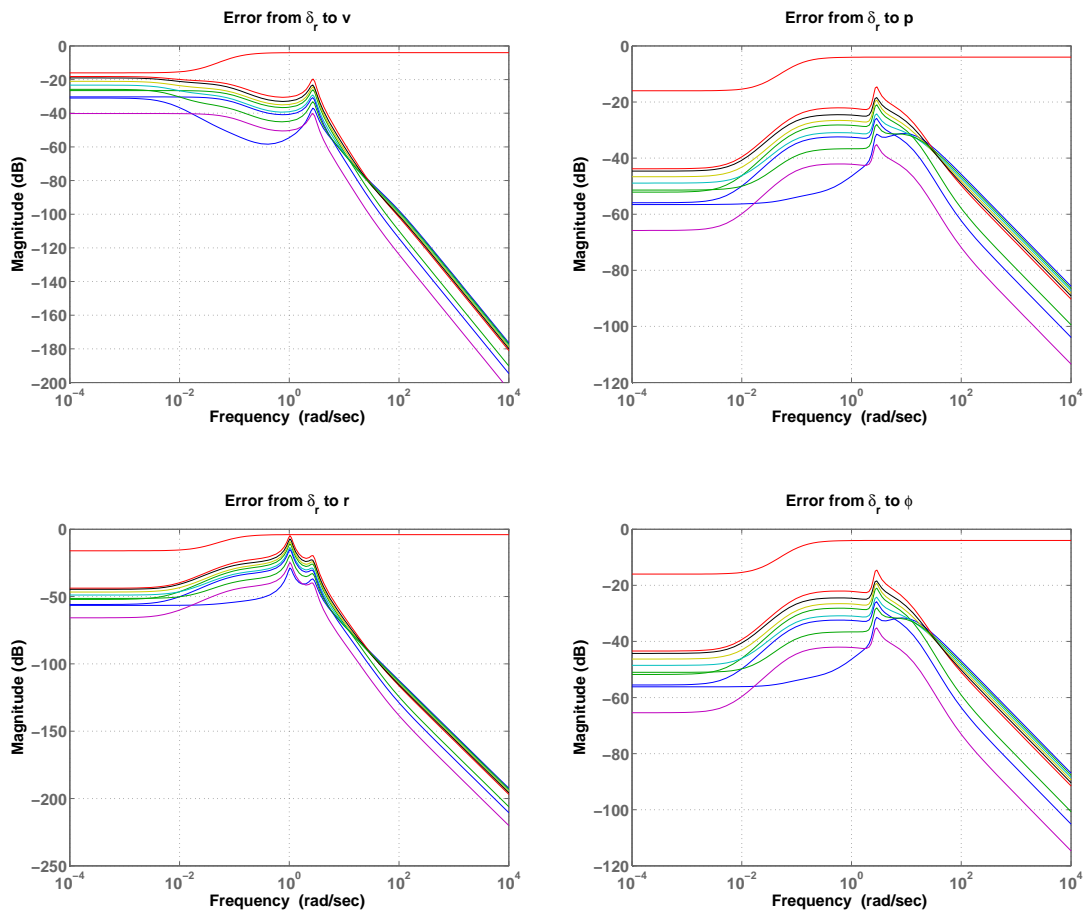


Figure 4.29: Relative Errors for Rudder Inputs

### 4.2.12.3 Robust Performance Analysis

For  $\mu$  analysis, the structured singular value,  $\mu_{\bar{\Delta}}(M(j\omega))$ , is computed at each frequency with

$$\bar{\Delta} = \begin{bmatrix} \Delta_p & 0 \\ 0 & \Delta \end{bmatrix}, \quad \Delta_p \in \mathbb{C}^{4 \times 4}, \quad \Delta = \text{diag}\{\Delta_1, \Delta_2\}, \quad \Delta_1 \in \mathbb{C}^{2 \times 2}, \quad \Delta_2 \in \mathbb{C}^{2 \times 2} \quad (4.51)$$

The  $\mu$  curve for the controller is shown in Figure 4.30. The peak value represents the  $H_\infty$  norm of the system. As can be seen from the results, it is approximately 1 (exact value is 1.01) which ensures that the system has robust performance at all frequencies.

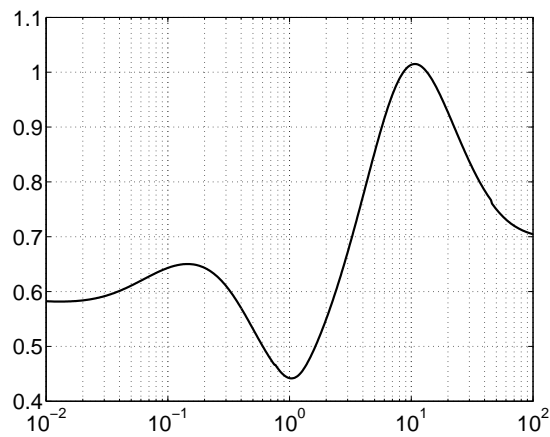


Figure 4.30:  $\mu$  Curve for Robust Performance of the Lateral Controller

## CHAPTER 5

# COMPARISON OF CLASSICAL AND ROBUST CONTROLLERS

This chapter includes the nonlinear simulation results of the classical and robust controllers. Both controllers are designed by using the linear UAV model. As the coupling between the longitudinal and lateral aircraft dynamics is negligible, first separate longitudinal and lateral autopilots are designed. Then, these two automatic flight control system designs are combined together and the full autonomous flight of the UAV is accomplished. Step responses of the classical and robust controllers are compared without use of command filters and it is checked whether the performance requirements are satisfied within the actuator limits. Finally, comparison analyses of the controllers for full autonomous flight are performed through nonlinear simulations for different maneuvers and the simulation results are presented.

### 5.1 Performance Comparison of Controllers for Unit Step Inputs

Responses of the controllers to unit step input commands are compared through nonlinear simulations in the presence of uncertainties. These uncertainties include the variations in the aerodynamic database. As mentioned before, the most important aerodynamic derivatives are  $C_{m_\alpha}$ ,  $C_{m_q}$  and  $C_{m_{\delta_e}}$  for longitudinal dynamics and  $C_{l_\beta}$ ,  $C_{l_p}$  and  $C_{l_{\delta_a}}$  for lateral dynamics. These derivatives are modified in the nonlinear model by adding 5 % of uncertainty to their nominal values. Following sections include the simulation results for the pitch attitude, longitudinal velocity, roll angle and yaw rate responses to elevator, throttle, aileron and rudder inputs, respectively.

### 5.1.1 Pitch Attitude Response

Numerical values of the performance requirements and performance characteristics of the controllers are listed in Table 5.1. Responses of the controllers to a unit step pitch attitude command are illustrated in Figure 5.1. As can be seen from the results, all related performance requirements are satisfied by both designs; however, use of robust controller leads to slightly better performance. Elevator deflection is a few degrees higher for the classical controller at the initial moment of the input and then converges to the same value with the robust controller as shown in Figure 5.2. In addition, classical controller requires a higher elevator deflection rate (Figure 5.3) but it is still within the limits as specified in Table 2.5.

Table 5.1: Performance Comparison of Controllers for Pitch Attitude

	Requirement	Result with CC	Result with RC
% Overshoot	< 15 %	4.47 %	0.5 %
Rise time (s)	< 1	0.664	0.420
Settling time (s)	< 3	0.593	0.304
Steady state error	< 2 %	0.6 %	0.1 %

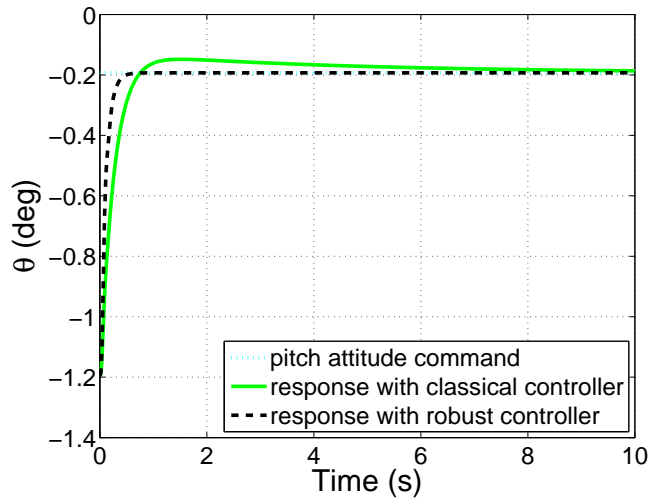


Figure 5.1: Variation of Pitch Attitude with Time

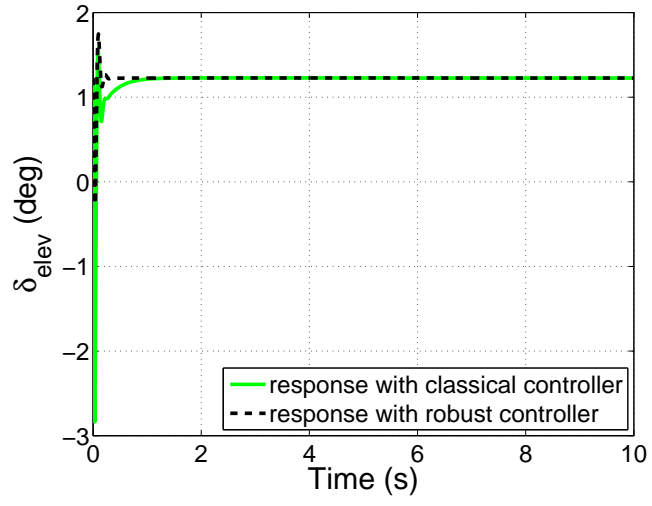


Figure 5.2: Variation of Elevator Deflection with Time

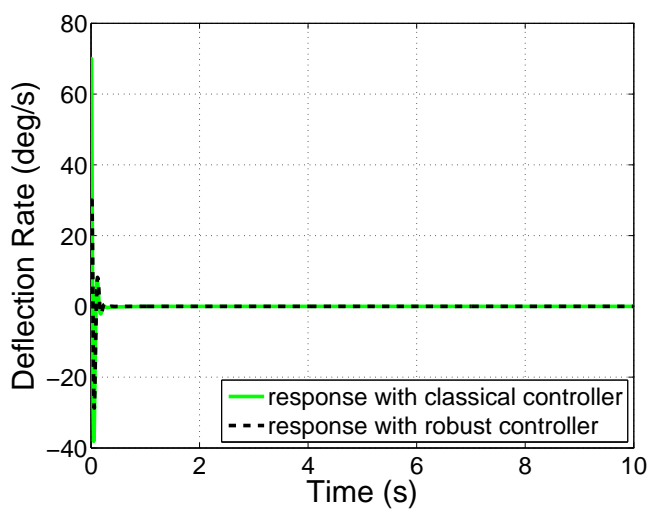


Figure 5.3: Variation of Elevator Deflection Rate with Time

### 5.1.2 Longitudinal Velocity Response

Numerical values of the performance requirements and performance characteristics of the controllers are listed in Table 5.2. Responses of the controllers to a unit step longitudinal velocity command are shown in Figure 5.4. It can be seen that both controllers satisfy the performance requirements; however, steady state characteristic of the classical controller is better. At the initial moment of the input, throttle command and actuator rate are higher for the classical controller as illustrated in Figures 5.5 and 5.6, respectively. High deflection rate is expected because command filters are not used for step response analyses. However, in final simulations they are implemented to the model in order to smoothen the command inputs and decrease the initial high deflection rates.

Table 5.2: Performance Comparison of Controllers for Longitudinal Velocity

	Requirement	Result with CC	Result with RC
% Overshoot	< 15 %	4.76 %	1.80 %
Rise time (s)	< 1	0.460	0.126
Settling time (s)	< 3	0.420	0.211
Steady state error	< 2 %	0.1 %	0.3 %

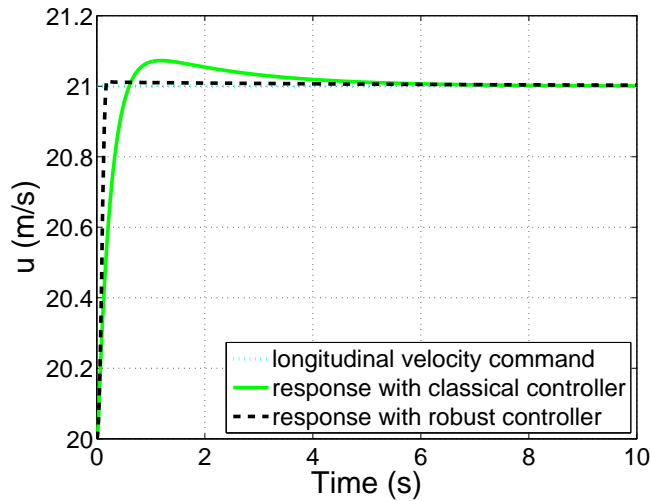


Figure 5.4: Variation of Longitudinal Velocity with Time

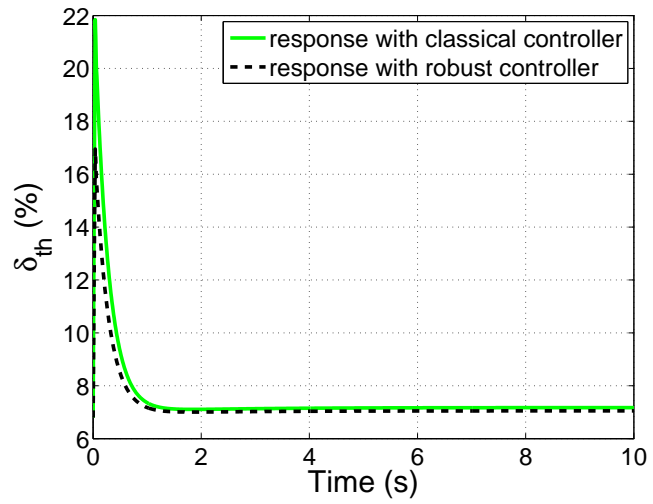


Figure 5.5: Variation of Percent Throttle with Time

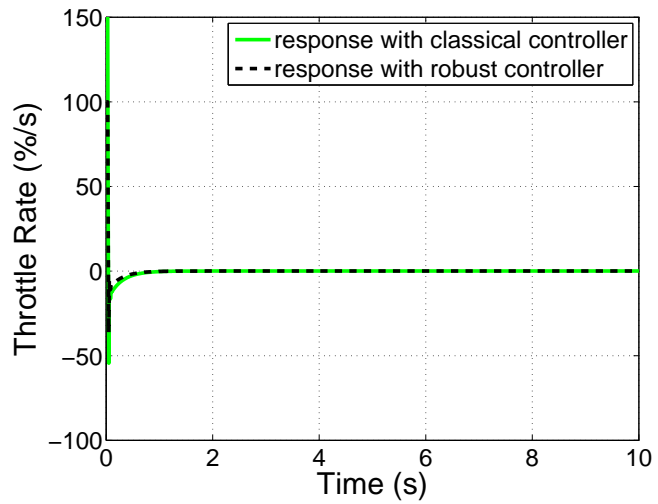


Figure 5.6: Variation of Percent Throttle Rate with Time

### 5.1.3 Roll Attitude Response

Numerical values of the performance requirements and performance characteristics of the controllers are listed in Table 5.3. Responses of the controllers to a unit step roll attitude command are illustrated in Figure 5.7. Results show that characteristics of the roll attitude response of the classical and robust controllers are similar, and both satisfactory for the design requirements. As shown in Figure 5.8, aileron deflections are quite small for both controllers. In addition, deflection rates (Figure 5.9) are within the limits as desired (see Table 2.5).

Table 5.3: Performance Comparison of Controllers for Roll Attitude

	Requirement	Result with CC	Result with RC
% Overshoot	< 15 %	9.35 %	9.22 %
Rise time (s)	< 1	0.401	0.286
Settling time (s)	< 3	1.530	1.005
Steady state error	< 2 %	0.4 %	0.3 %

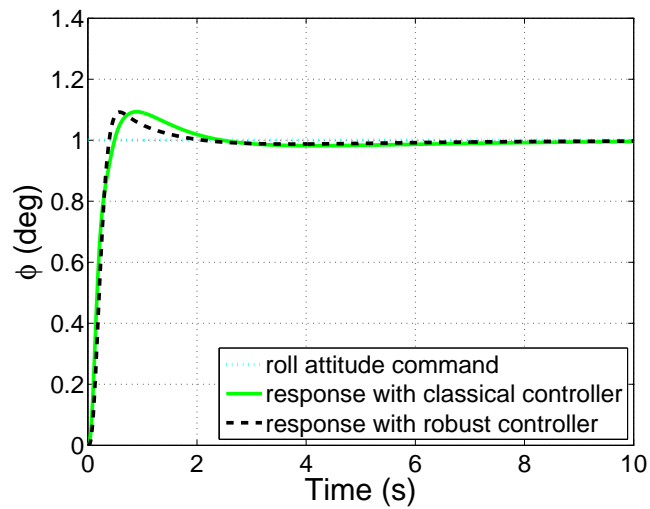


Figure 5.7: Variation of Roll Attitude with Time

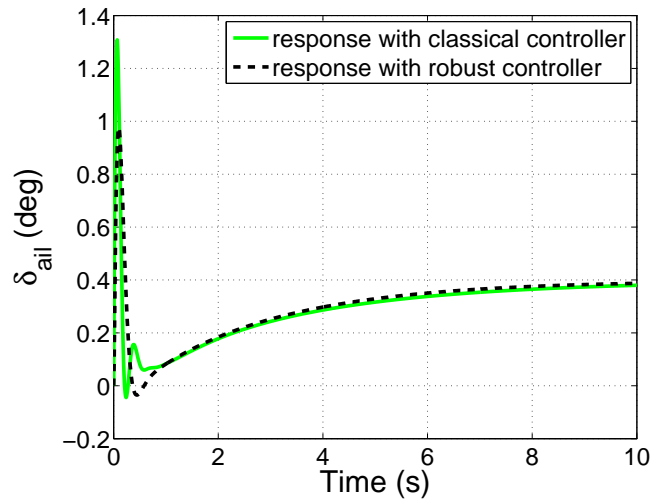


Figure 5.8: Variation of Aileron Deflection with Time

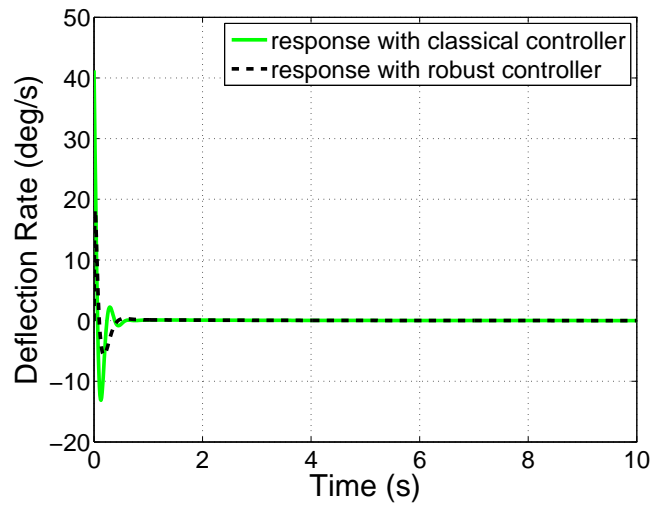


Figure 5.9: Variation of Aileron Deflection Rate with Time

### 5.1.4 Yaw Rate Response

Numerical values of the performance requirements and performance characteristics of the controllers are listed in Table 5.4. Responses of the controllers to a unit step yaw rate command are shown in Figure 5.10. As can be seen from the results, all related performance requirements are satisfied by both controller designs; however, robust controller leads to better performance characteristics. For both controllers, deflections and deflection rates are small as shown in Figures 5.11 and 5.12, respectively. However, robust controller requires a higher deflection rate at the initial moment of the input.

Table 5.4: Performance Comparison of Controllers for Yaw Rate

	Requirement	Result with CC	Result with RC
% Overshoot	< 15 %	13.77 %	6.67 %
Rise time (s)	< 1	0.178	0.133
Settling time (s)	< 3	2.811	2.281
Steady state error	< 2 %	0.4 %	0.3 %

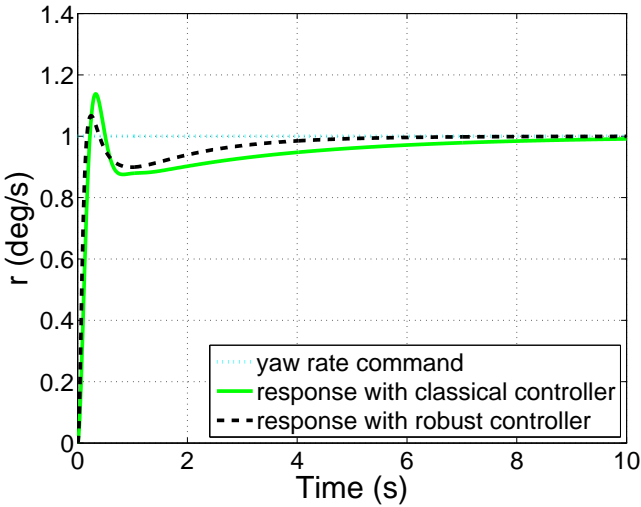


Figure 5.10: Variation of Yaw Rate with Time

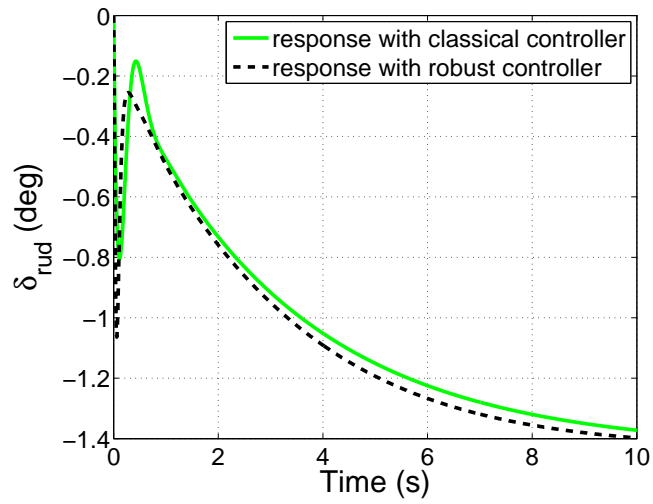


Figure 5.11: Variation of Rudder Deflection with Time

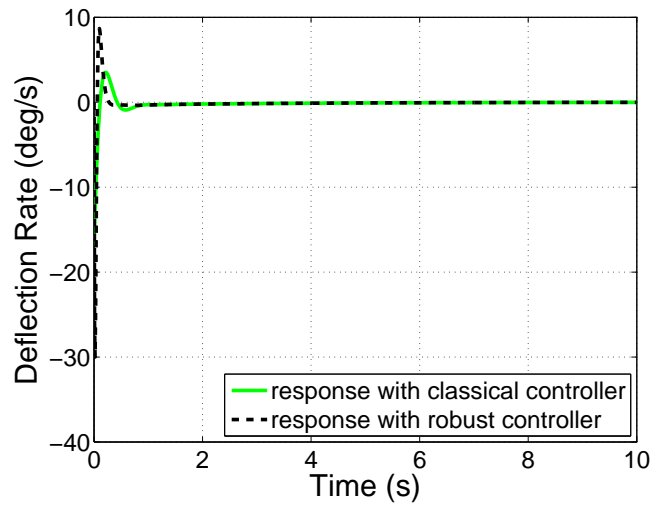


Figure 5.12: Variation of Rudder Deflection Rate with Time

## 5.2 Performance Comparison of Controllers for Full Autonomous Flight

Performances of the controllers for full autonomous flight are tested through nonlinear simulations in presence of both uncertainties and disturbances in the aircraft model. As mentioned in the previous chapter, the uncertainties are resulting from the variations in the aerodynamic database. To account for these uncertainties, the most important aerodynamic derivatives are modified in the nonlinear model by adding 5 % of uncertainty to their nominal values. In addition, disturbances are also included in the simulations as external inputs to account for the measurement noises.

Gaussian noises are added to the respective channels in which sensor measurements are available. Characteristics of the noises are determined according to the flight test data of the UAV. For this purpose, a separate simulation model is utilized. In this model, flight test data of the UAV, which includes the onboard sensor noises, is combined with a Kalman filter. Noise characteristics obtained from this model are listed in Table 5.5.

Table 5.5: Gaussian Noise Characteristics

	Standard Deviation ( $\sigma$ )
u	0.0516 (m/s)
$\theta$	0.8881 (deg)
h	1.7337 (m)
$\phi$	0.7277 (deg)
r	2.1715 (deg/s)

To check the performance of the perturbed plant, first the values presented in Table 5.5 are used in the simulations. Since Kalman filter outputs are taken at 10 Hz, Gaussian noises are fed to the system at 10 Hz and then re-sampled to 100 Hz by rate transition. However, when given one at a time, these noises led to large oscillations in control surface deflections and throttle input. In such a case, using low-pass filters is a common approach to reduce the effect of noises. Thus, in the thesis, the problem caused by high standard deviations, is solved by implementing low-pass filters to the simulation model. In addition to the Gaussian noises, 1 degree bias to pitch and roll attitudes, 1 m/s bias to velocity, 1 deg/s bias to yaw rate and 1 m bias to altitude are also added to consider the effect of bias errors on the UAV.

Simulations for different longitudinal and lateral maneuvers are carried out to test the performances of the controllers. In addition to uncertainties in the aerodynamic database and sensor noises, gust loads are also applied in some simulations to demonstrate the capabilities of the controllers. Results for both classical and robust controllers are presented in the following sections for comparison purposes.

### **5.2.1 Longitudinal Maneuvers**

The airplane is commanded to carry out two different longitudinal maneuvers. In the first simulation, the airplane is required to decrease its velocity by 5 m/s while holding its altitude. As can be seen from the results shown in Figure 5.13, the airplane slows down 5 m/s while the altitude is kept constant at its initial value of 1000 m as desired. There is no deviation in the straight flight path at a northerly heading. In the second simulation on the other hand, the airplane is commanded to acquire 50 m altitude and 5 m/s velocity. During the simulation, vertical wind gust of 2 m/s is also applied for a short duration. Results given in Figure 5.14 show that, the airplane successfully climbs the commanded altitude within 15 seconds as it increases its velocity by 5 m/s and maintains this new flight condition. The wind gust input around 20 s is also counteracted. Simulation results illustrate that, both classical and robust controllers perform very well at tracking the command inputs. Both controllers tolerate the measurement noises and uncertainties which lead the aircraft to achieve the desired maneuvers without any deviation in lateral channel. The only difference between the responses of the controllers can be realized in the actuator behaviors. That is, classical controller is slightly more sensitive to the noises than the robust controller. However, oscillations in elevator and throttle inputs are still small and acceptable.

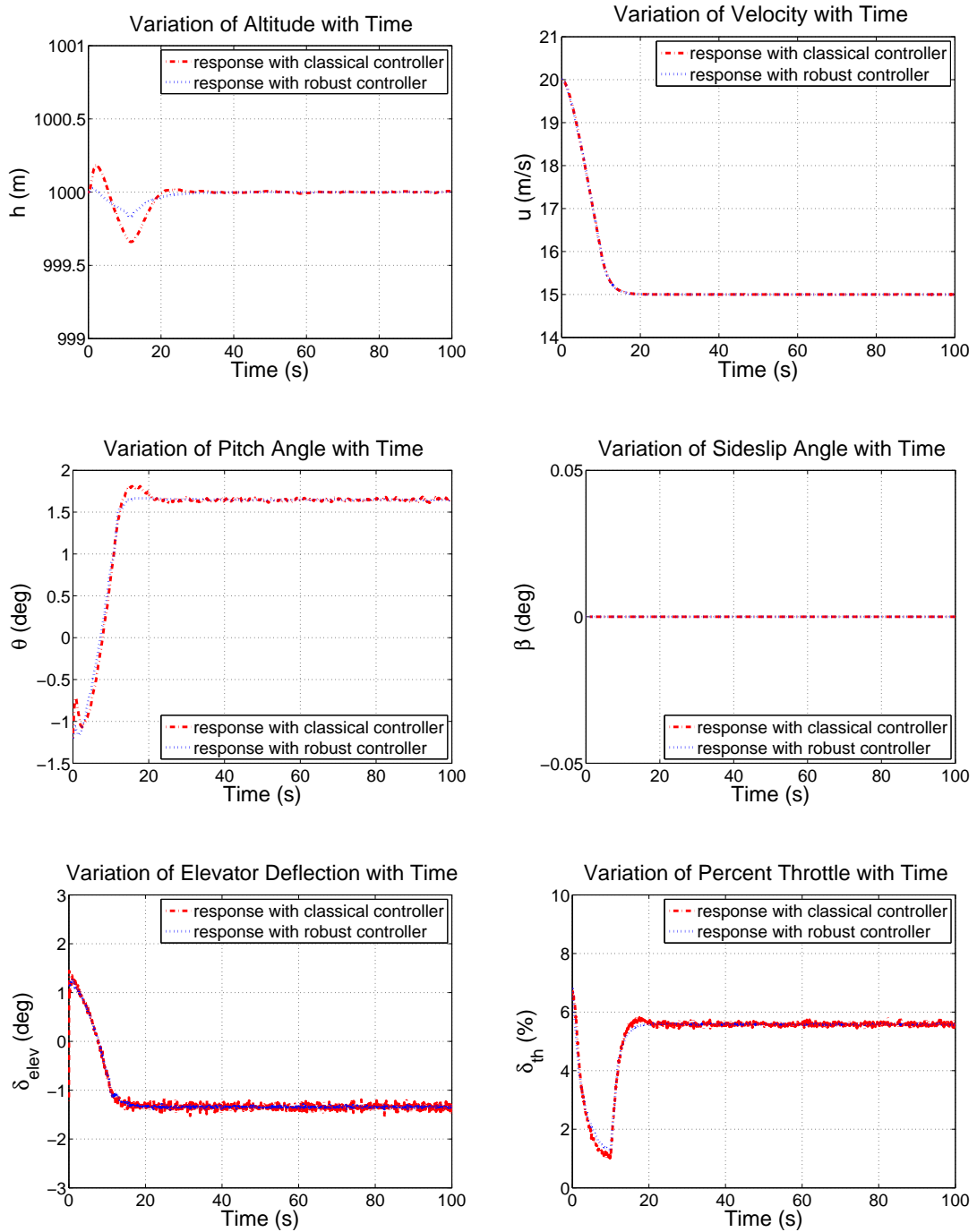


Figure 5.13: Simulation Results for Decreasing Velocity by 5 m/s at Constant Altitude

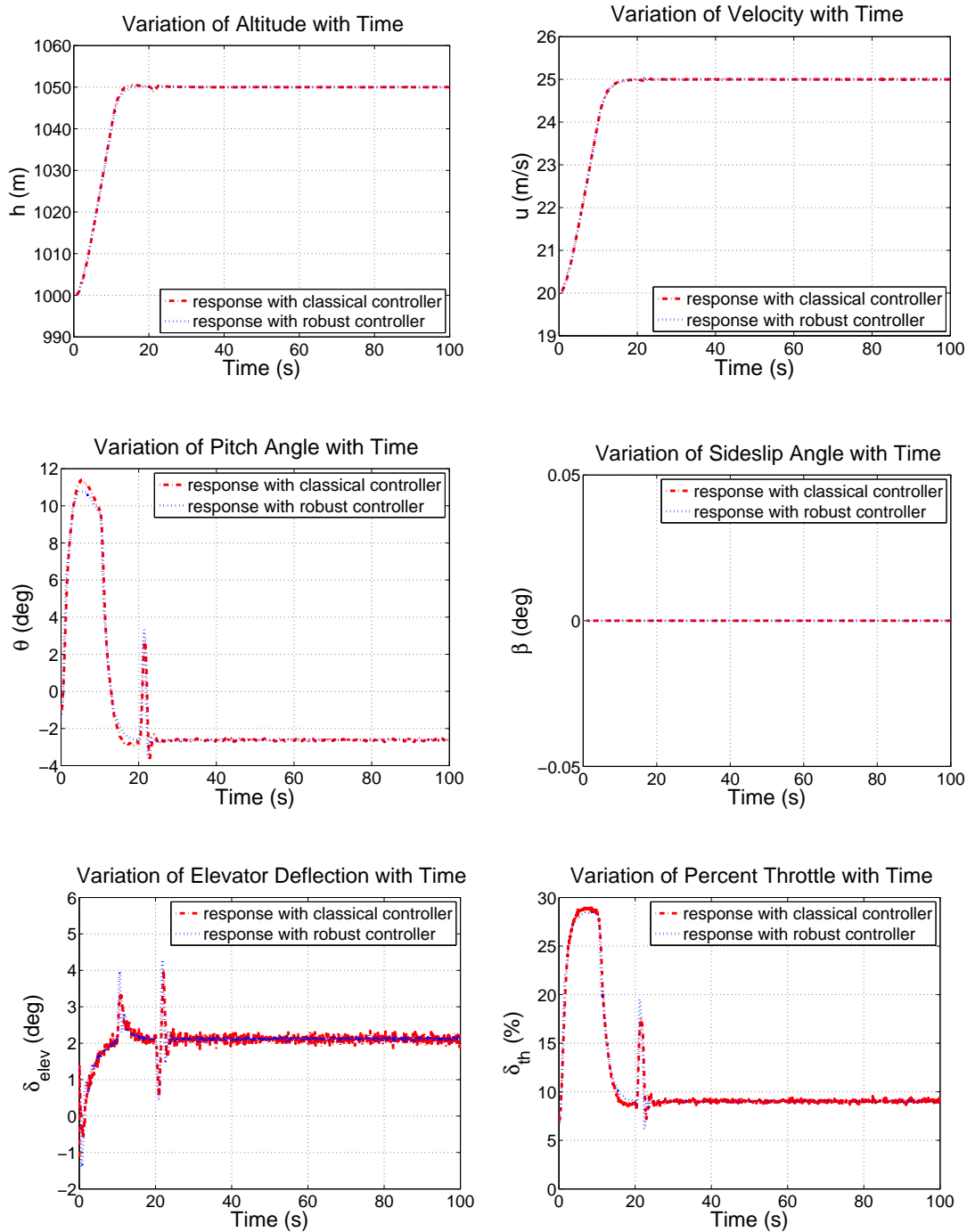


Figure 5.14: Simulation Results for Increasing Altitude by 50 m while Increasing Velocity by 5 m/s

### 5.2.2 Lateral Maneuvers

The airplane is required to achieve two different lateral maneuvers. In the first simulation, the aircraft is commanded to carry out a coordinated turn with 3 deg/s turn rate from a steady straight flight. As it may be observed from the results given in Figure 5.15, the airplane achieves the desired turn without any offset and maintains this new flight condition. In the second simulation, the airplane is required to make a roll maneuver. To test the capabilities of the controllers, lateral wind gust of 2 m/s is also acted at 20<sup>th</sup> second. In Figure 5.16, the simulation results of this 10 degree roll attitude acquire and hold is shown. The airplane achieves the desired maneuver while the altitude and velocity are kept constant. Effect of the lateral wind gust can be seen at 20<sup>th</sup> second; however the roll attitude and yaw rate are acquired back again right after the gust is removed.

Simulation results show that both classical and robust controllers show satisfactory performances for the UAV model considered. They are both capable of tracking the command inputs and realizing these commands without any offset in altitude or velocity. Moreover, effect of the wind gust is eliminated while effects of the uncertainties and measurement noises are tolerated as desired. The point here is robust controller design is carried out considering the variations in the aerodynamic database. Hence, it is internally able to handle with uncertainties. However, the simulation results show that classical controller is also capable of tolerating the uncertainty effects. In addition, as demonstrated in the longitudinal maneuvers previously, robust controller again leads to slightly smaller oscillations in control surface deflections. However, since the magnitude of the oscillations are small for both controllers, it can be concluded that the classical and robust controller designs are successful in tolerating the sensor noises.

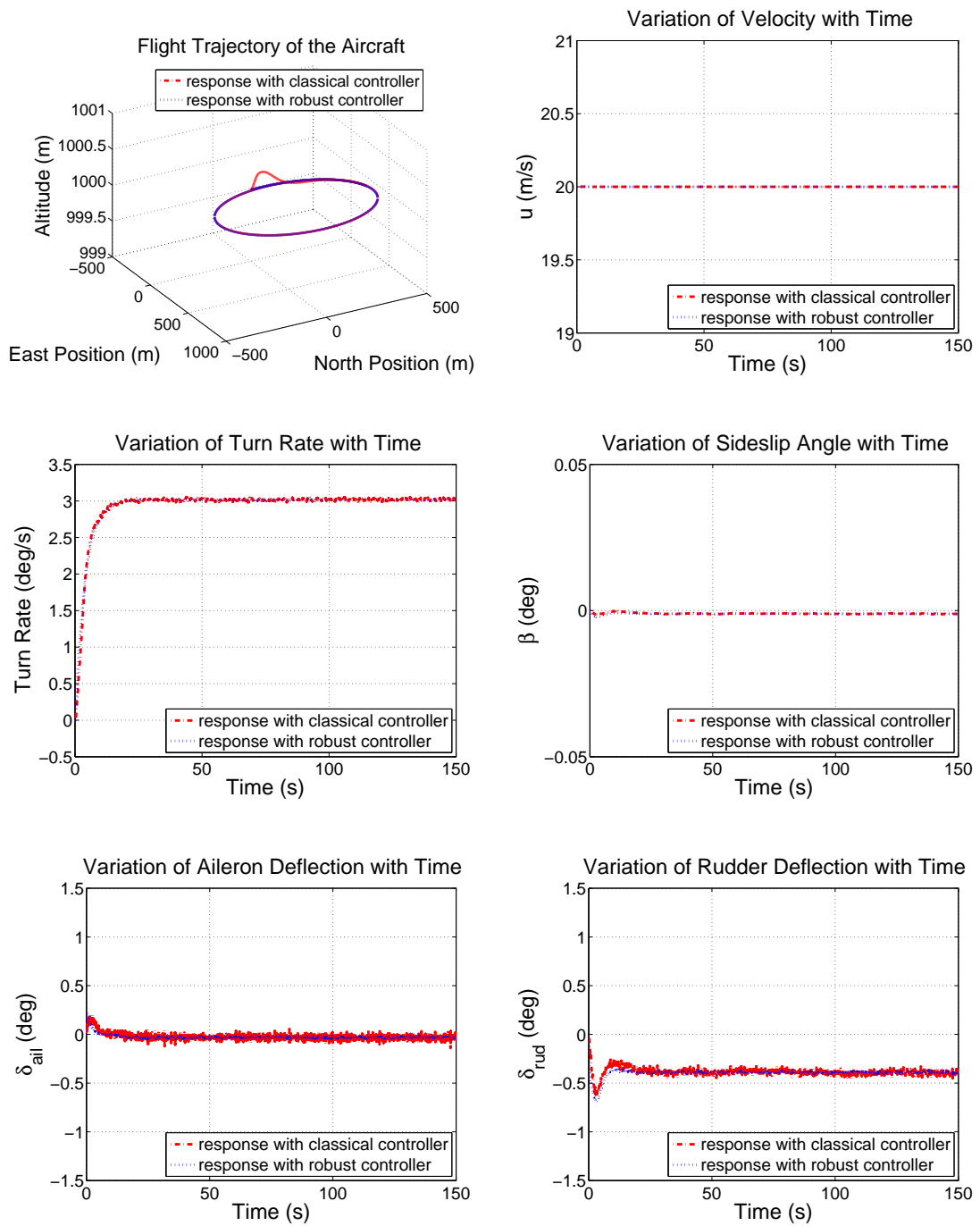


Figure 5.15: Simulation Results for a Coordinated Turn with 3 deg/s Turn Rate

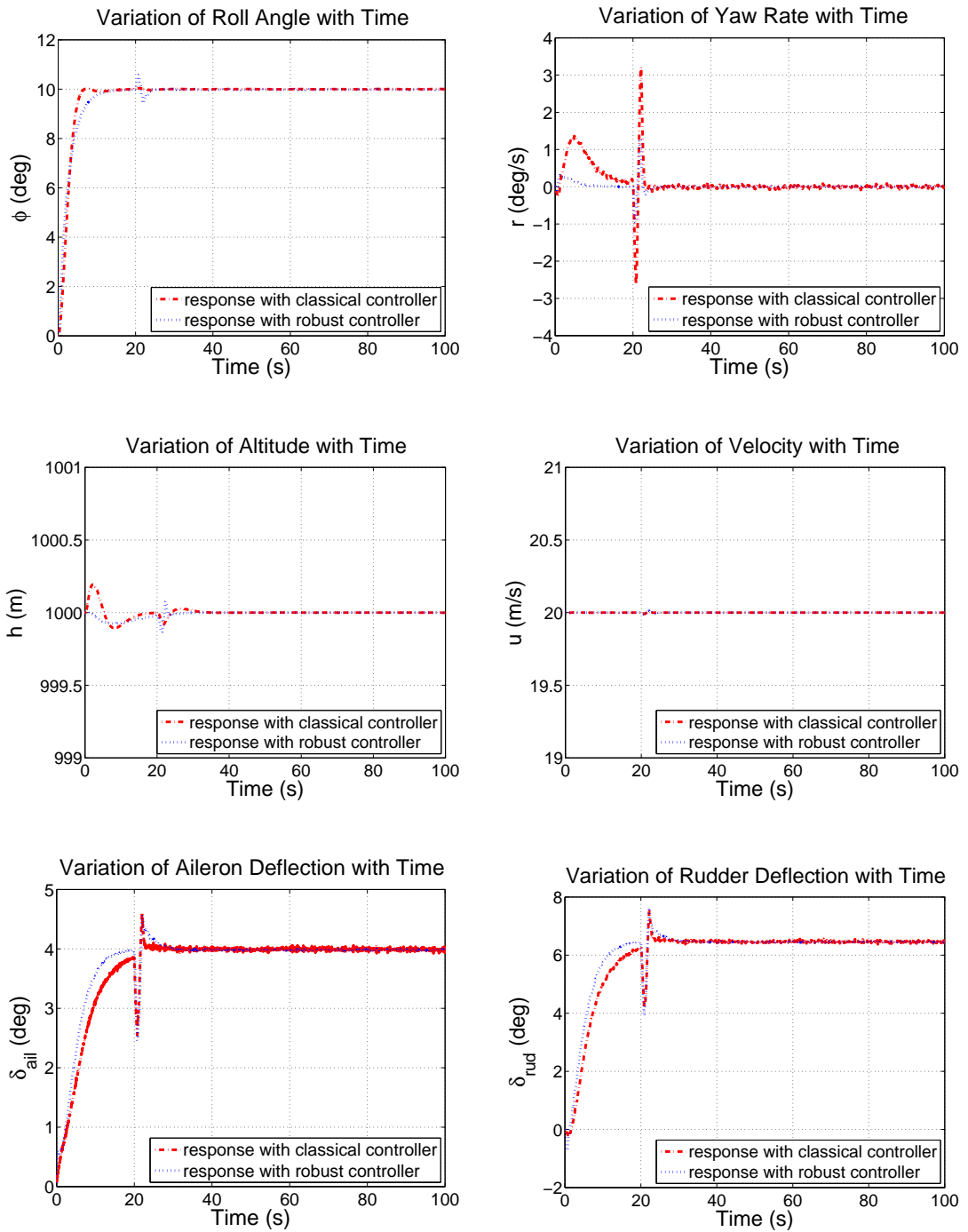


Figure 5.16: Simulation Results for a Fixed Roll Maneuver

## **CHAPTER 6**

### **FAULT TOLERANT CONTROLLER DESIGN FOR AN OVER ACTUATED UAV**

The scope of this chapter is to provide information about the control allocation methods applied in the thesis and to explain the controller configuration of the over actuated UAV. For this purpose, first the allocation methods, namely Moore-Penrose pseudo inverse and blended inverse algorithms, are discussed. Next, over actuated mechanism of the controls is defined and the control system configuration is explained. Then, determination of the controller gains and allocation weights are discussed. Simulation results for comparison of allocation methods and demonstration of effectiveness of the selected algorithm for different scenarios are presented at the end of the chapter.

#### **6.1 Allocation Methodology**

In the thesis, the primary objective is to address the fault tolerant control of an over actuated UAV. For this purpose, the traditional ailerons are divided into 3 segments and each of them is commanded independently. When dealing with such an over actuated system, determining how to transform the control commands into individual control surfaces may be difficult. Control allocation is used at this stage to define the relation between the forces and moments (or accelerations), and actual physical controls of the over actuated UAV. By allocating commands to the individual control surfaces, required forces and/or moments that are specified by a control law can be achieved in the limit of the system capabilities.

For an over actuated system, the main concern is the method used in allocating redundant controls. Static control allocation methods are widely used to steer redundant robot manipulators [36] and control moment gyroscopes [52] for singularity avoidance, obstacle avoidance, performance optimization [2]. For aircrafts, control allocation methods can be used to have an authority on the controls in order to enhance survivability, maneuverability as well as reliability.

Linear aircraft flight mechanics equations can be written as in the following form:

$$\dot{x} = Ax + B\delta \quad (6.1)$$

where,  $x$  are the states and  $\delta$  are the physical controls such as surface deflections, thrust inputs etc. Equation 6.1 may also be written as:

$$\dot{x} = Ax + u \quad (6.2)$$

In equation 6.2,  $u$  represents the specific forces and moments required steer the aircraft. Then, the relation between the specific forces and moments, and actual physical controls can be defined as in equation 6.3.

$$u = B\delta \quad (6.3)$$

In conventional designs, three control surfaces (elevator, ailerons and rudder) provide pitch, roll and yaw controls. For such a non-redundant system, the Jacobian matrix  $B$  is square. Thus, it is invertible and the solution is unique unless it is non-singular ( $\det(B) \neq 0$ ). However, for over actuated systems, inverting the Jacobian matrix requires some additional considerations. When the physical controls are more than the desired specific forces and moments, the  $B$  matrix is rectangular and may not be directly inverted to find the physical controls. Inverse kinematic algorithms are used for determining the control surface deflections for desired specific forces and moments by proposing different allocation approaches.

The common feature of the static control allocation methods such as Moore-Penrose Pseudo (MP) inverse, weighted MP Inverse, singularity robust (SR) inverse and blended inverse (BI) is that, they can be applied regardless of the flight control system. Thus, in the thesis, static solutions are preferred and two methods are examined: Moore-Penrose pseudo inverse and blended inverse. These allocation methodologies are described in the following sections.

### 6.1.1 Moore-Penrose Pseudo (MP) Inverse

Moore-Penrose pseudo (MP) inverse steering law is one of the most common methods. It is a simple algorithm which finds the controls that minimize the square of the error (Equation 6.4).

$$u_e = B\delta - u \quad (6.4)$$

$$\min_{\delta} (u_e^T u_e) \quad (6.5)$$

The above minimization problem gives the following solution:

$$\delta_{MP} = B^T [BB^T]^{-1} u \quad (6.6)$$

Most of the steering laws are pseudo inverse based. However, the main problem in these inverse kinematic algorithms is that the Jacobian matrix is required to be non-singular. This is because when  $B$  is singular,  $\det(BB^T)$  becomes zero and as a result equation 6.6 fails.

In addition to the singularity problem, with MP-inverse it is not possible to supply an authority on the controls. For an over actuated system, there may be several combinations of control surface deflections which may result in the same system performance. However, the aim is obtaining the desired forces and torques while also controlling the deflections of each control surface. This cannot be achieved by using MP-inverse since the allocation is not controllable.

### 6.1.2 Blended Inverse (BI)

The main difficulty in control allocation is to be able to generate the desired forces and torques necessary for control together with selectively allocating these controls to different actuators. The only method that realizes this double objective is the blended inverse (BI) algorithm. The algorithm is successfully applied to the steering of control moment gyroscopes [49], and to the allocation of controls during transition phase flight control of a tilt-duct UAV [48].

BI control allocation algorithm is derived from the following mixed minimization problem:

$$\min_{\delta} \frac{1}{2} \{ \delta_e^T Q \delta_e + u_e^T R u_e \} \quad (6.7)$$

In equation 6.7,  $\delta_e = \delta - \delta_{des}$  and  $u_e = B\delta - u$ . Hence, the error between the desired and realized physical controls as well as the error between the desired specific forces (and/or moments) calculated as the feedback algorithm requirement is blended, and minimized. The symmetric positive definite weighting matrices  $Q$  and  $R$  are used to define the relation between the relative importance of the objectives.

The solution of the minimization problem gives,

$$\delta_{BI} = [Q + B^T R B]^{-1} [Q \delta_{des} + B^T R u] \quad (6.8)$$

In equation 6.8,  $Q = qI_n$  where  $q$  is the blending coefficient and  $I_n$  is an  $n \times n$  identity matrix. Considering the weighing matrix  $R$  as an identity matrix, equation 6.8 can be reduced to:

$$\delta_{BI} = [qI_n + B^T B]^{-1} [q\delta_{des} + B^T u] \quad (6.9)$$

## 6.2 Control Allocation for the UAV

### 6.2.1 Over Actuated Mechanism of Controls

Over actuated UAV model has the same longitudinal controls namely, an elevator and an engine. However, there are three sets of ailerons (inner, middle and outer) instead of one. These aileron sets, together with the rudder, are employed to provide roll and yaw controls. Inputs to the over actuated UAV are shown in equation 6.10.

$$\delta = \begin{bmatrix} \delta_{elev} (deg) \\ \delta_{th} (\%max) \\ \delta_{ail_{in}} (deg) \\ \delta_{ail_{mid}} (deg) \\ \delta_{ail_{out}} (deg) \\ \delta_{rud} (deg) \end{bmatrix} \quad (6.10)$$

## 6.2.2 Controller Configuration

Linearization results of the over actuated UAV showed that the coupling effects between the longitudinal and lateral airplane dynamics are negligible. Hence, as previously done for the conventional UAV, separate longitudinal and lateral autopilots are designed and combined together for full autonomous flight. Controller design technique for these autopilots is determined according to the simulation results presented in the preceding chapter.

In the previous chapter, performances of classical and robust controllers are compared through simulations. These nonlinear simulations are carried out for different maneuvers to test the capabilities of both designs in presence of uncertainties, measurements noises and wind gusts. The results presented in Chapter 5 show that, both classical and robust controllers perform almost equally well for the UAV model considered. Both designs are able to follow the command inputs without any offset, tolerate the measurement noises as well as uncertainties in the aerodynamic database and counteract the wind gusts. Although robust controller is expected to be capable of tolerating the system uncertainties and sensor noises, the results illustrate that classical controller also leads to satisfactory results while handling the uncertainties and noises. Thus, classical control techniques are preferred while designing the control system of the over actuated UAV.

In the thesis, flight control system design for the over actuated UAV is carried out by using classical sequential loop closing methods. For the longitudinal autopilot, same feedback system is used with exactly the same gains as for the conventional UAV. On the other hand, a new lateral autopilot is designed due to the increased number of control inputs in this channel. Figure 6.1 gives the block diagram on how the controls are allocated to redundant actuators in the automatic flight control system. The control allocation block accepts the desired controls in terms of specific forces and moments from the autopilot and generates surface deflection commands to the controls according to the allocation policy or algorithm used.

Note that the flight control systems are designed using the linearized UAV dynamics for the over actuated case and then tested for different maneuvers through nonlinear simulations. Linearized matrices for the longitudinal and lateral dynamics can be found in Appendix C. First order command filters are used in the simulations to shape the command signals for two reasons: to match the dynamics of the aircraft and limit the actuator deflection rates.

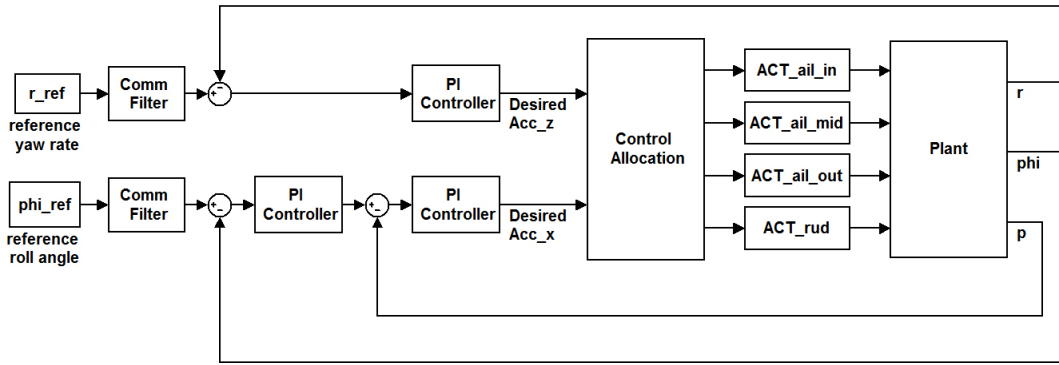


Figure 6.1: Block Diagram of the Control System

### 6.2.3 Determination of the Controller Gains

During the design phase of the flight control system (including the control allocation algorithm), first the controller gains and then, the allocation policy are determined. The reason is, first it must be confirmed that the desired specific forces and moments are generated from the desired command inputs (reference roll angle and yaw rate) appropriately. For this purpose, the system structure shown in Figure 6.1 is modified.

Figure 6.2 illustrates the block diagram of the new system used for finding the controller gains. Control allocation method is combined with the lateral UAV dynamics in one block. Considering equation 6.2, it is assumed that the specific moments  $\alpha_x$  and  $\alpha_z$  affect the roll and yaw rates directly.

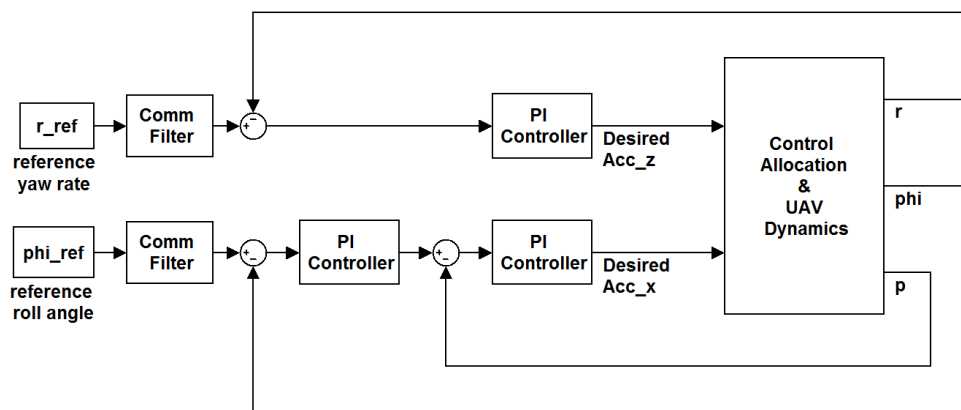


Figure 6.2: Block Diagram of the Combined System

Controller gains are found according to the methods discussed in Section 4.1 and listed in

Table 6.1. Roll and yaw rate errors are converted to desired acceleration commands via PI controllers as no derivative term is needed. Roll rate command is generated from the roll angle error as shown in Figure 6.2. Gains of this controller are the same with the ones given in Table 4.2.

Table 6.1: Controller Gains

	$K_p$	$K_i$	$K_d$
p	25	10	0
r	20	5	0

After finding the controller gains, first the unknown parameters in the BI algorithm and then the allocation policy are determined. Following section is about choice of the weights in BI algorithm. Allocation policy is selected according to the simulation results presented in Section 6.3.1.

#### 6.2.4 Determination of the Weightings in Allocation

As mentioned in Section 6.1.2, BI algorithm generates the desired specific forces and moments while also deriving the controls to the desired positions. The blending coefficient  $q$  is a key parameter which defines the relative importance between the two objectives. The priority between the desired acceleration command ( $u$ ) and desired control input ( $\delta$ ) is determined according to its value.

Usually  $q$  is taken as a small number to emphasize the importance of the desired accelerations. This is also the reason for the  $R$  matrix in equation 6.8 to be taken as identity. If the controls deviate from their desired positions,  $q$  may be increased to make the desired control inputs dominate the equation. However, in this case, if the desired controls supplied to the BI algorithm are irrelevant, the desired accelerations may not be obtained.

In the thesis, the most suitable value for  $q$  is obtained by iterations. Values from  $10^{-5}$  to  $10^1$  are tried and it is found that  $10^{-3}$  is the best choice for satisfying both the desired acceleration and actuator position commands. This value for  $q$  lets to obtain the desired accelerations if the controls supplied to the BI realize the same specific forces and moments. In addition, even if the desired controls are irrelevant, the BI algorithm realizes the desired accelerations since the blending coefficient  $q$  is a small number.

## 6.3 Results and Discussion

In this section, nonlinear simulation results for four case studies are presented. The first study is carried out to determine the control allocation method that yields the best airplane response for the desired tasks. In this study, Moore-Penrose pseudo (MP) inverse and blended inverse (BI) control allocation techniques are compared for a roll maneuver. After selecting the allocation method according to the simulation results of the first study, second and third case studies are carried out. These studies are also based on some possible scenarios that may be confronted during the flight. In the last study, system responses with and without using BI method are compared. The key point in the simulations is that, the controller is not informed about the actuator failures to demonstrate the fault tolerant behavior of the flight control system. Gust loads are also applied in order to test the abilities and performances of both the flight control system and the BI technique even further.

### 6.3.1 Scenario-1

In order to determine the control allocation method, a case study is carried out. In this first study, MP-inverse and BI techniques are compared through nonlinear simulations for a possible scenario. To test the effectiveness of these techniques under certain critical conditions, actuator limits of the ailerons are decreased to 10 degrees and the aircraft is commanded to make a simple roll maneuver. According to the scenario, it is assumed that at the 20<sup>th</sup> second of the maneuver the most important aileron pair, namely the outer one, is got stuck at its neutral position.

The simulation results presented in Figure 6.3 show that both MP-inverse and BI control allocation techniques performed pretty well, realizing the desired maneuver. The UAV acquires the commanded roll attitude while altitude and velocity are kept constant at their trim values. However, considering the simulation results given in Figure 6.4, it can be seen that with MP-inverse, middle aileron saturates soon after the outer aileron pair is lost. In fact, this result is expected from the MP-inverse since the allocation is not controllable with this technique. On the other hand, with BI algorithm, neither of the remaining controls is saturated. This is because the allocation with BI algorithm is carried out by purposefully commanding equal deflections for the inner and middle aileron pairs.

In the thesis, BI control allocation technique is preferred since it lets to perform both of the desired tasks. With this method, not only the desired specific moments (controller outputs) are produced, but also the controls are allocated to the corresponding actuators selectively. In this case, actuator saturations are also avoided due to the authority on the controls defined by the weightings and desired control inputs. Thus, this method is used for the simulation scenarios presented for the rest of the thesis.

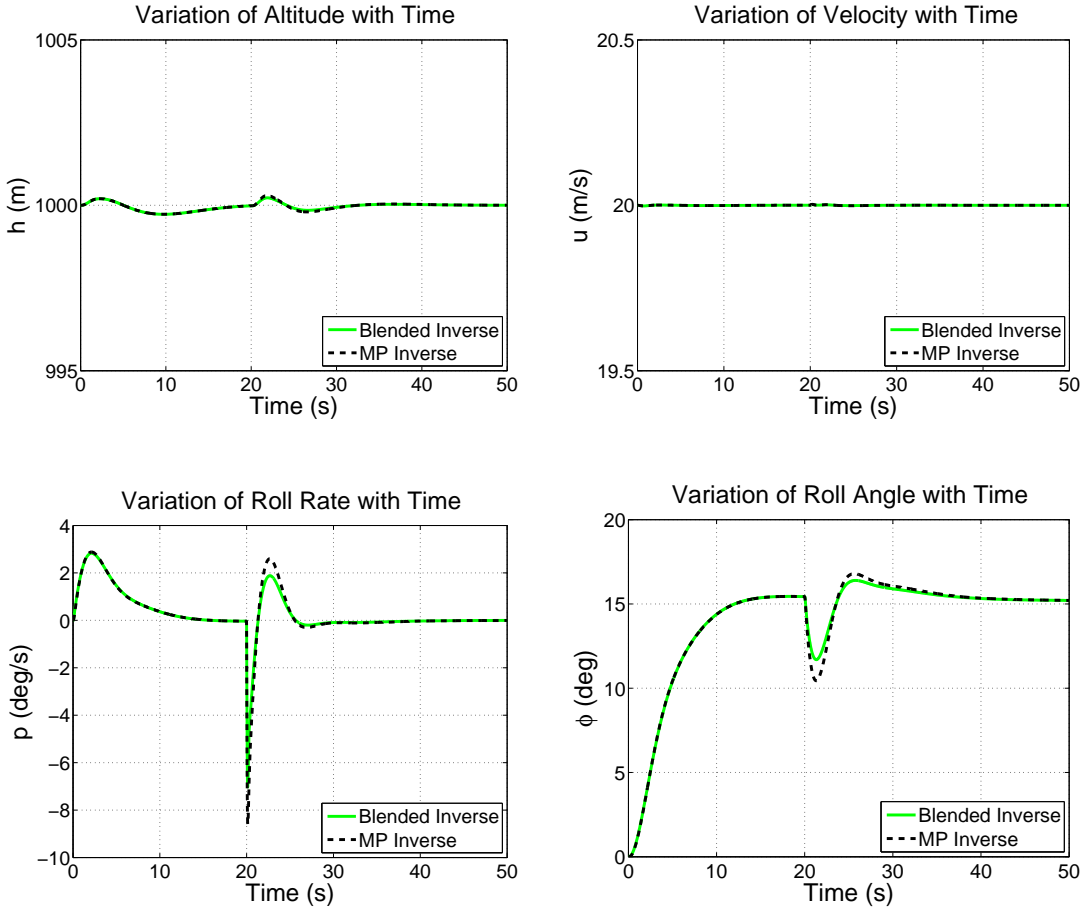


Figure 6.3: Simulation Results for Comparison of MP-Inverse and Blended Inverse Methods

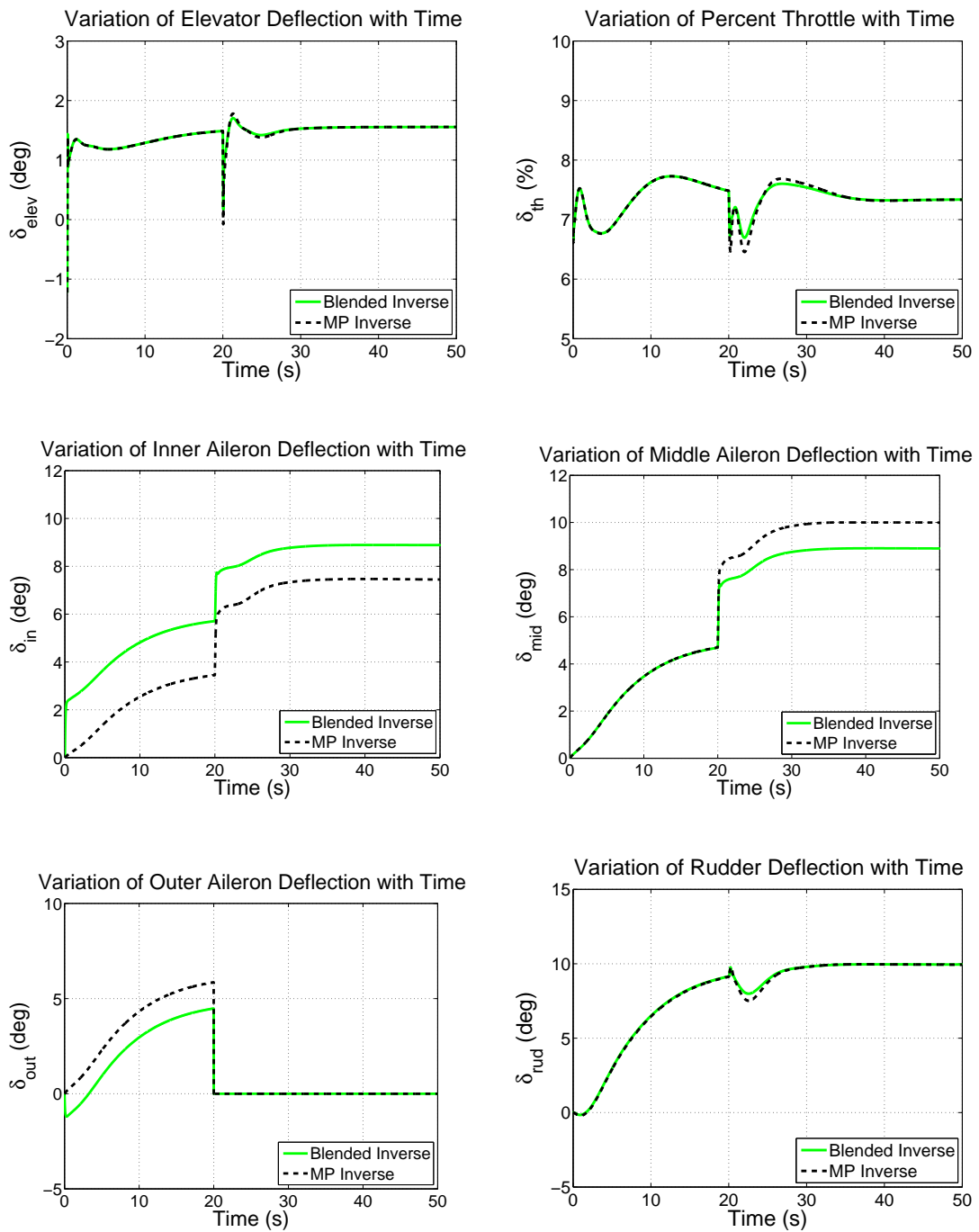


Figure 6.4: Variations of the Controls for Comparison of MP-Inverse and Blended Inverse Methods

### 6.3.2 Scenario-2

The purpose of this second study is to test if redundant set of control surfaces are capable of preventing airplane loss when some aerodynamic control surfaces are not operating. To demonstrate what may happen to a UAV with the loss of ailerons a simulation is carried out. In Figure 6.5, variations of the controls of the conventional UAV during a 15 degree roll attitude acquire and hold is shown. 40 seconds after the simulation is started, the ailerons are lost. As can be seen from the results, after that moment, on the airplane all controls are lost as well. Furthermore, the simulation results given in Figure 6.6 show that, the aircraft goes into a spin while its velocity, roll rate and roll angles oscillate and deviate from their required values.

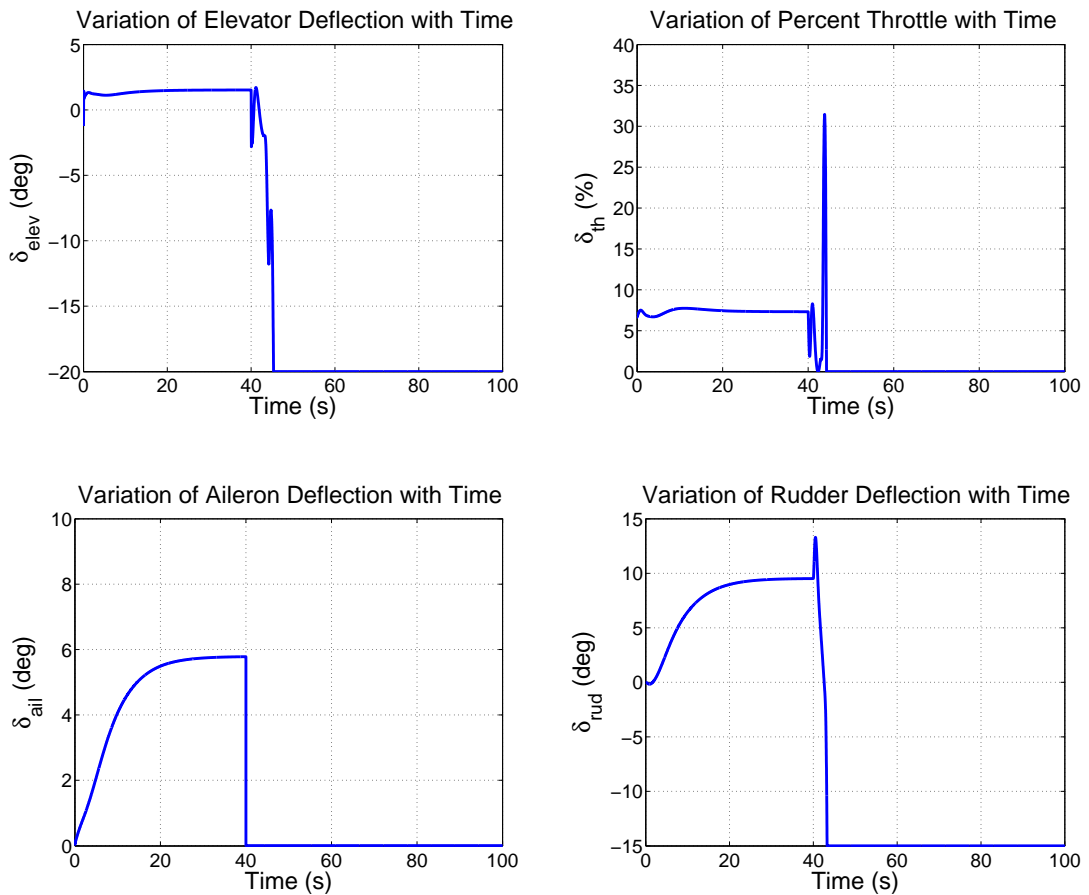


Figure 6.5: Variations of the Controls for a Roll Maneuver with Conventional UAV

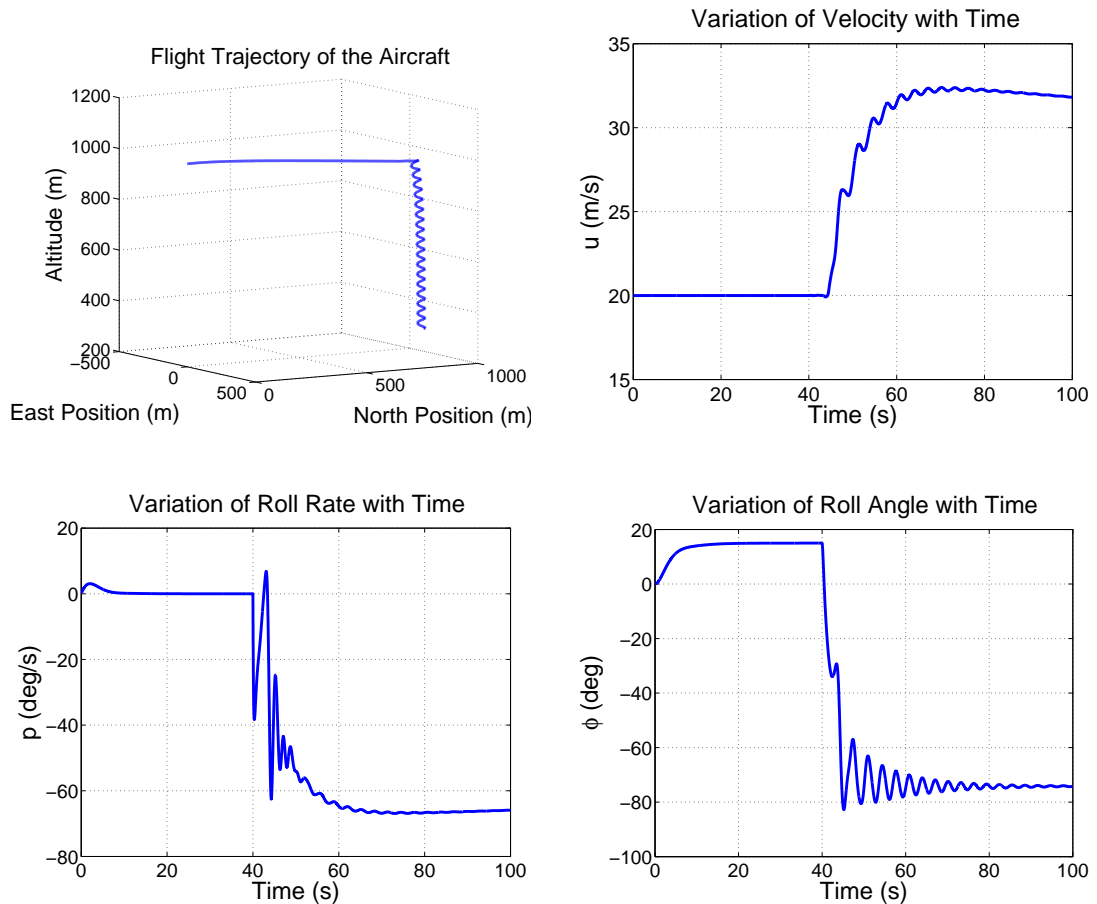


Figure 6.6: Simulation Results for a Roll Maneuver with Conventional UAV

The same 15 degree roll attitude acquire and hold scenario is repeated for an over actuated UAV with three redundant set of ailerons. As explained in the previous section, the control allocation is carried out using the blended inverse algorithm. Variations of the controls are illustrated in Figure 6.7. First the inner and then the middle aileron pairs are lost at 30<sup>th</sup> and 40<sup>th</sup> seconds, respectively. In addition, during the simulation a gust loading is also applied that generates 5 deg/s roll rate disturbance for a short duration. It may be observed from the simulation results given in Figure 6.7 and 6.8 that, although the controller itself is not aware of the aileron losses, the feedback system tries to compensate this situation by commanding higher level of specific moments. Consequently, the allocation is done to the remaining ailerons after the first failure, and then to the only remaining aileron set after the second failure. Note that the remaining ailerons are capable of eliminating the effect of the failure. The roll attitude is acquired back again right after each aileron set failures. The short duration gust at 50<sup>th</sup> second is also counteracted.

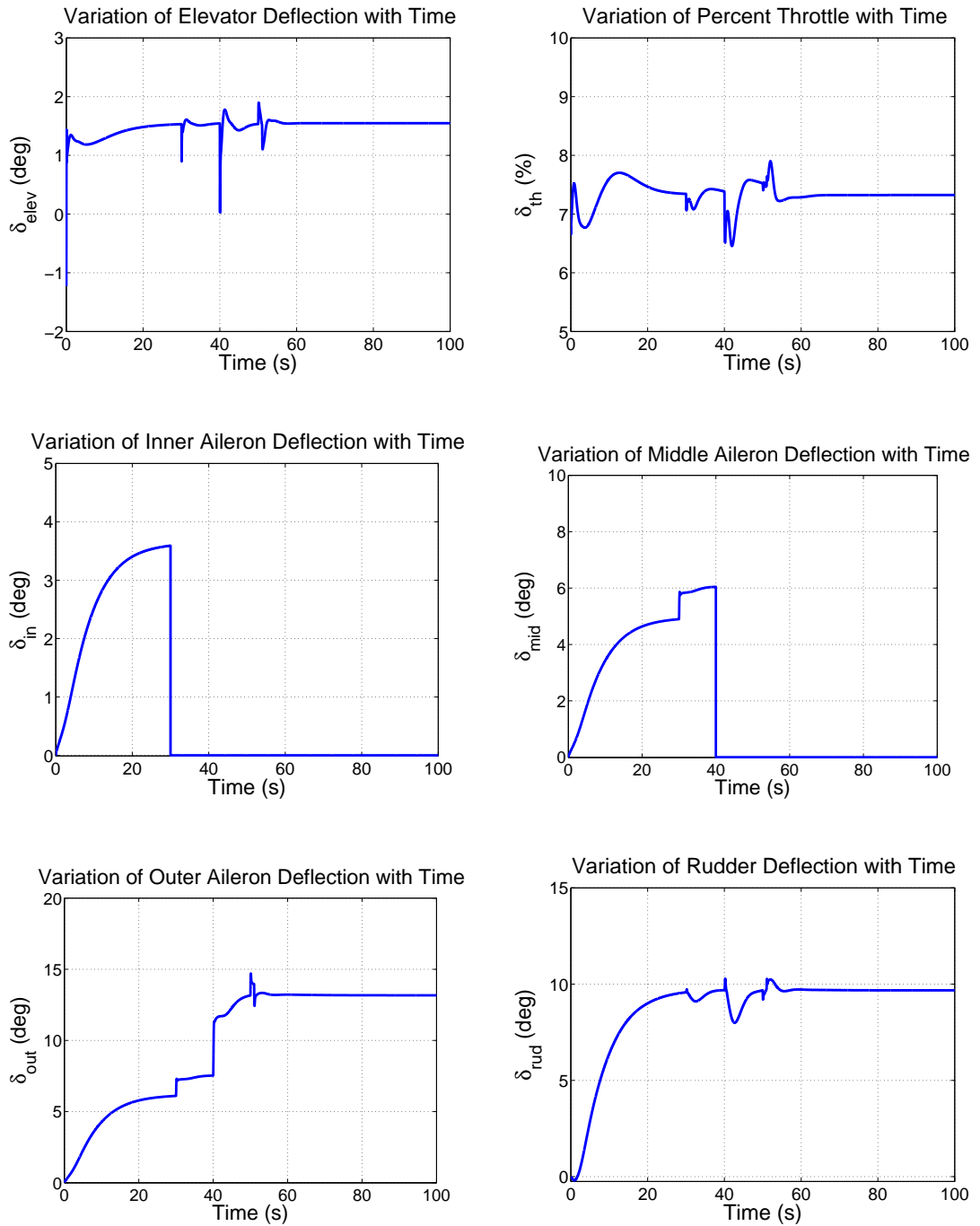


Figure 6.7: Variations of the Controls for a Roll Maneuver with Redundant Ailerons

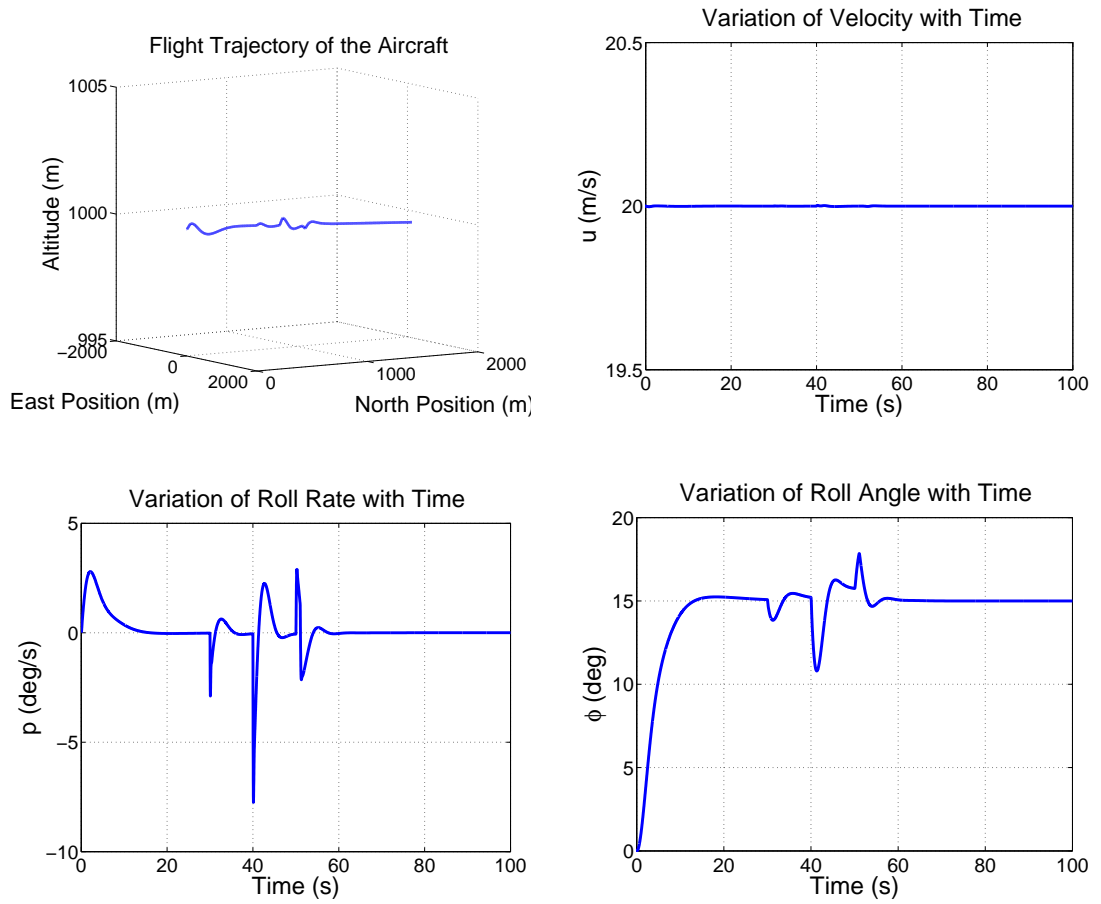


Figure 6.8: Simulation Results for a Roll Maneuver with Redundant Ailerons

### 6.3.3 Scenario-3

In this third case study, the UAV is commanded to fly steady wings level first, then to carry out a steady, 3 deg/s coordinated turn and to go back to steady wings level flight again. The scenario is planned to have the middle aileron pair loss at the 25<sup>th</sup> second, meanwhile, the inner aileron pair got stuck at its maximum position (20 degrees), finally a roll gust causing 5 deg/s roll rate disturbance acted for a short duration. The simulation results for the control inputs are given in Figure 6.9. It may be observed from these results that, the feedback system again commands more specific moments to the roll channel. This, in turn, translated as more control surface deflections to the available ailerons. It should be stressed that, the deflection commands are also going to the failed aileron channels without any response. As can be seen from the plots, the healthy aileron sets automatically take over the burden and successfully complete the maneuver. From the simulation results given in Figure 6.10 it can be seen that, the roll gust input around 50 s is also counteracted. The maneuver is completed successfully, without any offset, demonstrating the fault tolerant behavior of the flight control system with redundant actuators.

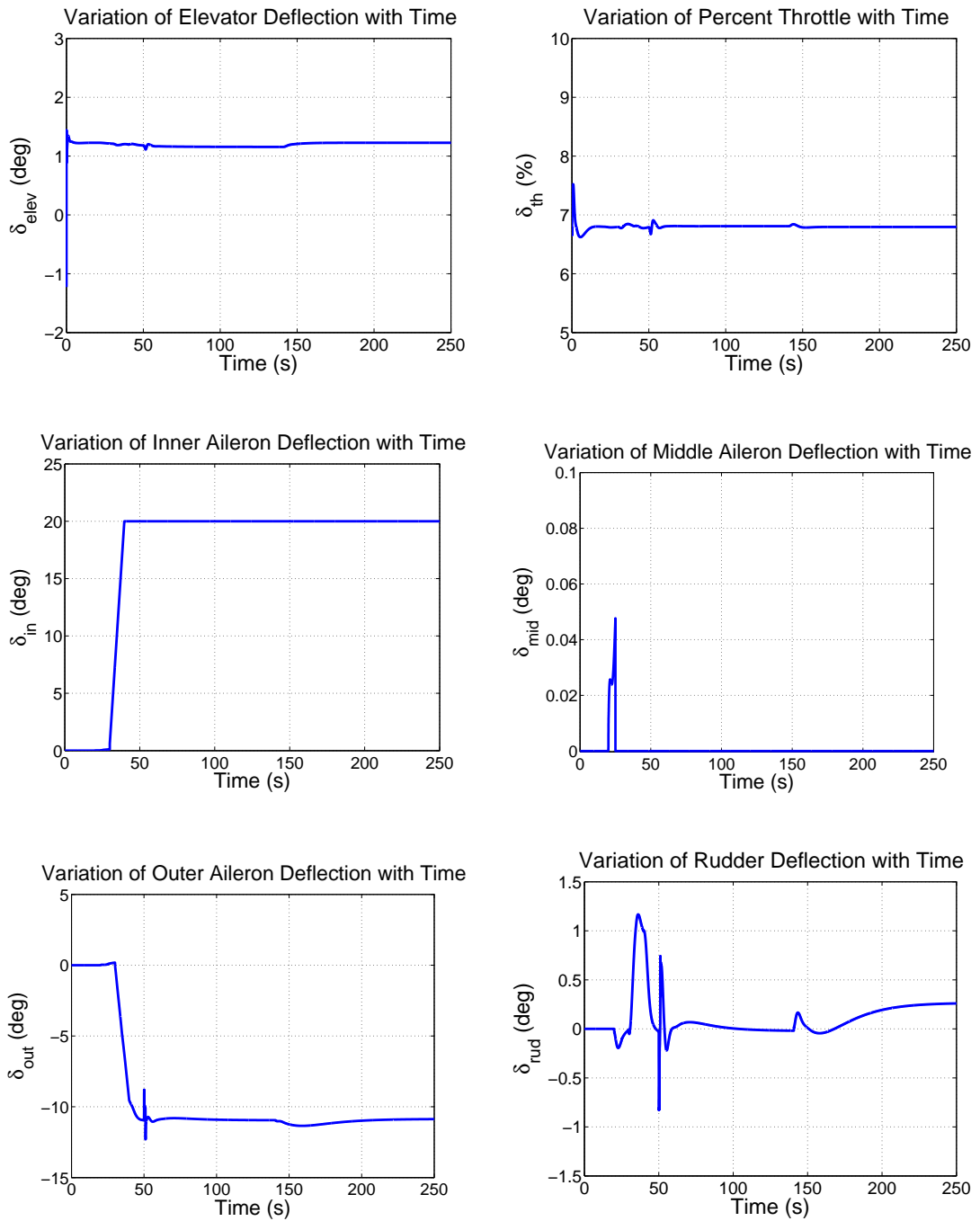


Figure 6.9: Variations of the Controls for a Coordinated Turn Maneuver with Redundant Ailerons

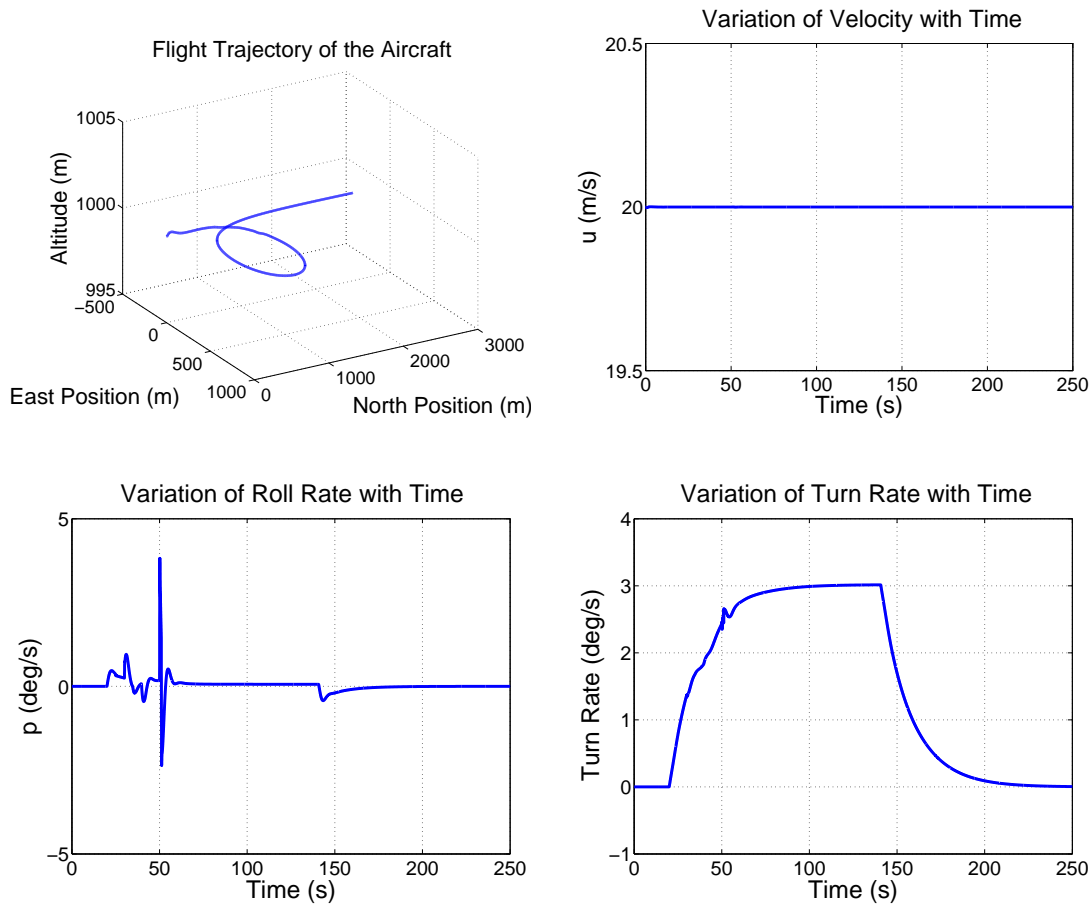


Figure 6.10: Simulation Results for a Coordinated Turn Maneuver with Redundant Ailerons

#### 6.3.4 Scenario-4

The purpose of this last study is to determine whether the fault tolerant behavior of the flight control system is maintained by the BI technique or the redundant set of ailerons. For this aim, the flight control system of the conventional UAV is modified such that the desired aileron deflections generated by the control system are equally commanded to each aileron set whereas with BI algorithm, aileron sets are commanded separately. In this study, actuator limits of the ailerons are decreased to 10 degrees and the aircraft is commanded to make a simple roll maneuver of 17 degrees. According to the scenario, 30 seconds after the simulation is started, the outer aileron pair is lost.

As can be seen from the simulation results given in Figure 6.11, the aircraft acquires the commanded roll attitude while holding its altitude and velocity constant at their initial values. Although the flight control system without BI is able to achieve the maneuver, at the moment of aileron loss, the remaining aileron pairs are saturated instantly (Figure 6.12). On the other hand, with BI algorithm, saturation is not observed. Moreover, with this method, it is possible to control each aileron pair separately.

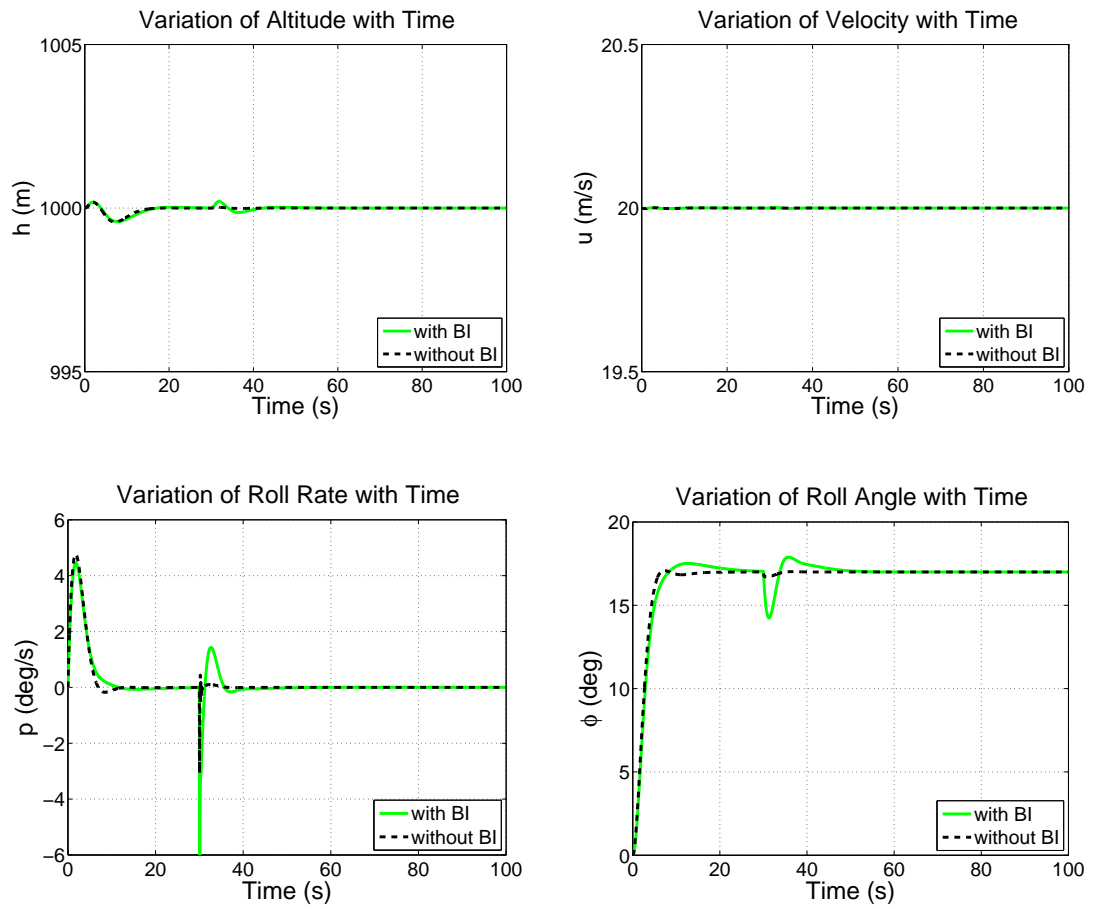


Figure 6.11: Simulation Results for Comparison of System Responses with and without Blended Inverse Method

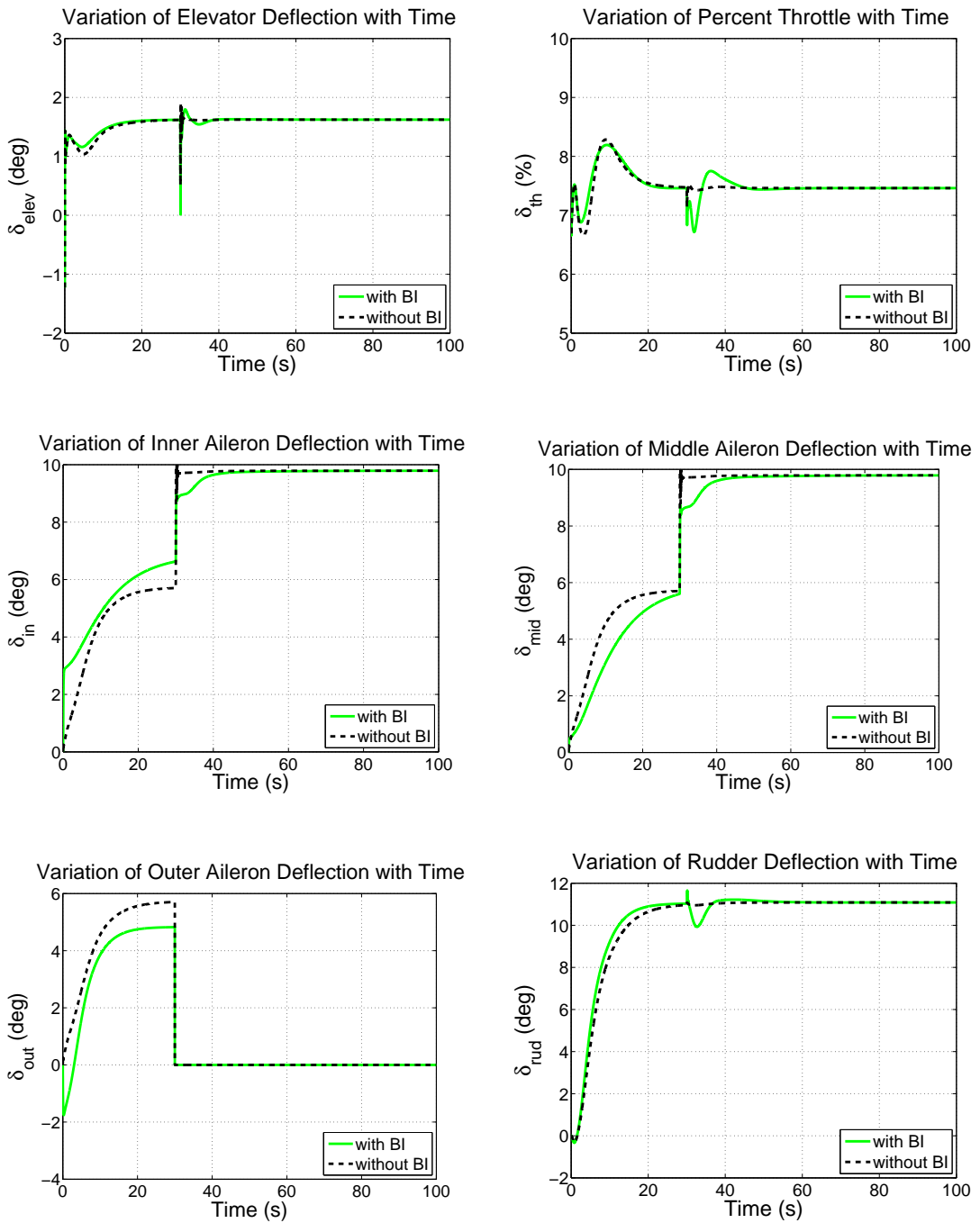


Figure 6.12: Variations of the Controls for Comparison of System Responses with and without Blended Inverse Method

## CHAPTER 7

### CONCLUSION

In this thesis work, automatic flight control systems are designed for a conventional and an over actuated UAV. For this purpose, first a nonlinear flight simulation model is developed. 6-DOF equations of motions, interpolated nonlinear aerodynamics, propulsion, mass-inertia and atmospheric models are generated in Matlab<sup>®</sup> - Simulink<sup>®</sup> environment. Actuator models are also included to obtain a more accurate model. This nonlinear simulation model is then used to calculate the trim flight conditions, linearize the flight mechanics equations around the trim points and test the automatic flight control algorithms.

In order to create the linear state space model to be used in development of the flight control algorithms, trim and linearization codes are developed. After validating these tools by using an existing airplane's data found in the literature, stability characteristics are examined. Trim and linearization results showed that, both longitudinal and lateral modes of the UAV are stable.

Automatic flight control algorithms of the conventional UAV based on both classical and robust approaches are presented. The purpose of designing different autopilots by classical PID and robust  $H_\infty$  control techniques is to compare their performances in presence of errors in the plant model as well as variations in the aircraft dynamics and to select the controller design method for the over actuated UAV. Linear UAV model is used for the controller designs. Because the coupling between the longitudinal and lateral aircraft dynamics is found to be negligible, longitudinal and lateral controllers are designed separately, and then combined together for full autonomous flight. Performances are compared through nonlinear simulations in case of sensor noises, wind gusts and variations in the aerodynamic database. Results demonstrated that, both classical and robust controllers are able to track the command inputs,

tolerate the measurement noises, eliminate the effect of uncertainties and also counteract the wind gusts.

In the thesis, the ultimate goal is to address the fault tolerant control of a UAV with redundant control surfaces. The autopilot is designed using classical sequential loop closing methods and two static control allocation methods, namely Moore-Penrose pseudo (MP) inverse and blended inverse are applied for allocating the controls to redundant actuators in the flight control system. To demonstrate use of which allocation method would yield the desired performance in case of actuator failures, a simulation study is carried out. It is observed that, although MP-inverse realizes the maneuver, due to lack of control authority on the redundant actuators, it is not possible to prevent saturation by using this method. On the other hand, with blended inverse not only the maneuver is achieved but also saturation is avoided since the controls are allocated to the desired actuators selectively. Other simulations with different scenarios are also performed to demonstrate the effectiveness of the blended inverse algorithm further. According to the results it can be concluded that, with redundant control surfaces, fault tolerant control is possible. In addition, blended inverse algorithm is quite successful to realize the maneuver, control the aircraft and recover the UAV when one or more control surfaces are damaged or stuck. As a result, flight safety as well as flight quality of the aircraft is improved.

On top of the research carried out in this thesis, the following items can be suggested as future work:

- The existing simulation model of the UAV shall be enhanced by a system identification study
- Different wind - turbulence models may be implemented to the simulation model
- Flight control system of the over actuated UAV may be designed by using robust control techniques
- Additive uncertainty form may be used to obtain better robust performance
- The approaches in using additional redundant controls shall be investigated to improve the vehicle's reliability and survivability further

## REFERENCES

- [1] Abdulrahim, M. “*Flight Dynamics and Control of an Aircraft with Segmented Control Surfaces*”, 42nd AIAA Flight Sciences Meeting, and Exhibit, Reno, NV, AIAA-2004-128, January 2004.
- [2] Ahuactzin ,J. M., Gupta, K. K. “*The Kinematic Roadmap: A Motion Planning Based Global Approach for Inverse Kinematics of Redundant Robots*”, IEEE Transactions on Robotics and Automation, Vol. 15, pp. 653–669, August 1999.
- [3] Altay, A. “*Steering of Redundant Robotic Manipulators and Spacecraft Integrated Power and Attitude Control - Control Moment Gyroscopes*”, MS Thesis, Aerospace Engineering Department, METU, January 2006.
- [4] Astrom, K. J.,Hagglund, T. “*Advanced PID Control*”, ISA-The Instrumentation, Systems, and Automation Society, 2006.
- [5] Astrom, K. J.,Hagglund, T. “*Automatic Tuning of PID Controllers*”,Instrument Society of America, 1988.
- [6] Balas, G. J., Doyle., J. C., Glover, K., Packard, A., Smith, R. “ *$\mu$  –Analysis and Synthesis Toolbox*”, Mathworks, Mass, 1995.
- [7] Bodson, M. “*Evaluation of Optimization Methods for Control Allocation*”, Journal of Guidance, Control, and Dynamics, Vol. 25, No. 4, pp. 703–711, 2002.
- [8] Castillo, C. L., Alvis, W., Effen, M. C., Moreno, W., Valavanis, K. “*Small Scale Helicopter Analysis and Controller Design for Non-Aggressive Flights*”, University of South Florida, Department of CSE and EE.
- [9] Cheng-Ching, Y. “*Autotuning of PID Controllers: A Relay Feedback Approach*”, Springer, 2006.
- [10] Doyle, J. C., and Packard, A. “*Uncertainty Multivariable Systems from a State Space Perspective*”, In Proc. American Control Conf., pp. 2147–2152, Minneapolis, MN, 1987.
- [11] Doyle, J. “*Structured Uncertainties in Control System Design*”, Proc. of the 24th Conference on Decision and Control, Lauderdale, pp. 260–265, 1985.
- [12] Doyle, J. “*Lecture Notes on Advances in Multivariable Control*”, ONR/Honeywell Workshop, Minneapolis, 1984.
- [13] Doyle, J. C., Francis, B., Tannenbaum, A. “*Feedback Control Theory*”, Macmillan Publishing Co., 1990.
- [14] Doyle, J. C., Glover, K., Khargonekar, P. P., Francis, B. A., “*State-space Solutions to Standard  $H_2$  and  $H_\infty$  Problems*”, IEEE Transactions on Automatic Control, vol.AC-34, No. 8, pp 831-847, 1989.

- [15] Doyle, J. C. “*Robustness of Multiloop Linear Feedback Systems*”, Proc. 17th IEEE Conf. Decision and Control, pp. 12-18, 1979.
- [16] Ellis, G. “*Observers in Control Systems: A Practical Guide*”, Academic Press, 2002.
- [17] Etkin B., Reid L.D. “*Dynamics of Flight, Stability and Control, 3rd Edition*”, John Wiley & Sons, Inc., 1996.
- [18] Francis, B. A., Doyle, J. C. “*Linear Control Theory with an  $H_\infty$  Optimality Criterion*”, SIAM J. Control Opt., vol. 25, 1987.
- [19] Frew, E., Xiao, X., Spry, S., McGee, T., Kim, Z., Tisdale, J., Sengupta, R., Hendrick, K.J. “*Flight Demonstrations of Self-directed Collaborative Navigation of Small Unmanned Aircraft*”, Proceedings of the 2004 IEEE Aerospace Conference, Big Sky, MT, March 2004.
- [20] Glover, K., Doyle, J. C. “*A State-space Approach to  $H_\infty$  Optimal Control*”, Springer-Verlag, Berlin, 1989.
- [21] Goodwin, G. C., Graebe, S. F., Salgado, M. E. “*Control System Design*”, 1st. Prentice Hall PTR, 2000.
- [22] Hald, U. B., Hesselbæk, M. V., Holmgaard, J.T., Jakobsen, S.L, Siegumfeldt, M. “*Autonomous Helicopter - Modelling and Control*”, Aalborg University, Department of Control Engineering, 2005.
- [23] Harkegard, O. “*Dynamic Control Allocation using constrained quadratic programming*”, Journal of Guidance Control and Dynamics, 27(6), 1027-1038, 2004.
- [24] Jodeh, N. M., Blue, P. A. and Waldron, A. A. “*Development of Small Unmanned Aerial Vehicle Research Platform: Modeling and Simulating with Flight Test Validation*”, AIAA 2006-6261, 2006.
- [25] Jodeh, Nidal M. “*Development of Autonomous Unmanned Aerial Vehicle Research Platform: Modeling, Simulating, and Flight Testing.*”, MS Thesis, AFIT/GAE/ENY/06-M18. School of Engineering and Management, Air Force Institute of Technology (AFIT), Wright-Patterson AFB, OH. March 2006.
- [26] Kargin, V., Yavrucuk, I. “*Autolanding Strategies for a Fixed wing UAV Under adverse Atmospheric Conditions*”, American Institute of Aeronautics and Astronautics, Guidance, Navigation and Control Conference, Honolulu, HI, USA, August 2008.
- [27] Kargin, V. “*Design of an Autonomous Landing Control Algorithm for a Fixed Wing UAV*”, MS Thesis, Aerospace Engineering Department, Middle East Technical University, October 2007.
- [28] Kim, T. “*Development of an Interactive Modeling, Simulation, Animation, and Real-time Control (MoSART) Aircraft Environment*”, MS Thesis, Arizona State University, May 2000.
- [29] Kuo, B. C. “*Automatic Control Systems*”, Prentice Hall Englewood Cliffs, New Jersey, 1999.

- [30] Legowo, A. and Okubo, H. “*Robust Flight Control Design for a Turn Coordination System with Parameter Uncertainties*”, American Journal of Applied Sciences, Vol. 4, No. 7, pp 496–501, 2007.
- [31] Leonard, J. R. “*Investigation of Lateral-Directional Coupling in Longitudinal Responses of a Transfer Function Simulation Model*”, MS Thesis, Aerospace Engineering Department, Virginia Polytechnic Institute & State University, December 2003.
- [32] Lunze, J. “*Robust Multivariable Feedback Control*”, Prentice Hall, 1989.
- [33] McDonnell Douglas Corporation “*United States Air Force (USAF) Stability and Control DATCOM*”, Douglas Aircraft Division and Flight Control Division, Wright-Patterson Air Force Base, OH, April 1978.
- [34] McLean, D. “*Automatic Flight Control Systems*”, Prentice Hall, 1990.
- [35] Mickle, M. C., Zhu, J. J. “*Simulation Results for Missile Autopilot Design Based on Extended Mean Assignment*”, System Theory, Proceedings of the Twenty-Eight Southern Symposium, 1996.
- [36] Nakamura, Y., Hanafusa, H. “*Inverse Kinematics Solutions with Singularity Robustness for Robot Manipulator Control*”, Journal of Dynamics, Measurement and Control, vol. 108, pp. 163-171, 1986.
- [37] Ogata, K. “*Modern Control Engineering*”, Prentice Hall, 2002.
- [38] Packard, A., and Doyle, J. “*The Complex Structured Singular Value*”, Automatica, 29 No. 1 pp. 71–109, 1993.
- [39] Roskam, J. “*Airplane Design, Part VI: Preliminary Calculation of Aerodynamic, Thrust and Power Characteristics*”, Roskam Aviation and Engineering Corporation, 2nd Ed. 1990.
- [40] Ruijgrok, G.J.J. “*Elements of airplane performance*”, Delft University Press, Delft, 1990.
- [41] Sadraey, M., Colgren, R. “*Robust Nonlinear Controller Design for a Complete UAV Mission*”, American Institute of Aeronautics and Astronautics, Guidance, Navigation and Control Conference and Exhibit, Keystone, Colorado, 21 - 24 August 2006.
- [42] Sarris, Z. “*Survey of UAV Applications in Civil Markets*”, Technical University of Crete, 2001.
- [43] Skogestad, S., Postlethwaite, I. “*Multivariable Feedback Control – Analysis and Design*”, 2nd Edition, Wiley, 2005.
- [44] Spillman, M. S. “*Robust Longitudinal Flight Control Design Using Linear Parameter-Varying Feedback*”, Journal of Guidance, Control, and Dynamics, Vol. 23, No. 1, pp 101–108, January–February 2000.
- [45] Stevens, B.L., Lewis, F.L. “*Aircraft Control and Simulation*”, John Wiley & Sons Inc., 1992.
- [46] U.S. Government Printing Office “*U.S. Standard Atmosphere*”, Washington, D.C, 1976.

- [47] Ünlü, T. “*Automatic Flight Control System Design of an Unmanned Tilt Rotor Aircraft*”, MS Thesis, Aerospace Engineering Department, METU, September 2009.
- [48] Tekinalp, O., Ünlü, T., Yavrucuk, İ. “*Simulation and Flight Control of a Tilt Duct UAV*”, AIAA Modeling and Simulation Technologies Conference, Chicago, IL, 10-13 August 2009.
- [49] Tekinalp, O., and Yavuzoglu, E. “*A New Steering Law for Redundant Control Moment Gyroscope Clusters*”, Aerospace Science and Technology, Vol. 9, No. 7, pp. 626-634, October 2005.
- [50] Visioli, A. “*Practical PID Control*”, Springer, 2006.
- [51] Vo, H., Seshagiri, S. “*Robust Control of F-16 Lateral Dynamics*”, International Journal of Mechanical, Industrial and Aerospace Engineering, Vol. 2, No. 2, pp 80–85, 2008.
- [52] Wie, B. “*Space Vehicle Dynamics and Control*”, AIAA Education Series, AIAA Inc., Reston, VA, 1998.
- [53] Yavuzoglu, E. “*Steering Laws for Control Moment Gyroscope Systems Used in Spacecraft Attitude Control*”, MS Thesis, Aerospace Engineering Department, METU, November 2003.
- [54] Zames, G. “*Feedback and optimal sensitivity: Model Reference Transformations, Weighted Seminorms, and Approximate Inverses*”, Proc. 17th Allerton Conf., pp. 744-752, 1979.
- [55] Zames, G. “*Feedback and Optimal Sensitivity: Model Reference Transformation, Multiplicative Semi-norms and Approximate Inverses*”, IEEE Transactions on Automatic Control, vol. AC-26, pp.301-320, 1981.
- [56] Zames, G. “*On the input-output stability of non-linear time-varying feedback systems, Part I and II*”, IEEE Trans. On Automatic Control, II, pp.228-238 and pp.465-476, 1966.
- [57] Zhou, K., Doyle, J. C., Glover, K. “*Robust and Optimal Control*”, Prentice Hall, 1996.

## APPENDIX A

### UAV GEOMETRY

#### A.1 Aircraft Geometric Parameters

##### A.1.1 Wing Geometry

Table A.1: Geometric Parameters of Wing

Parameter	Acronym	Value	Unit
Span	$b_w$	2.79	m
Area	$S_w$	0.98	m <sup>2</sup>
Root chord	$c_{r_w}$	0.41	m
Wing leading edge point	$X_w$	0.32	m
Incidence	$i_w$	0	deg
Dihedral	$\Gamma_w$	4	deg
Twist	-	0	deg
Leading edge sweep	$\Gamma_{LE_w}$	0	deg
Quarter chord sweep	$\Gamma_{c/4_w}$	0	deg
Aspect ratio	AR	7.94	
Oswald efficiency	e	0.7	
Taper ratio	$\lambda_w$	0.73	
Top airfoil section		Eppler 193	
Bottom airfoil section		Eppler 205	
Airfoil for Datcom		NACA 4310	

### A.1.2 Horizontal Tail Geometry

Table A.2: Geometric Parameters of Horizontal Tail

Parameter	Acronym	Value	Unit
Span	$b_{HT}$	0.93	m
Area	$S_{HT}$	0.18	m <sup>2</sup>
Root chord	$c_{rHT}$	0.25	m
Horizontal tail leading edge point	$X_{HT}$	1.50	m
Incidence	$i_{HT}$	0	deg
Dihedral	$\Gamma_{HT}$	0	deg
Twist	-	0	deg
Leading edge sweep	$\Gamma_{LEHT}$	0	deg
Quarter chord sweep	$\Gamma_{c/4HT}$	0	deg
Taper ratio	$\lambda_{HT}$	0.57	
Airfoil for Datcom		NACA 0009	

### A.1.3 Vertical Tail Geometry

Table A.3: Geometric Parameters of Vertical Tail

Parameter	Acronym	Value	Unit
Span	$b_{VT}$	0.29	m
Area	$S_{VT}$	0.07	m <sup>2</sup>
Root chord	$c_{rVT}$	0.33	m
Vertical tail leading edge point	$X_{VT}$	1.44	m
Incidence	$i_{VT}$	0	deg
Dihedral	$\Gamma_{VT}$	0	deg
Twist	-	0	deg
Leading edge sweep	$\Gamma_{LEVT}$	25	deg
Quarter chord sweep	$\Gamma_{c/4VT}$	0	deg
Taper ratio	$\lambda_{VT}$	0.52	
Airfoil for Datcom		NACA 0009	

# APPENDIX B

## SIMULATION SUBSYSTEMS

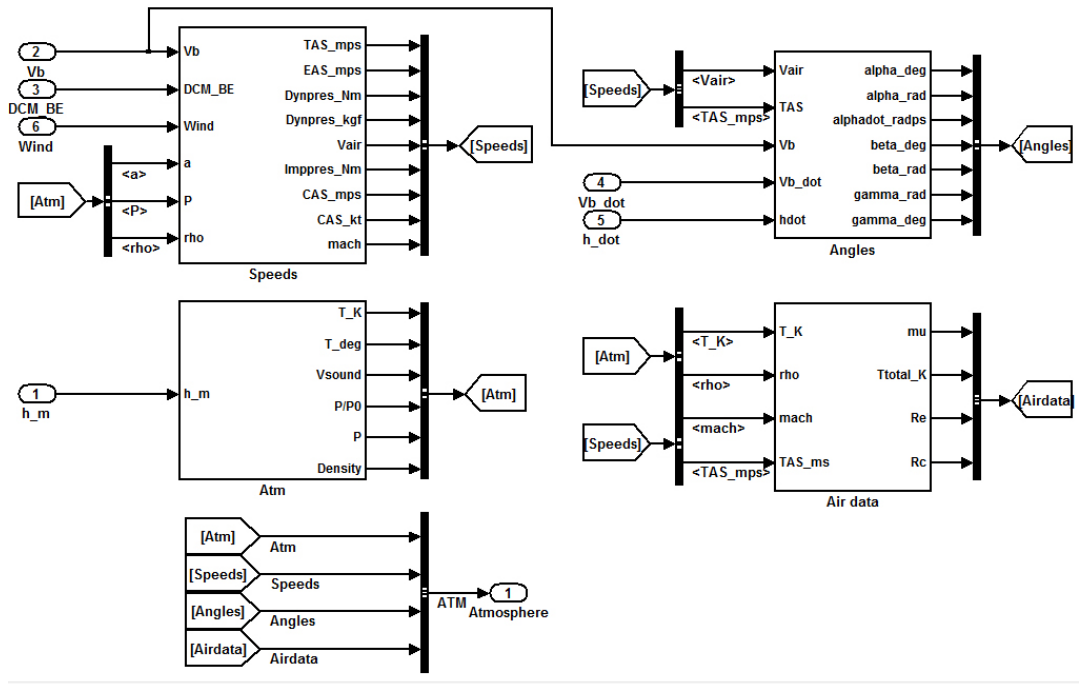


Figure B.1: Atmosphere Subsystem Model

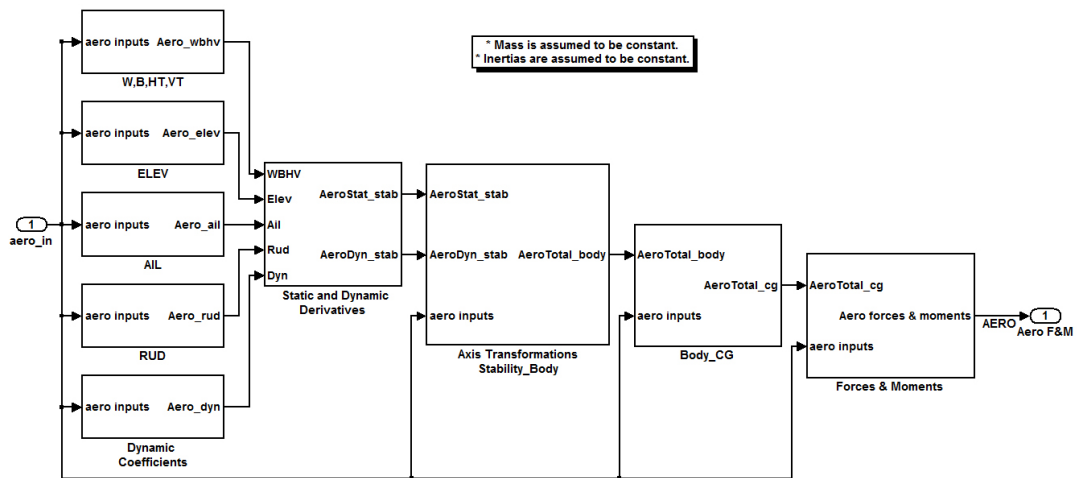


Figure B.2: Aerodynamics Subsystem Model

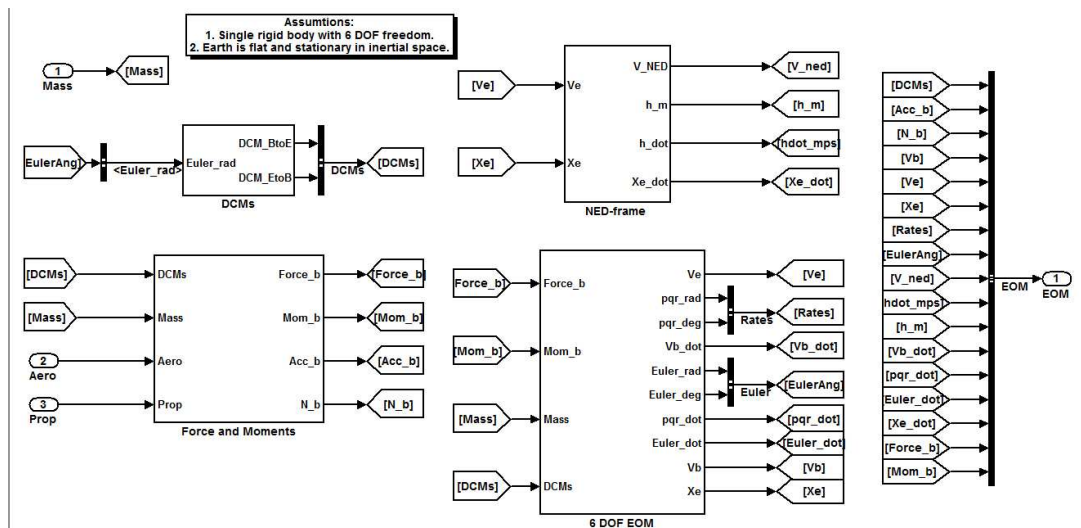


Figure B.3: Equations of Motion Subsystem Model

## APPENDIX C

### LINEARIZED SYSTEM MATRICES

#### C.1 Conventional UAV

$$A_{long} = \begin{bmatrix} -0.0893 & 0.1064 & 0.3701 & -9.8039 \\ -1.1273 & -7.4207 & 17.7733 & 0.2041 \\ 0.0406 & -0.3144 & -8.0281 & 0 \\ 0 & 0 & 1.0000 & 0 \end{bmatrix} \quad (C.1)$$

$$B_{long} = \begin{bmatrix} -0.5302 & 0.1135 \\ -9.8269 & -0.0001 \\ -33.0768 & -0.0003 \\ 0 & 0 \end{bmatrix} \quad (C.2)$$

$$C_{long} = \begin{bmatrix} 1 & 0 & 0 & 0 \\ 0 & 1 & 0 & 0 \\ 0 & 0 & 1 & 0 \\ 0 & 0 & 0 & 1 \end{bmatrix} \quad (C.3)$$

$$A_{late} = \begin{bmatrix} -0.4807 & -0.6362 & -20.0000 & 9.8039 & 0 \\ -0.9700 & -8.2639 & 0.1482 & 0 & 0 \\ 0.2808 & -0.3477 & -0.5848 & 0 & 0 \\ 0 & 1.0000 & -0.0208 & 0 & 0 \\ 0 & 0 & 1.0002 & 0 & 0 \end{bmatrix} \quad (C.4)$$

$$B_{late} = \begin{bmatrix} 0 & 2.3193 \\ 55.7042 & 1.0549 \\ -3.5463 & -7.8857 \\ 0 & 0 \\ 0 & 0 \end{bmatrix} \quad (C.5)$$

$$C_{late} = \begin{bmatrix} 1 & 0 & 0 & 0 & 0 \\ 0 & 1 & 0 & 0 & 0 \\ 0 & 0 & 1 & 0 & 0 \\ 0 & 0 & 0 & 1 & 0 \\ 0 & 0 & 0 & 0 & 1 \end{bmatrix} \quad (C.6)$$

## C.2 Over Actuated UAV

$$A_{late} = \begin{bmatrix} -0.4807 & -0.6362 & -20.0000 & 9.8039 & 0 \\ -0.9700 & -8.2639 & 0.1482 & 0 & 0 \\ 0.2808 & -0.3477 & -0.5848 & 0 & 0 \\ 0 & 1.0000 & -0.0208 & 0 & 0 \\ 0 & 0 & 1.0002 & 0 & 0 \end{bmatrix} \quad (C.7)$$

$$B_{late} = \begin{bmatrix} 0 & 0 & 0 & 2.3193 \\ 15.8546 & 20.9481 & 26.0433 & 1.0549 \\ -0.8574 & -1.2603 & -1.5801 & -7.8857 \\ 0 & 0 & 0 & 0 \\ 0 & 0 & 0 & 0 \end{bmatrix} \quad (C.8)$$

$$C_{late} = \begin{bmatrix} 1 & 0 & 0 & 0 & 0 \\ 0 & 1 & 0 & 0 & 0 \\ 0 & 0 & 1 & 0 & 0 \\ 0 & 0 & 0 & 1 & 0 \\ 0 & 0 & 0 & 0 & 1 \end{bmatrix} \quad (C.9)$$